

Determining local viscoelastic properties of collagen systems using optical tweezers

by

Marjan Shayegan

M.Sc., Sharif University of Technology, 2008

B.Sc., Sharif University of Technology, 2005

Thesis Submitted in Partial Fulfillment of the
Requirements for the Degree of
Doctor of Philosophy

in the
Department of Chemistry
Faculty of Science

© **Marjan Shayegan 2014**

SIMON FRASER UNIVERSITY

Spring 2014

All rights reserved.

However, in accordance with the *Copyright Act of Canada*, this work may be reproduced, without authorization, under the conditions for "Fair Dealing." Therefore, limited reproduction of this work for the purposes of private study, research, criticism, review and news reporting is likely to be in accordance with the law, particularly if cited appropriately.

Approval

Name: Marjan Shayegan
Degree: Doctor of Philosophy (Chemistry)
Title: *Determining local viscoelastic properties of collagen systems using optical tweezers*
Examining Committee: Chair: David Vocadlo
Professor

Dr. Nancy R. Forde
Senior Supervisor
Associate Professor

Dr. Barbara J. Frisken
Supervisor
Professor

Dr. Zuo-Guang Ye
Supervisor
Professor

Dr. Erika Plettner
Internal Examiner
Professor

Dr. John R. de Bruyn
External Examiner
Professor
Department of Physics
The University of Western Ontario

Date Defended: January 13, 2014

Partial Copyright Licence



The author, whose copyright is declared on the title page of this work, has granted to Simon Fraser University the non-exclusive, royalty-free right to include a digital copy of this thesis, project or extended essay[s] and associated supplemental files ("Work") (title[s] below) in Summit, the Institutional Research Repository at SFU. SFU may also make copies of the Work for purposes of a scholarly or research nature; for users of the SFU Library; or in response to a request from another library, or educational institution, on SFU's own behalf or for one of its users. Distribution may be in any form.

The author has further agreed that SFU may keep more than one copy of the Work for purposes of back-up and security; and that SFU may, without changing the content, translate, if technically possible, the Work to any medium or format for the purpose of preserving the Work and facilitating the exercise of SFU's rights under this licence.

It is understood that copying, publication, or public performance of the Work for commercial purposes shall not be allowed without the author's written permission.

While granting the above uses to SFU, the author retains copyright ownership and moral rights in the Work, and may deal with the copyright in the Work in any way consistent with the terms of this licence, including the right to change the Work for subsequent purposes, including editing and publishing the Work in whole or in part, and licensing the content to other parties as the author may desire.

The author represents and warrants that he/she has the right to grant the rights contained in this licence and that the Work does not, to the best of the author's knowledge, infringe upon anyone's copyright. The author has obtained written copyright permission, where required, for the use of any third-party copyrighted material contained in the Work. The author represents and warrants that the Work is his/her own original work and that he/she has not previously assigned or relinquished the rights conferred in this licence.

Simon Fraser University Library
Burnaby, British Columbia, Canada

revised Fall 2013

Abstract

In this work, I aimed to develop and apply a technique capable of measuring the viscoelastic properties of collagen at different levels of hierarchy. Collagen is the predominant structural protein in vertebrates, and its self-assembly into well-defined structures including fibrils underlies the formation of a wide variety of biological structures with a broad range of functions. Here, in order to understand the correlation between collagen's structure and its mechanical properties, the viscoelastic properties of different collagen systems were characterized, ranging from solutions of molecules to self-assembled forms of fibrillar gels and gelatin.

To determine rheological properties, optical tweezers were used to trap and monitor thermal fluctuations of an embedded micron-sized particle, producing measurements of viscoelastic response of collagen systems at a high bandwidth ($> 10^4$ Hz). To validate these measurements, I reproduced results on a previously characterized system (polyethylene oxide). The obtained viscoelastic response is affected by the timescales of the interactions between polymers, which play a critical role in conferring elasticity to the system. To provide guidance to the microrheology experiments, the structure of collagen in acidic solution was probed using dynamic light scattering. My microrheology studies of collagen molecules in acidic solution showed that elastic response becomes comparable to viscous response at the highest concentration studied here, 5 mg/ml. Here, the significant elasticity observed at frequencies above ~ 200 Hz is due to collagens' intermolecular interactions, which I found were not due to electrostatic interactions. However, elasticity was found to decrease following the removal of collagen's telopeptides, consistent with their role in facilitating fibril formation.

At the fibrillar level, unlike in solutions of collagen, I observed spatial heterogeneity in viscoelastic properties. The elastic modulus varies by an order of magnitude at different locations within fibrillar collagen gels. By making measurements over 100-minute timescales as collagen self-assembled into fibrils, I probed the development of microscale heterogeneity and concluded that heterogeneity appears during early phases of fibrillar growth and continues to develop further during this growth phase.

Keywords: Collagen; self-assembly; fibrils; microrheology; optical tweezers; complex shear modulus

Dedication

To my husband, Amir, for all of his love and support and for being a constant source of encouragement during this time.

Acknowledgements

A great number of people have helped me during my PhD work. I would like to take this opportunity to personally thank them.

My first and sincere appreciation goes to Dr. Nancy Forde, my supervisor, for providing continuous support, encouragement and help during these years. I want to thank her not only for her thoughtful advices for research but also for teaching me valuable life lessons as a successful academic woman.

I would like to thank Dr. Barbara Frisken and her lab members for letting us to use their light scattering instrument and their help in the interpretation of those results. I would also like to thank Dr. Martin Zuckermann, Dr. Michael Plischke and Dr. Zuo-Gang Ye for their invaluable ideas and discussions in the past few years.

I would also like to thank all the past and present members of the Forde lab for making such an amazing and supportive environment in this group. My especial acknowledgment goes to Andrew for sharing his invaluable “decades of experience” in the biochemistry and many other areas with me. My other especial acknowledgment is to Astrid for passing her optical tweezers on to me, to Norman and Tuba for all their hard work on different aspects of collagen microrheology and to Laleh and Naghmeh for being such supportive and helpful friends. I would like to extend my appreciation to all my dear friends both at SFU and UBC.

Finally, I would like to express my deepest gratitude to my dear family, my mom and dad, to my sister, Maryam, and her lovely family for their never-ending encouragement and support during my PhD study. Last, but not least, I want to thank my dear husband, Amir, for standing beside me throughout this study and writing this thesis and for being such a patient and supportive person in my life.

Table of Contents

Approval.....	ii
Partial Copyright Licence	iii
Abstract.....	iv
Dedication	v
Acknowledgements	vi
Table of Contents.....	vii
List of Tables.....	ix
List of Figures.....	x
List of Symbols.....	xix

Chapter 1. Introduction.....	1
1.1. Collagen.....	1
1.2. Rheology and Viscoelastic Properties.....	4
1.3. Selected Topics in Polymer Physics	9
1.4. Microrheology.....	13

Chapter 2. Optical-Tweezers-Based Microrheology	18
2.1. Principles of Optical Tweezers	18
2.2. The Optical Tweezers Apparatus.....	23
2.3. General Sample Preparation for Microrheology Experiments	26
2.4. Principles of Analyses for Microrheology	27
2.5. Verification of the Microrheological Characterization Technique	43
2.5.1. Experimental Details	44
2.5.2. Microrheology of water	44
2.5.3. Microrheology of PEO	45

Chapter 3. Collagen and its characterization	48
3.1. Collagen structure and self-assembly	48
3.2. Materials.....	52
3.3. Sodium Dodecyl Sulfate Polyacrylamide Gel Electrophoresis (SDS-PAGE)	52
3.4. Enzyme-Linked Immunosorbent Assay (ELISA)	55
3.5. Turbidity Measurements of Fibril Formation Kinetics	55
3.6. TEM study of collagen fibrils.....	58

Chapter 4. Dynamic Light Scattering	61
4.1. Theory	61
4.2. Details of the Light Scattering Instrument	64
4.3. DLS of a Spherical System.....	64
4.4. DLS of a Rigid-Rod System.....	65
4.5. DLS of Collagen Solutions.....	66
4.5.1. Effect of Collagen Concentration.....	67

4.5.2. Ultrasonication Technique.....	70
4.5.3. Ultracentrifugation Technique	73
Chapter 5. Solutions of Collagen Molecules	80
5.1. Experimental and Analysis Details.....	81
5.2. Effect of Ultracentrifugation on Viscoelastic Properties	81
5.3. Concentration Dependence of Viscoelastic Properties	84
5.4. Effect of Charge and Size of Probe Particles.....	95
5.5. Effect of Salt.....	99
5.6. Effect of Molecular Modification (removal of telopeptides)	101
5.7. Summary.....	105
Chapter 6. Networks of Collagen Fibrils.....	106
6.1. Experimental and Analysis Details.....	107
6.2. Microrheology of Collagen Gels.....	108
6.3. Microrheology During Fibril Formation.....	116
6.4. Microrheology of Gelatin.....	123
6.5. Summary.....	126
Chapter 7. Conclusions and Future Directions.....	128
Bibliography	134
Appendix A. Rationale for the Preference of Manual Adjustment of Laser Power	149
Appendix B. Mathematical Derivation of the Relationship Between Trap Stiffness and Complex Shear Moduli	151
Appendix C. High-Frequency Dispersion of Elastic Modulus	153
Appendix D. Labelling Collagen with Alexa Fluorophore	157
Appendix E. Enzyme-Linked Immunosorbent Assay (ELISA)	159

List of Tables

Table 1.1.	List of major collagen types and information on their structure including contour length and higher order structure (if any), tissue localization, and diseases caused by genetic mutations. Information is adapted from [15,21].	3
Table 1.2.	A broad range of persistence length, radius of gyration, and overlap concentration has been found for collagen.	12
Table 2.1.	Refractive indices of collagen solutions compared with solvent (20 mM acetic acid) at 21°C	31
Table 3.1.	Amino acid composition of the chains (including telopeptides) in triple-helical collagen type I from rat tail tendon. (This information is sourced from the Universal Protein Resource, UniProt, for genes COL1A1 and COL1A2).	49
Table 3.2.	D-spacing values of type I collagen fibrils: formed <i>in-vivo</i> or <i>in-vitro</i> with different solvent conditions.	52
Table 4.1.	Calculated translational and rotational diffusion coefficients for different concentrations of collagen solutions	69
Table 4.2.	Collagen concentrations of the untreated, and 10- and 20-minute sonicated and filtered samples obtained by ELISA.	72

List of Figures

Figure 1.1.	Illustration of shear modulus versus frequency for a (A) pure solid, (B) pure liquid (e.g. water), and (C) viscoelastic material.....	6
Figure 1.2.	Schematic of (A) Maxwell and (B) Kelvin-Voigt models using a spring and dash-pot connected in series and parallel, respectively. Correspondingly, (C) and (D) illustrate elastic and viscous moduli of a viscoelastic material following the Maxwell and Kelvin-Voigt models.	7
Figure 1.3.	Elastic (circles) and viscous (triangles) moduli as a function of frequency for a 16 mg/ml collagen concentration collagen in 500 mM acetic acid. The low frequency behaviour is consistent with the Maxwell model. Figure is taken with permission from [38].	8
Figure 1.4.	Illustration of concentration regimes: Left-top figure shows the dilute regime (when $c < c^*$), right-top figure corresponds to the critical condition of $c = c^*$, and bottom figure shows the concentrated regime ($c > c^*$). Circles represent hypothetical spheres with radius R_g . Figure is taken with permission from [42].	10
Figure 1.5.	Definition of the persistence length, l_p , for a polymer chain.	11
Figure 1.6.	Representation of a flexible polymer chain by the bead-spring model.	13
Figure 2.1.	Gradient and scattering forces, produced from refraction and reflection, respectively, exerted by a laser beam with a Gaussian intensity profile on a microsphere, within a medium which has lower refractive index than the particle, are shown with arrows in each figure. (A) When the bead is centered in the beam, there is no net force perpendicular to the optical axis, while when it is slightly off-centered, (B) a net force perpendicular to the axis pushes the bead towards the maximum intensity.	21
Figure 2.2.	Schematic shows a bead in a potential well (blue line) created by an optical trap. The horizontal and vertical axes represent displacement from the center of the trap (minimum position in the well) and potential energy, respectively. The trap acts as a Hookean spring (right) where the force exerted on the bead is proportional to its displacement from the center of the trap. (Red arrows show directions of the forced motion.)	23
Figure 2.3.	Schematic diagram of our optical tweezers instrument. Figure is adapted with permission [111].	25

Figure 2.4.	The position of the light spot on the QPD surface determines the voltages V_x and V_y , values of which are calculated as the differences between the output voltages from the right and left, and up and down, respectively. The total voltage on the four quadrants also is calculated as the Sum value. When (A) the light spot is located at the center, both V_x and V_y are zero, while (B) when it is off-centered they are both non-zero values (with the same Sum value).	25
Figure 2.5.	Diagram of a sample chamber consisting of two coverslips sandwiching two pieces of parafilm (in gray). A micropipettor can be used to inject the sample (by capillary flow) into the chamber.	26
Figure 2.6.	Flowchart diagram of analysis for microrheological measurements using optical tweezers. The details are described in the text.	28
Figure 2.7.	Power spectrum of a 2.1 μm polystyrene particle trapped in water. The red line shows the corresponding fit of Eq. 2.5 to this data. Fitting parameters were $A = 0.054 \pm 8.4 \times 10^{-5} ((V/V)^2 \cdot \text{Hz})$, $f_c = 638 \pm 28 \text{ Hz}$	29
Figure 2.8.	(A) Positions measured by the camera (red line) plotted together with the displacement read out by the QPD (blue line) when the particle is intentionally displaced back and forth within the trap. (B) A subset of the data from (A) are replotted to extract the conversion factor (here, 1 Volt = 11.2 pixel and because in our setup 1 pixel = 52.0 nm, 1 Volt = 0.582 μm).	33
Figure 2.9.	The power spectrum of a particle in water (red crosses) is significantly different from that in a collagen solution of 2 mg/ml concentration (blue dots). The latter does not show a -2 slope at high frequency (dashed line), which is a characteristic of normal Brownian motion in purely viscous media. The red line shows the corresponding fit (Eq. 2.3) to the data obtained from water. Fitting parameters were $A = 0.0185 \pm 2.5 \times 10^{-5} (\mu\text{m}^2 \cdot \text{Hz})$ and $f_c = 638 \pm 28 \text{ Hz}$. This value of A corresponds to a bead radius of 1.17 μm , in agreement with the stated size.	34
Figure 2.10.	Real (blue circles) and imaginary (red crosses) parts of the complex response function for a 2.1 μm bead trapped in water.	36
Figure 2.11.	(A) Real (blue circles) and imaginary (red crosses) parts of the complex shear modulus measured for a 2.1 μm bead trapped in water. (B) Comparison of the obtained shear moduli from the original data ($f_{max}=50 \text{ kHz}$) and as if the data were sampled at $1/8^{\text{th}}$ of the original bandwidth ($f_{max}=6250 \text{ Hz}$). Each plot shows an average of 100 sets of 1-second measurements.	37

Figure 2.12.	The measured elastic modulus of water (blue circles/squares) scales with laser power. By correcting for trap modulus via subtraction of the low-frequency G' values (see text), the curves collapse to zero (green circles/squares). This plot is shown in semi-log scale. The large dispersion at high frequencies ($f > 200$ Hz) is predominantly due to the finite sampling. This issue is discussed more in Appendix C.	39
Figure 2.13.	Two examples of the $G'_{measured}$ values obtained for two different beads in water for a laser power of 150 mW. The actual sizes of the beads were determined by Eq. 2.5 and elasticity for the trap was corrected using Eq. 2.12. This plot is shown in semi-log scale to facilitate reading the data.	40
Figure 2.14.	Similar data as in Figure 2.13 when an average bead size is used instead of the actual size (Eq. 2.5). A small variation in bead size causes a large error in G'_{medium} , if Eq. 2.12 is used for correction of the trap.....	41
Figure 2.15.	Dark and light blue symbols are similar data as in Figures 2.13 and 2.14 when an averaged bead size is used instead of the actual size (Eq. 2.5). When the average value of the first few data points of $G'_{measured}$ is used as G'_{trap} , G'_{water} become similar and equal to zero for both measurements.	42
Figure 2.16.	Elastic (green circles) and viscous (red crosses) moduli of water are presented in logarithmically equally spaced format and averaged over ten different beads. Error bars show the standard deviation among these ten measurements.	43
Figure 2.17.	Elastic (green circles) and viscous (red crosses) moduli of water (replotted from Figure 2.16). The black line shows the corresponding fit (Eq. 2.14) to the values of viscous modulus. The fitting parameter (viscosity) obtained is 1.01×10^{-3} Pa.s.....	45
Figure 2.18.	(A) Elastic and (B) viscous moduli of 6.7 wt% PEO obtained using our optical tweezers technique (crosses), compared with bulk rheology (open symbols) and microrheology via diffusing-wave spectroscopy (DWS; solid line) from reference [120]. Crosses indicate the mean values over 5 independent measurements, and error bars represent the standard error of the mean.	46
Figure 3.1.	Hierarchical self-organization pathway of fibrillar collagen. Triple-helical molecules of collagen associate laterally to form fibrils with characteristic 67 nm D-banding patterns.	51

Figure 3.2.	SDS-gel electrophoresis reveals the presence (sharp bands corresponding to the α_1 and α_2 chains) and purity of the collagen stock solution using a gel stained with Coomassie blue dye in (A), and visualizing a fluorescently labelled collagen in a separate gel (B).....	54
Figure 3.3.	Turbidity measurements of collagen fibril formation kinetics at 30°C as a function of collagen concentration: 0.5 and 1 mg/ml. Here, collagen has its telopeptides intact. Error bars represent standard deviations from 5 replicate measurements.	56
Figure 3.4.	The effect of telopeptide removal on the kinetics of collagen fibril formation at 30°C and 1 mg/ml concentration. The gap between 120 and 130 minutes is because the experiment was stopped and re-run. Error bars represent standard deviations from 5 replicate measurements. The larger error bars obtained for the telopeptide-removed collagen versus collagen including telopeptides are due to their morphological difference: the former was a solution including white patches whereas the latter was a milky and macroscopically more homogenous solution.	57
Figure 3.5.	Turbidity measurements of collagen fibril formation at a collagen concentration of 0.5 mg/ml at 20°C and 30°C. Collagen has intact telopeptides.....	58
Figure 3.6.	(A) Transmission electron micrograph of collagen fibrils formed at 20°C and (B) its correlation with the staggered organization of the individual molecules.	60
Figure 4.1.	Schematic diagram of the light scattering technique: The laser light interacts with particles in a solution and scatters in different directions. When the scattered beam is monitored at an angle θ , the scattering vector \vec{q} is defined as the difference of the wavevector after and before scattering; this is shown geometrically on the right.	62
Figure 4.2.	Correlation function for a solution of polystyrene microspheres (diameter= 0.29 μm , concentration ~ 0.004 wt % in nanopure water) measured at an angle of $\theta = 30^\circ$ (red crosses). The black line corresponds to the fit (only over the range shown) obtained from Eq. 4.3.	64
Figure 4.3.	Correlation function obtained for a solution of TMV at a 30° angle. The black line shows the fit with Eq. (4.5), considering $B = 0.00925$. B is mathematically calculated using Ref. [146] at $\theta = 30^\circ$.).....	66

Figure 4.4.	Correlation function for a solution of collagen (concentration: 0.1 mg/ml) at two angles of (A) 30° and (B) 90°. Translational diffusion is extracted from the data at 30° in (A) and it was fixed for the analysis in part (B). For definitions of the parameters and fit functions, see the text.	68
Figure 4.5.	Comparison between correlation functions obtained for collagen solutions before sonication, after 6 minutes and after 45 minutes of sonication. The experimental data are compared with simulated curves based on three sets of values in Ref. [51] (all three of which appear indistinguishable here). All of the plots correspond to data taken at a scattering angle of 90°.	71
Figure 4.6.	Gel image of A) sonicated (10 and 20 minutes) and filtered collagen samples and B) sonicated collagen samples. The sonication process seems to be disruptive to the collagen molecules due to the fact that collagen bands disappear after this treatment.....	72
Figure 4.7.	Size distribution spectrum obtained by CONTIN analysis of collagen solution at a 90° angle (data in Figure 4.4(B)). Note: this plot is an unweighted spectrum; therefore, large particles tend to have larger amplitude because they scatter more, not necessarily because they are more numerous in solution.	75
Figure 4.8.	The total volume of the centrifuged collagen solution was divided into four layers and characterized (A) qualitatively by the gradient of the blue color in the labelled collagen and (B) by the intensity of the bands in the gel electrophoresis experiment. The schematic illustrates that the bottom layers are enriched in collagen after centrifugation.	76
Figure 4.9.	The correlation function for the ultracentrifuged collagen sample (red crosses) shows a significant reduction in decay time compared to the non-centrifuged sample (green circles). Results for the centrifuged sample are in a good agreement with curves plotted using values in the literature [51]. All curves correspond to data obtained at a scattering angle of 45°.	77
Figure 4.10.	Results for the ultracentrifuged sample (red dots) are compared to theoretical curves assuming collagen to be flexible (green line; $l_p = 15$ nm [25], $D_t = 8.9 \times 10^{-12}$ m ² /s), semiflexible (blue line; $D_t = 8.4 \times 10^{-12}$ m ² /s and $D_r = 800$ 1/s [51]), or a rigid rod (black line; $D_t = 7.8 \times 10^{-12}$ m ² /s and $D_r = 660$ 1/s). It is not possible to easily distinguish which theoretical curve is in better agreement with my experimental data either at 90° (A), or 45° (B), although the larger difference at 45° suggests that measurements with improved signal to noise might help.....	79

Figure 5.1.	Viscoelastic properties of collagen solutions with and without ultracentrifugation treatment at concentrations of (A) 0.7 mg/ml and (B) 4.7 mg/ml.....	83
Figure 5.2.	(A) Elastic and (B) viscous moduli increase with collagen concentration from 0.5 to 5 mg/ml (in 20 mM acetic acid). The viscous modulus of the solvent (20 mM acetic acid) is plotted in (B) for comparison. Values presented are averages over 10 independent measurements at each concentration of collagen, with error bars representing the standard error of the mean.....	85
Figure 5.3.	The reduced viscous modulus, G_R'' (filled triangles), is plotted along with elastic modulus for solutions of 5 mg/ml collagen. The solid lines at low frequency represent the expected Maxwell scaling of the moduli. At high frequency, slopes of the lines indicate possible frequency-dependent scaling of moduli for flexible ($\frac{2}{3}$) and semiflexible ($\frac{3}{4}$) polymers.....	86
Figure 5.4.	(A) Elastic and (B) reduced viscous moduli divided by sample concentration, c . While the lowest concentration of G' values appears to scale linearly with concentration, this is not the case for G_R''	90
Figure 5.5.	(A) Elastic and (B) reduced viscous moduli divided by the square root of sample concentration, c . The reduced viscous modulus, G_R'' , appears better to rescale with $c^{0.5}$ at high frequency, although not the elastic modulus.....	91
Figure 5.6.	(A) The viscosity of collagen solutions (obtained from G'' using Eq. 2.14) is also frequency-dependent and increases with collagen concentration. Black symbols connected with lines show the viscosity obtained for the solvent, which is in good agreement with that of water at room temperature (0.001 Pa.s). (B) Specific viscosity of collagen solutions at different concentrations shows a change in slope between 0.5 and 2 mg/ml collagen concentrations. Dashed line corresponds to slope of 0.5.....	93
Figure 5.7.	(A) Elastic and (B) viscous moduli for solutions of 5 mg/ml collagen probed with polystyrene beads (diameter $\sim 2 \mu\text{m}$) with two different surface chemistries: carboxylate-functionalized and amine-functionalized.	96
Figure 5.8.	(A) Elastic and (B) viscous moduli for a solution of 5 mg/ml collagen probed with polystyrene beads with two different diameters: $2 \mu\text{m}$ and $3 \mu\text{m}$. This work was performed in collaboration with Dr. Tuba Altindal, a postdoctoral researcher in the lab.	98

Figure 5.9.	Effect of addition of salt on viscoelasticity of collagen solutions. Comparison of (A) elastic and (B) viscous moduli for collagen solutions of 5 mg/ml. Note that in these measurements telopeptides removed collagen was used.	100
Figure 5.10.	Comparison of the collagen-related bands for untreated (including telopeptides), pepsin-treated, and commercially available pepsin-treated collagen solutions analysed by SDS-PAGE. Removal of telopeptides results in a shift of collagen bands to lower molecular weights. For each sample, two different amounts of collagen were tested to verify that the shift in the position of collagen band was not related to the amount of collagen loaded in the gel.....	102
Figure 5.11.	(A) Elastic and (B) viscous moduli for 1.5 mg/ml collagen with intact telopeptides (untreated, pH 2); collagen with telopeptides removed and pepsin and digested telopeptides still in solution (pepsin-treated, pH 2); and collagen with telopeptides removed by pepsin and purified away from pepsin and telopeptide fragments (pepsin-treated, salt precipitated, pH 3.3). Values presented are averages over 6 measurements in each sample and error bars are the standard error of the mean.	104
Figure 6.1.	Presence of beads at low concentration ($\sim 5 \times 10^{-4}$ % w/v) does not affect the kinetics of fibril formation. Figure shows the kinetics of fibril formation with 0.5 mg/ml collagen at $\sim 25^\circ\text{C}$ (measured via the plate reader).....	107
Figure 6.2.	Heterogeneity of properties is observed within a collagen gel sample prepared from 0.5 mg/ml collagen at room temperature. Plots here show the x-y trajectories from two different beads (different locations) over ~ 9 seconds. In these measurements, the beads were not optically trapped.	109
Figure 6.3.	Measured (A) elastic and (B) viscous moduli at different locations in collagen fibrillar gels (prepared from 0.5 mg/ml collagen at 21°C and $\text{pH}=6.9$). Note the large variation in properties at different positions (within either the same gel or gels prepared under identical conditions). The solid and dashed lines in (A) represent the independently measured average elastic modulus of the trap and its standard deviation ($G'_{\text{trap}} = 3.9 \pm 0.7 \text{ Pa}$) for the same laser power and bead size ($N=28$). In (B), the dashed line at high frequency is plotted to illustrate power-law scaling of $\frac{3}{4}$. For comparison, the solid and dotted lines plot the measured viscous modulus of water and of 0.5 mg/ml collagen in acidic solution, respectively. Gel data shown here include the maximal and minimal moduli measured in all of my experiments.	110

Figure 6.4.	Measured (A) elastic and (B) viscous moduli at different locations in a collagen fibrillar matrix formed from 1 mg/ml collagen and prepared at 30°C and pH=6.9. The solid and dotted lines plot the measured viscous moduli of water and of 1 mg/ml collagen in acidic solution, respectively. Overall, the heterogeneity of viscoelastic properties within the gel does not change substantially with this different collagen concentration and formation temperature. Measurements were performed at room temperature.....	111
Figure 6.5.	Uncertainties in trap modulus significantly affect observed power-law scaling. Here, two elastic moduli measured for collagen gels, G'_{gel} , are obtained by subtracting G'_{trap} from the measured values of $G'_{measured}$ (same symbols as used in Figure 6.3). See text for details on the shading.	113
Figure 6.6.	Heterogeneous microscale viscoelasticity is apparent even from the early growth phase of collagen fibril assembly. Measured (A) elastic and (B) viscous moduli at $f = 2$ kHz as a function of time during collagen self-assembly at 0.5 mg/ml (pH=6.9, 21°C). Solid and dashed lines in (A) show $G'_{trap} = 3.9 \pm 0.7$ Pa as described for Figure 6.3. The dot-dashed line in (B) plots the measured viscous modulus of water at $f = 2$ kHz. Triangles at zero time reproduce moduli measured at $f = 2$ kHz for 0.5 mg/ml collagen in acidic conditions (Figure 5.2), where assembly cannot occur. For comparison, the sigmoidal development of turbidity (Figure 3.5) is superimposed on the plot (solid line; right axis), rescaled vertically between solvent response and the maximum measured value of elastic modulus.	118
Figure 6.7.	Measured (A) elastic and (B) viscous moduli from the same measurements as in Figure 6.6 but here at $f = 100$ Hz.	119
Figure 6.8.	Measured (A) elastic and (B) viscous moduli in an assembling collagen fibrillar matrix, reproduced from Figure 6.6. In rare circumstances, it was possible to retain a given probe particle for measurements at multiple times. These results are indicated by filled symbols, and are connected by lines to guide the eye. A significant evolution in viscoelastic properties is seen at one location (solid line), while in another location, no significant change is observed (dotted line).	121
Figure 6.9.	This schematic compares the structural organizations of collagen molecules and gelatin [192]. The latter includes individual α -chains of collagen and regions of short triple-helical entwinements of the chains.	123

Figure 6.10.	Elastic and viscous moduli for 5 mg/ml collagen-gelatin and commercial gelatin (Knox gelatin) are identical within error. Although they are both greater than the corresponding moduli measured in solvent (20 mM acetic acid, circle symbols) alone, they result in much lower moduli than a similar concentration of collagen molecules in solution (Figure 5.2) and fibrillar gels with lower concentrations of collagen (Figures 6.3 and 6.4). Symbols represent mean values and error bars the standard deviations, for $N=10$ beads under each experimental condition.....	124
Figure 6.11.	Measured (A) elastic and (B) viscous moduli of 14 mg/ml commercial gelatin (Knox gelatin) exhibit significant spatial heterogeneity as sensed by the 2.1 μm probe particles used in these experiments. Different traces represent examples of independent measurements by different beads at different locations. Solid and dashed lines in (A) show $G'_{\text{trap}} = 3.9 \pm 0.7 \text{ Pa}$ as described for Figure 6.3.	126
Figure A.1.	Power spectrum of a 2.1 μm polystyrene particle trapped in water using four different laser currents.	150
Figure C.1.	An ideal theoretical power spectrum of a particle in water according to Eq. 2.5 (the Lorentzian function) with $f_c = 873 \text{ Hz}$ and $A = 0.0235 ((V/V)^2 \cdot \text{Hz})$	153
Figure C.2.	(A) Real and imaginary parts of the response function for a particle trapped in water, for a finite sampling rate of 100 kHz (solid lines) and as if it were sampled at an infinite bandwidth (dashed lines). (B) Elastic shear modulus obtained for the above conditions.....	154
Figure C.3.	The power spectrum of a particle in water obtained from particle's simulated motions in an optical trap. Parameters of the Lorentzian fit are similar to those in Figure C.1, and here, aliasing at high frequencies is apparent.	155
Figure C.4.	(A) Real and imaginary parts of the response function for a particle trapped in water, when it is sampled at finite sampling rate of 100 kHz (solid lines) when random noise is included and as if it were sampled at an infinite bandwidth with no noise (dashed lines). (B) Elastic shear modulus obtained for the above conditions. Blue circles are the averaged, blocked results of the elastic modulus with finite sampling (solid line). Inset: The data are replotted on a semi-logarithmic scale to show better the overall decreasing trend of elastic modulus at high frequency.	156
Figure D.1.	Structure of Alexa Fluor 647 carboxylic acid, succinimidyl ester.	157
Figure E.1.	Chemical steps for the ELISA experiment.	159

List of Symbols

A^*	Complex response function
c^*	Overlap concentration
D	Diffusion coefficient
D_t	Translational diffusion
D_r	Rotational diffusion
f	Frequency
f_c	Corner frequency
G'	Elastic modulus
G''	Viscous modulus
G''_R	Reduced viscous modulus
G^*	Complex shear modulus
$I(t)$	Scattering light intensity as a function of time
I	Ionic strength
\vec{k}	Wavevector
k_B	Boltzmann's constant
l_c	Contour length
l_p	Persistence length
M_w	Molecular weight
N_A	Avogadro's number
$p(f)$	Power spectral density of displacement
\vec{q}	Scattering vector
R	Radius
R_g	Radius of gyration
R_h	Hydrodynamic radius
S	Sedimentation coefficient
T	Temperature (in Kelvin)
ω	Angular frequency
$x(t)$	Particle's displacement as a function of time

$\gamma(t)$	Shear strain as a function of time
γ	Drag coefficient
δ	Phase lag
ϵ_0	Permittivity of free space
ϵ_r	Dielectric constant of the medium
η	Viscosity
η_s	Viscosity of solvent
η_{sp}	Specific viscosity
κ	Trap stiffness
λ	Wavelength
λ_D	Debye length
$\sigma(t)$	Shear stress as a function of time

Chapter 1.

Introduction

The goal of this thesis is to develop and apply a technique that can probe the viscoelastic properties of the protein collagen at different hierarchical structural levels. Collagen is a well-known family of structural proteins present in the majority of connective tissues in mammals and is responsible for their mechanical behaviours. It has the ability to make or to assemble into microfibrillar/network structures, which makes it an excellent example of a hierarchical biological material. Therefore, determining the mechanical behaviour of collagen from a single molecule to a network of entangled chains will contribute to understanding the correlation between its molecular structure and its mechanical properties. To do this, I apply a microrheology technique based on high-bandwidth particle tracking using optical tweezers, in order to probe the strength and local variations of mechanical properties of collagen at different hierarchies of structure.

This chapter gives a general introduction to the field. It first introduces collagen, its biochemistry and role in physiological functions. Then, one of collagen's important physical properties (viscoelasticity) is introduced followed by the science used to characterize this property (rheology). In order to interpret dynamics of and intermolecular interactions between collagens, some relevant concepts in polymer physics are defined and their ambiguities for collagen are discussed. Finally, the technique of microrheology is introduced as a method to locally characterize viscoelastic media. Several microrheology techniques are described, along with their strengths and limitations.

1.1. Collagen

Collagen accounts for approximately 30% of the total protein in the human body. It is the main structural protein in vertebrates. In several connective tissues such as

tendon, skin, bone and cartilage, it plays a critical role in strength and flexibility. Collagen is also the main component of the extracellular matrix, which gives structural support for cellular movement and growth [1–6].

Collagen has become a natural choice of biomaterial for medical applications because it is biodegradable and biocompatible [7]. It enhances cellular penetration, which makes it a potential biomaterial for use in scaffolds in tissue engineering such as for bone repair, ligament repair, artificial skin in plastic surgery, and oral wounds in dentistry [8–12]. In other examples, collagen systems (e.g. gels) are used for local drug delivery, an example of which is a collagen sponge with a differentiation factor, which allows cells to penetrate into the sponge, differentiate and form new bone [7].

There is also a wide range of connective tissue diseases including arthritis, osteogenesis imperfecta, Ehlers-Danlos syndrome, and many others arising from mutations in collagen, some of which are summarized in Table 1.1 [13–15]. Moreover, several chemical modifications associated with diabetes and aging [16–18] are likely to underlie the fact that modifications of the chemical composition of collagen impact its mechanical properties (such as loss of skin elasticity and bone toughness due to age-related modifications of collagen).

In many of these cases, collagen's mechanical properties play a substantial role on its function at the macroscale, while at the microscale scale its mechanics significantly affect cellular fate [19,20].

Table 1.1. List of major collagen types and information on their structure including contour length and higher order structure (if any), tissue localization, and diseases caused by genetic mutations. Information is adapted from [15,21].

Type	Contour length	Higher order structure	Localization	Disease
I	300 nm	Fibrillar	Skin, Tendon, Bone, others	Osteogenesis imperfecta, Osteoporosis, Ehlers-Danlos syndrome type VIIA, VIIB
II	300 nm	Fibrillar	Cartilage, Vitreous humor	Several chondrodysplasias, Osteoarthritis
III	300 nm	Fibrillar	Skin, Muscle (frequently associated with type I)	Ehlers-Danlos syndrome type IV, Aortic aneurysms
IV	390 nm	Non-fibrillar	All basal lamina	Alport syndrome
V	390 nm	Small fibers	Most interstitial tissues	
VI	150 nm	Microfibrils	Most interstitial tissues	
VII	450 nm	Dimer	Epithelia	Epidermolysis bullosa
VIII	130 nm		Some endothelial cells	
IX	200 nm		Cartilage (associated with type II)	Osteoarthritis
X	150 nm		Mineralizing cartilage	Schmid metaphyseal chondrodysplasia
XI	300 nm	Small fibers		Stickler syndrome

The characteristic feature of a collagen molecule is that it is composed of three polypeptide chains, the so-called α -chains, which have a highly repetitive sequence of amino acids, $(\text{Gly-X-Y})_n$. Here, X and Y can be any amino acids, often proline and hydroxyproline, and n may be >300 (depending on collagen type). This specific tripeptide motif of the α -chains allows them to organize in a triple-helical structure with glycine residues buried inside and the side chains of X and Y residues facing the outside of the helix [22].

Collagen molecules (fibrillar types) can self-assemble into fibrils with well-ordered organizations of single molecules along the fibrils. Subsequent assembly of these fibrils into networks or fibres can follow, which, depending on tissue type, may also include organization of minerals or other protein components [23]. Collagen mechanics are coupled throughout its assembly hierarchy, implying that changes in molecular-level interactions can impact higher-level mechanical response [24].

Only very recently have investigations on mechanical properties of single collagen molecules been undertaken [25,26]. The influence of the structure and mechanics of collagen at the single-molecule level on its mechanics at higher-order levels of structure has been investigated only by computational simulations [27,28]. Therefore, to date an integrated experimental approach is lacking to study the relationships between the mechanics of these different hierarchies of collagen structure.

In order to address this question of structure-function relationship, understanding the timescales, strengths and types of interactions between collagen molecules in solution, and the mechanism by which collagen molecules undergo assembly into fibrils is required. Furthermore, whether microscale heterogeneity of mechanics observed in fibrillar networks [29–31] can be controlled and the importance of the range of mechanical environments sensed about a cell on timescales relevant to regulatory mechanisms and motility remain open questions.

The study of physical and mechanical properties of collagen systems falls in the field of complex fluids. In this area of research, there is an extremely wide range of sample chemistries and topologies such as colloids, polymers, and biological materials. Complex fluids exhibit intermediate behaviour between a solid (purely elastic) and a fluid (purely viscous). The phenomenon is called viscoelasticity and is studied in the field of rheology.

1.2. Rheology and Viscoelastic Properties

Rheology is the science that studies the flow and deformation of a material. It aims to describe the interrelation between force field, deformation field, and timescale of a material's response to an applied force (or deformation). This may be in the form of an elastic response, in which the energy is stored through a fully reversible deformation, or in the form of a viscous response, in which the energy is dissipated through liquid flow, or as in the case of complex fluids by some behaviour in between (viscoelastic response) [32].

The response of a viscoelastic material to a disturbance (applied force or deformation) can be of various kinds depending on the timescale on which this response

is probed. A simple observation can be made with an experiment with silly putty (polydimethyl siloxane): the material flows when laid stationary but bounces when dropped [33]. That is, on short time scales, it has no time for structural rearrangements in response to the force and hence, will respond elastically. However, at long time scales, it deforms slowly but permanently. The inherent timescale of the material defines the boundary between these two responses [32].

In almost all biological tissues, viscoelastic response plays an important role in their active functions. This is because cells, structural proteins, and extracellular matrices are all viscoelastic materials [34]. For example, to successfully engineer a tendon or ligament, it is important to understand and replicate the time-dependent and time-independent properties of the material, otherwise, it may result in the lack of functionality or even total failure [35].

To study the viscoelasticity of materials by rheology, a simple shear is the most commonly studied type of deformation, because it can be applied to both solids and liquids. Conventional rheological characterization measures the in-phase and out-of-phase response of the material to an oscillatory shear strain $\gamma(t) = \gamma_0 \sin(\omega t)$, in which γ_0 is the amplitude of strain and ω is the angular frequency of oscillation, $\omega = 2\pi f$, where f is frequency in Hz. If the applied strain is sufficiently small such that the material's response is linear, the stress response is also sinusoidal and can be written as $\sigma(t) = \sigma_0 \sin(\omega t + \delta)$, where σ_0 is the stress amplitude and δ is the phase lag. This relationship is usually rewritten in the form of $\sigma(t) = \gamma_0 [G'(\omega) \sin(\omega t) + G''(\omega) \cos(\omega t)]$, where $G' = \frac{\sigma_0}{\gamma_0} \cos(\delta)$ and $G'' = \frac{\sigma_0}{\gamma_0} \sin(\delta)$. G' is in phase with the strain and is called the elastic or storage modulus and G'' is out of phase with the strain and is called the viscous or loss modulus.

To interpret rheological properties, it is usually useful to consider the elastic and viscous moduli to be the real and imaginary parts of the complex shear modulus, G^* which is defined as $G^* = G'(\omega) + iG''(\omega)$. When $G'/G'' \gg 1$, a material exhibits solid-like response [32]. For a simple solid, G' is frequency-independent as shown in Figure

1.1(A). On the other hand, when $G'/G'' \ll 1$, a material's response is liquid-like [32]. For a simple liquid the viscous modulus increases linearly with frequency (Figure 1.1(B)). In a viscoelastic medium, both elastic and viscous moduli can be frequency-dependent and their relationship may vary dramatically over the frequency range. An example of such a response is demonstrated in Figure 1.1(C) [36].

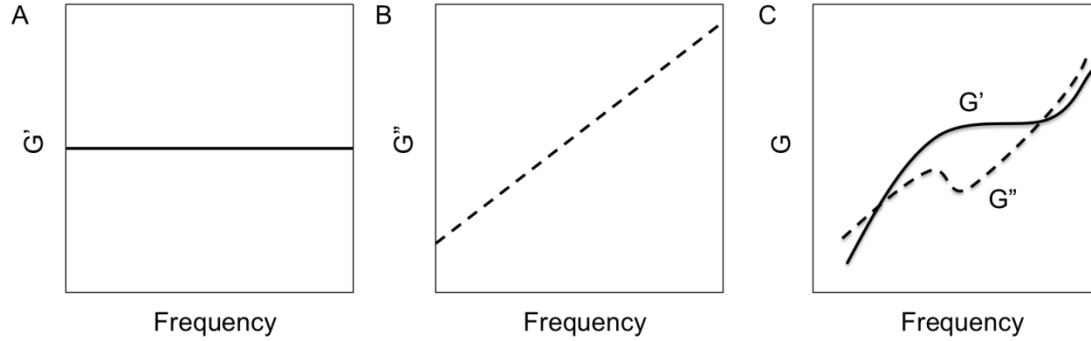


Figure 1.1. Illustration of shear modulus versus frequency for a (A) pure solid, (B) pure liquid (e.g. water), and (C) viscoelastic material.

Various models have been developed to describe the viscoelastic properties of materials. The simplest versions are based on the combination of two elements, a spring and a dash-pot (damper), which are responsible for the elastic and viscous behaviour of the system, respectively. The two most basic models are the Maxwell and Kelvin-Voigt models, which are shown in Figure 1.2 [32,37].

Maxwell model: This model is based on the combination of a spring and dash-pot in series, such that both elements feel the same stress. Here, the spring is responsible for the elastic shear modulus (G_0) and the dash-pot for the viscosity (η). According to this model, the applied stress relaxes with a single exponential decay equation, $G = G_0 \exp(-t/\tau)$, in which the characteristic time τ is equal to η/G_0 .

In the frequency representation, the Maxwell model describes elastic and viscous moduli as the following [37],

$$G'(\omega) = \frac{G_0 \omega^2 \tau^2}{1 + \omega^2 \tau^2}, \quad (1.1)$$

$$G''(\omega) = \frac{G_0 \omega \tau}{(1 + \omega^2 \tau^2)}$$

in which ω is the angular frequency and τ is the relaxation time. Based on these equations, at high enough frequencies, when $\omega\tau \gg 1$, G' approaches a plateau, $G' = G_0$ and the material behaves as an elastic body. At sufficiently low frequencies, when $\omega\tau \ll 1$, $G' \propto \omega^2$ and $G'' \propto \omega$ and the material behaves as a simple liquid. Figure 1.2(C) illustrates this expected viscoelastic behaviour predicted by the Maxwell model.

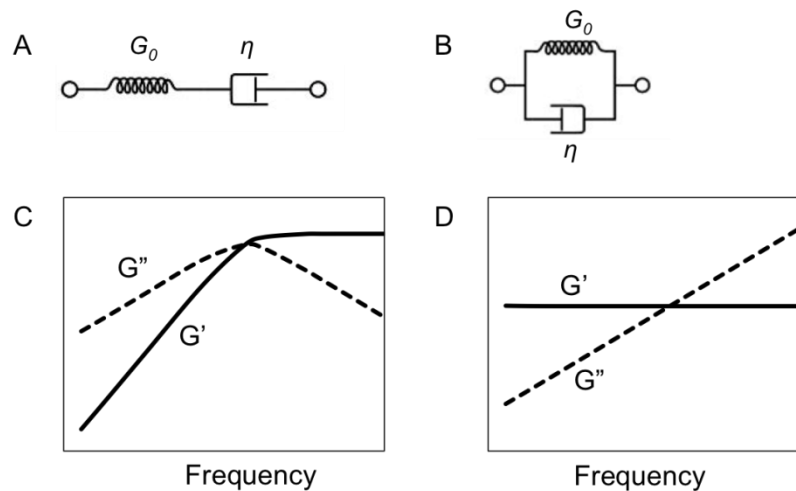


Figure 1.2. Schematic of (A) Maxwell and (B) Kelvin-Voigt models using a spring and dash-pot connected in series and parallel, respectively. Correspondingly, (C) and (D) illustrate elastic and viscous moduli of a viscoelastic material following the Maxwell and Kelvin-Voigt models.

Although this model is an idealized model of real systems, the predicted response has been seen in a variety of systems, even if only in a certain frequency range [32,37]. Gobeaux *et al.* [38] showed that the viscoelastic properties of collagen solutions at a concentration of 16 mg/ml are well described by the Maxwell model at low frequencies (Figure 1.3) [38]. They hypothesized that this observation is due to a single dominant intermolecular relaxation mode. However, at high frequencies different relaxation modes are involved (e.g. intramolecular relaxation modes).

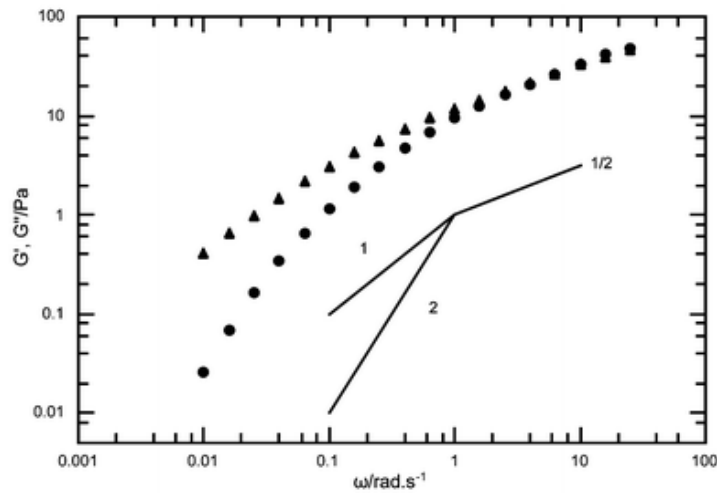


Figure 1.3. Elastic (circles) and viscous (triangles) moduli as a function of frequency for a 16 mg/ml collagen concentration collagen in 500 mM acetic acid. The low frequency behaviour is consistent with the Maxwell model. Figure is taken with permission from [38].

Kelvin-Voigt model: This model, which is based on a parallel arrangement of a spring and dash-pot (Figure 1.2(B)), such that both are subjected to the same strain. This model is appropriate for systems exhibiting solid-like behaviour at low frequency [37]. In this thesis work, we attempt to describe the viscoelastic response of molecular collagen systems with simple models. Because these collagens are predominantly viscous at low frequencies, their response should not be described by this model (Figure 1.2(D)), and instead, the Maxwell model is more appropriate.

These are two very simple models for describing viscoelastic properties of different systems, however, a single Maxwell or Kelvin-Voigt model can describe the behaviour of only a few real materials. In practice, combinations of these two models have been used to describe the viscoelastic properties of various systems [37].

In general, the viscoelastic properties of a polymeric system and their corresponding description by a theoretical model are associated with the microstructure of the material. The area of polymer physics studies the properties of microstructure in polymeric systems and helps us better understand the correlation between viscoelastic properties of the system and its microstructure.

1.3. Selected Topics in Polymer Physics

This section focuses on the perspective of polymer physics and briefly discusses some topics that are relevant to rheological studies. In this thesis work, the purpose of characterizing the viscoelastic properties of collagen is to understand the dynamics and interactions of collagens (strength and timescale) at different hierarchical levels. For that to be achieved, the first characteristic to be understood is the solution's concentration regime.

From very dilute solutions of polymer chains to a crowded solution (concentrated), molecular dynamics and intermolecular interactions vary. An example of this is in collagen self-assembly where its kinetics closely correlate with monomer concentration [39]. When polymer concentration is very low (dilute regime), the chains and their neighbours do not touch. Although at this low concentration it is not possible to study the intermolecular interactions (if any), one may characterize the molecular dynamics. By increasing the polymer concentration, the solution reaches a point where the effective volumes occupied by single polymer chains begin to overlap. This critical concentration is called the overlap concentration, c^* . Figure 1.4 illustrates the concept of overlap concentration. Above c^* , polymer chains start to physically contact, share their respective volumes with their neighbours, and hence, interpenetrate [40]. At high enough concentrations ($c > c^*$) both dynamics and intermolecular interactions govern the rheology of the system [41].

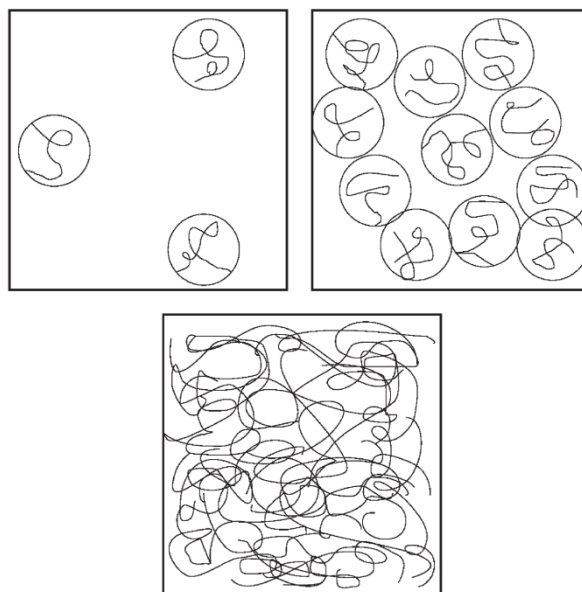


Figure 1.4. Illustration of concentration regimes: Left-top figure shows the dilute regime (when $c < c^*$), right-top figure corresponds to the critical condition of $c = c^*$, and bottom figure shows the concentrated regime ($c > c^*$). Circles represent hypothetical spheres with radius R_g . Figure is taken with permission from [42].

The overlap concentration is defined using a measure of an effective size of the polymer, its radius of gyration (R_g). R_g is calculated as the root mean square distance of the chain's parts from its center of mass. In the dilute limit, the effective volume that each polymer chain occupies is the volume of a sphere with the radius R_g [36,43]. In a polymeric system, the radius of gyration is related to the fully extended length of the polymer chain, its so-called contour length, l_c . (The larger the contour length, the larger the R_g value becomes.)

For a given contour length, flexibility of the molecule also controls the magnitude of R_g . That is, if the polymer molecule is not flexible (behaves as a rigid rod), its radius of gyration is significantly different from that for a flexible molecule, which can bend more easily and obtain a more compact conformation. An interesting example of this comparison was theoretically performed for polymethylene chains with a given contour length (degree of polymerization=5000, $l_c \sim 600$ nm) [44]. It was found that the molecule as a hypothetical rigid rod would have radius of gyration of 130 nm whereas that for a

hypothetical flexible form (random coil) would be 8.2 nm [44]. This example shows the strong dependence of radius of gyration on polymer flexibility.

In polymer physics, persistence length is a frequently used parameter to quantify the flexibility of a polymer chain. Persistence length, l_p , is defined as the distance traveled along the polymer backbone over which the average correlation between the tangent vectors are lost (it drops to $1/e$) [45], as shown in Figure 1.5. More informally speaking, when a polymer's contour length is much greater than its persistence length ($l_c \gg l_p$), the polymer chain can adopt a random coil conformation (similar to a three-dimensional random walk). By contrast, when a polymer's contour length is smaller than its persistence length ($l_c < l_p$), the polymer behaves rather like a rod. There are many relevant biological examples located at these two extremes and in between. Lambda-phage DNA with a contour length of 16 μm and persistence length of 53 nm (in a solution with high concentration of sodium chloride) is an example of a flexible form of a biopolymer [46]. An actin filament with an average length of several tens of μm and persistence length of the order of 10 μm is counted as a semiflexible polymer [47].

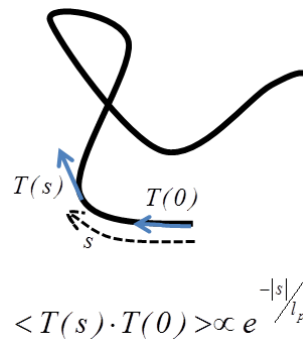


Figure 1.5. Definition of the persistence length, l_p , for a polymer chain.

For a collagen molecule, not all of the above polymer characteristics are well determined. It is known that the contour length of collagen (type I) is ~ 300 nm but values for its persistence length range from ~ 15 -170 nm [25,48–57]. Table 1.2 presents some of the values obtained from different studies along with their theoretically calculated radius of gyration and overlap concentration. This wide variation of persistence length predicts that collagen molecule behaves as anything between flexible random coil to a rigid rod-like molecule, an uncertainty that demands further study. This

variation may originate from the effect of the solvent [57], source of collagen, and/or characterization technique (e.g. imaging in two dimensions versus probing the response to an applied force). Here, I aim to determine collagen's flexibility by measuring the viscoelastic response of collagen solutions and interpreting this via appropriate theoretical models.

Table 1.2. A broad range of persistence length, radius of gyration, and overlap concentration has been found for collagen.

Technique	Persistence Length l_p (nm) [Ref.]	Radius of Gyration * R_g (nm)	Overlap Concentration ** c^* (mg/ml)
Rheometry	169-170 [48,49]	130	0.05
Viscometry	170 [50]	130	0.05
Dynamic Light Scattering	165 [51]	128	0.06
Static Light Scattering	156	125 [58]	0.06
Atomic Force Microscopy	165, 135, 12 [57] (solvent-dependent)	128, 116, 34 (respectively)	0.06, 0.1, 3 (respectively)
Viscometry	130 [52]	114	0.1
Electron Microscopy	60 [53]	77	0.3
Molecular Modeling	51 [54]	71	0.3
Molecular Modeling	16 [55]	40	1.9
Optical Tweezers	15 [25,56]	39	2.0

* Calculated with $R_g \approx \sqrt{\frac{l_c l_p}{3}}$ [59], assuming $l_c = 300$ nm.

** Calculated with $c^* \approx \frac{3M_w}{4N_A \pi R_g^3}$ [36], assuming $M_w = 300$ kDa. N_A is Avogadro's number.

For polymers studied at high frequency, both elastic and viscous moduli are assumed to increase with frequency based on $G'(\omega) \sim G''(\omega) \sim \omega^y$, where the exponent, y varies between 0.5 and 0.75 depending on the polymer's flexibility. For a flexible polymer ($l_p \ll l_c$), there are two basic models for the molecular dynamics: Rouse and Zimm models [60]. In both models, a polymer chain is represented by a chain of beads jointed via springs (Figure 1.6). The only difference is that in the Rouse model, hydrodynamic interactions between beads are not taken into account, while they are included in the Zimm model. Each of these models has its own prediction (0.5 in Rouse

and $\frac{2}{3}$ in Zimm model) for the scaling γ of the frequency-dependent viscoelastic properties. For a semiflexible polymer ($l_p > l_c$), the values of exponent are found to be greater ($\frac{3}{4}$ based on conventional theories [61,62] and $\frac{7}{8}$, recently found for certain high-frequency longitudinal relaxation mode [63]).

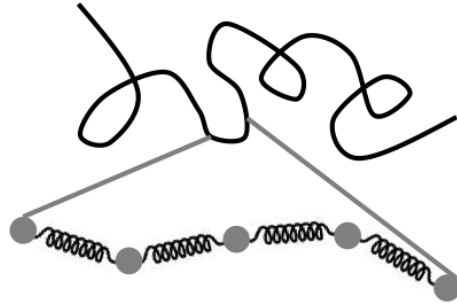


Figure 1.6. Representation of a flexible polymer chain by the bead-spring model.

In a polymeric solution with concentration greater than its overlap concentration, molecular response (e.g. Rouse behaviour of flexible polymers) dominates only at frequencies high enough, such that the timescale is too short for collective network dynamics. In other words, probing the viscoelastic properties of a polymer solution at high frequency can provide information on flexibility of polymer molecules. Given the ambiguities in collagen's flexibility, a rheological technique capable of high-frequency measurement would be a very useful tool. The following section describes a group of techniques, some of which can be used specifically to attain this goal.

1.4. Microrheology

Conventional rheometers, with various geometries such as cone-plate and parallel plates, are frequently used to probe rheological properties of materials such as polymer solutions, emulsions, and gels [64]. They typically require millilitre volumes of sample and can probe frequencies up to tens of Hz. Therefore, they are used to study the collective response of a material and dynamics associated with a large length scale (collective network dynamics), and do not give any information on the local properties and/or the short time-scale relaxation behaviour.

Microrheology, on the other hand, relates to the rheological studies of materials at the micrometer and sub-micrometer length scales. An excellent review of different techniques of microrheology and various studies has been written by Waigh [65], which forms the basis of this section. Although there is an extremely wide range of complex fluid systems studied with microrheology techniques, there is a distinct biological bias in the field, mainly because cells operate at the micrometre level and also because it is usually difficult to obtain large volumes of biological samples.

Historically, the field of microrheology stems from the observation of a biologist, Robert Brown, who found in 1827 that particles of pollen grains move in water [66]. This phenomenon remained unexplained until many decades later (1905), when Albert Einstein [67] theoretically described the molecular origin of so-called Brownian motion in terms of the collisions of surrounding solvent molecules with pollen. Shortly thereafter, in 1909, Perrin experimentally verified Einstein's theory and demonstrated the direct proportionality of the mean-square-displacement of a particle and time [68].

Another historical root is seen in Crick and Hughes' study [69] of the physical properties of cytoplasm, in which they created active magnetic microrheometers to probe micrometre-sized ferromagnetic particles. Decades later, thanks to improved computing power and intense coherent monochromatic light sources (lasers), modern microrheology techniques such as Particle Tracking Video microrheology [70], Atomic Force Microscopy [71], Diffusing Wave Spectroscopy [72], and Optical Tweezers [73] were developed.

Other than reduction in sample volumes, some advantages of microrheological methods include the local characterization of the system (smaller length scales than conventional rheology) and probing the response at high frequencies. The latter offers a novel means to relate the molecular dynamics of the material's constituents to the observed high-frequency behaviour. This has opened up an avenue for theoretical improvements on molecular origins of viscoelasticity of polymers, such as work by Morse [74,75].

The only bulk rheology method capable of probing viscoelasticity up to 10 kHz is the torsional oscillator technique which has been used by Fritz *et al.* [76]. Its main

drawback is being able to probe only at a series of fixed frequencies, and hence, this technique has not become widely used.

In contrast, microrheology techniques such as Diffusing Wave Spectroscopy and Optical Tweezers offer measurements of viscoelasticity over a wide range of frequencies up to MHz. This frequency range allows studying the rapid dynamics of relaxation of individual polymers in solution [65].

In the following, the major microrheology techniques currently used are highlighted: Particle Tracking, Diffusing Wave Spectroscopy, Atomic Force Microscopy, Magnetic Tweezers, and Optical Tweezers.

All these techniques are typically performed using micron-sized particles within the sample of interest, which are either actively manipulated or their thermal motion is passively monitored. The former method, which is called active microrheology, uses an external force to move a particle and monitor its response. The latter does not apply any force and simply monitors the motion of the particle(s); this method is called passive microrheology [65].

Particle tracking: This technique is the most basic form of microrheology, and is based on tracking the motion of micro-particles embedded in a medium using video microscopy. Measuring the trajectories of individual probe particles allows studying the spatial heterogeneity in the microstructure of a system [77]. Its frequency range is typically on the order of 50 Hz [78]. Its resolution may be tuned with different optics, though it is typically on the order of 10 nm [79]. Examples of this type of measurement on biological samples can be found in [80,81].

As a modification of this basic technique, Crocker and Grier [79] introduced two-particle tracking, where the cross correlation of particles' motion can be used to more accurately characterize inhomogeneous materials.

Diffusing Wave Spectroscopy: This technique uses multiple scattering from monodisperse colloidal probe particles embedded in a viscoelastic material to probe its microrheological properties [82]. The photon correlation electronics used for this method

offer a high-frequency readout (up to 1 MHz). The technique has been widely used for different complex fluid systems [82,83].

Atomic Force Microscopy: This technique is based on attaching a micro-particle to the cantilever of an atomic force microscope and oscillating it above the surface of interest to obtain the viscoelastic properties of the material as a function of frequency [71]. In a different type of study both cantilever and the surface can be oscillated to study the dynamics of a single molecule [84]. Some of the limitations of this method are that an external force always has to be present (active microrheology) and the maximum possible resonance frequency is typically a few kHz.

Magnetic Tweezers: This technique is based on manipulating and monitoring magnetic micro-particles embedded in a viscoelastic medium. Although with magnetic tweezers relatively high forces can be applied (~2000 pN), which extends the measurable range of moduli, the frequency range is below a kHz [85].

Optical Tweezers: In this technique, the position of the embedded micro-particle is monitored using laser light, which also traps the particle and prevents its long-range diffusion. This allows for the localized measurements of viscoelastic properties. This technique can also provide high-frequency measurements (up to 1 MHz) [86]. Additionally, both passive and active microrheology can be performed with this technique, as well as single-particle and two-particle measurements [87,88]. Microrheology based on optical tweezers has been performed for example on human cells [89], actin [61,90,91], DNA [92], and hyaluronic acid [93].

A single-particle, passive microrheology technique based on optical tweezers is used in this thesis work to measure the viscoelastic properties of collagen-based systems. This allows us to access the properties at relatively high frequencies (tens of kHz), where discussions on molecular dynamics and flexibility of collagen become possible. In addition, the timescale of intermolecular interactions can be studied by determining the frequency at which the elastic and viscous moduli become equal. Furthermore, this technique makes it possible to probe the heterogeneity of viscoelasticity in self-assembled collagen structures.

My work starts with the development of an optical-tweezers-based microrheology technique, the results of which are verified for a known system (Chapter 2). Before applying the technique to collagen systems, collagen structure and self-assembly are (microscopically and kinetically) characterized (Chapter 3), followed by a series of experimental studies on collagen size to determine appropriate concentration ranges for the microrheology experiments (Chapter 4). Next, the developed microrheology technique is applied to collagen solutions, first to study the dynamics and timescales of intermolecular interactions at the molecular level (Chapter 5). Then, the viscoelasticity of collagen is studied at the fibrillar level during self-assembly, to monitor the development of heterogeneity in collagen network structures (Chapter 6). Finally Chapter 7 summarizes the outcomes of this research followed by suggesting further directions of studies.

Chapter 2.

Optical-Tweezers-Based Microrheology

Among the microrheological techniques introduced in the previous chapter, optical tweezers was chosen in this thesis. This technique not only allows us to locally probe viscoelastic properties of a sample, but also provides the ability to characterize these properties at a high bandwidth (up to ~ 1 MHz). This chapter presents a brief introduction to the principles of optical tweezers, followed by a detailed description of our apparatus and data analyses for microrheological characterization.

2.1. Principles of Optical Tweezers

In the 1970s, Arthur Ashkin established that it is possible to optically trap and manipulate particles with laser light [94]. He demonstrated that optical forces exerted by a highly focused beam of light on a micron-sized dielectric particle could trap and manipulate the particle. This work led to development of the “optical tweezers” instrument, originally called the “single-beam gradient force optical trap” [95]. Since then, optical tweezers have been extensively employed for physical applications such as colloidal physics [96,97] as well as biological applications, which will be discussed more in the following paragraphs. A comprehensive review on the principles of optical trapping and its biological applications has been written by Neuman and Block [86].

Given that optical tweezers can be used to apply forces on the order of piconewtons, measure displacements on the order of nanometers, and read out these measurements with frequencies of up to 1 MHz, they have been successfully used as a tool in diverse biological studies [86]. Examples include manipulating bacteria [98,99], measuring the mechanical properties of human red blood cells [100] and cancer cells [89], study of forces exerted by molecular motors at the single-molecule level [101] and

within entangled filamentous actin networks [102], and stretching single DNA molecules [103] and proteins such as collagen [25].

Extending the manipulation capabilities of optical tweezers has also been accomplished using modulation of the optical wavefront in order to create multiple optical traps and manipulate them independently in three dimensions. Holographic optical tweezers are used for this purpose [104,105]. They are capable of creating complex patterns of light foci (in 3D) and dynamically steering them in real time, which has been applied for a wide range of manipulation experiments [106,107]. A related study on the traps' positional stability is presented in [108]. In addition, in Chapter 7, this technique is proposed for performing two-particle microrheology to study non-homogenous systems.

The physics describing the confinement of micron-sized particles can be explained by the interaction between the laser beam and probe particle, polystyrene microspheres in our experiments. Mie theory represents a complete solution of Maxwell's equations for the interaction of electromagnetic radiation with spherical particles[109]. Limiting cases, in which the particle's radius (R) is either much larger or much smaller than the wavelength of the laser (λ), the geometric optics model and the Rayleigh regime respectively, are generally used to describe the physics of optical trapping [86] and are outlined in the following paragraphs.

The condition for the geometric optics regime is satisfied if the particle's radius is much larger than the wavelength of the trapping laser ($R \gg \lambda$). Simple ray optics theories can be used to calculate the forces. The interaction between the particle and the laser beam originates from the conservation of momentum and the difference in refractive index between medium and the particle. Photons carry momentum. When they interact with a particle with a different refractive index than the medium, their directions will be changed by refraction, reflection, and/or absorption. Since absorption of light by the particles used here is minimal, I consider only refraction and reflection. Both of these processes lead to a change in the light's momentum. Because momentum should be conserved, the interacting particle experiences an equal and opposite momentum change, and hence experiences a force $\vec{F} = \frac{d\vec{p}}{dt}$, where \vec{p} is momentum. As shown in Figure 2.1(A), the force exerted on the particle by light has two components: scattering

and gradient forces. The scattering force is due to reflection of the incident light by the particle. This is such that for an isotropic particle (e.g. microsphere) centered on the optical axis, all scattering forces will cancel each other out except along the optical axis, where they act to push the particle along the direction of beam propagation. The gradient force is produced from refraction of the laser light: if the probe particle has a higher refractive index than the medium, the force will be directed in the direction of the field gradient, *i.e.* towards the higher light intensity as shown in Figure 2.1(B).

Therefore, when a laser beam with a Gaussian intensity profile is focused, it produces a gradient force on the particle and pulls it toward the focal point which has the highest intensity in the profile. If the bead is displaced laterally from the focal point, the beam will be deflected and produce a restoring force on the bead as shown in Figure 2.1(B). When a high-numerical-aperture lens is used to create the trap, the laser light will have a high gradient of intensity along the optical axis near the focal point. Therefore, the gradient force becomes significant enough along the optical axis that it cancels out the scattering force; this creates a stable trap in three dimensions.

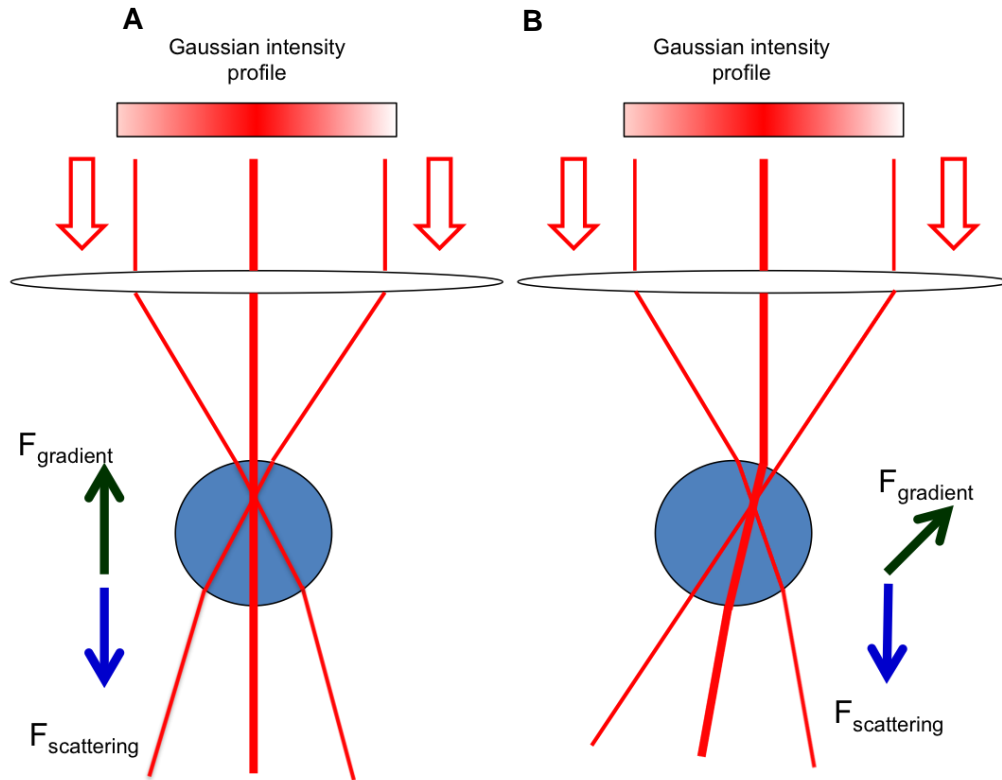


Figure 2.1. Gradient and scattering forces, produced from refraction and reflection, respectively, exerted by a laser beam with a Gaussian intensity profile on a microsphere, within a medium which has lower refractive index than the particle, are shown with arrows in each figure. (A) When the bead is centered in the beam, there is no net force perpendicular to the optical axis, while when it is slightly off-centered, (B) a net force perpendicular to the axis pushes the bead towards the maximum intensity.

In contrast, for the light-matter interaction to be in the Rayleigh regime, the particle's radius must be much smaller than the wavelength ($R \ll \lambda$). Here, the optical forces can be computed by treating the particle as a point dipole induced by the electromagnetic field of the laser. In this regime, for a sphere with radius R , the scattering force is given by [86]:

$$F_{\text{scat}} = \frac{I\sigma n_m}{c}, \quad (2.1)$$

$$\sigma = \frac{128\pi^5 R^6}{3\lambda^4} \left(\frac{m^2 - 1}{m^2 + 2} \right)^2,$$

where I is the incident light intensity, σ is the scattering cross section of the particle, n_m is the refractive index of the medium, c is the speed of light in vacuum, and m is

the ratio of the particle's refractive index to that of the medium. The gradient force arising from the dipole interacting with the electric field of the laser is shown to be [86]:

$$F_{grad} = \frac{2\pi\alpha}{cn_m^2} \nabla I, \quad (2.2)$$

$$\alpha = n_m^2 R^3 \left(\frac{m^2 - 1}{m^2 + 2} \right),$$

where α is the polarizability of the sphere. Similar to the geometric optics regime, a gradient force is applied in the direction of the highest gradient if the refractive index of the particle is greater than that of the medium.

When the particle's radius is comparable to the wavelength ($R \approx \lambda$), neither of these approaches is valid and more complicated electromagnetic theories are required. Mie scattering is the corresponding theory describing this regime [110]. Although the majority of biophysical studies including the current work fall in this intermediate regime, understanding the net effect of the laser on the trapped particle is sufficient for this study.

As explained above, when the bead is displaced from the center of the trap, it experiences a force that increases with displacement. In other words, the optical trap creates a potential well in which large-range motion of the particle is restricted although it still has short-range thermal fluctuations. As schematically illustrated in Figure 2.2, this system can be described as a Hookean spring where the restoring force, F , is proportional to the displacement from the equilibrium position, x :

$$F = -\kappa x, \quad (2.3)$$

where κ is the spring constant (trap stiffness) and is proportional to the intensity of light. This harmonic approximation is valid for small displacements of the trapped particle [86], the range used for the work described in this thesis.

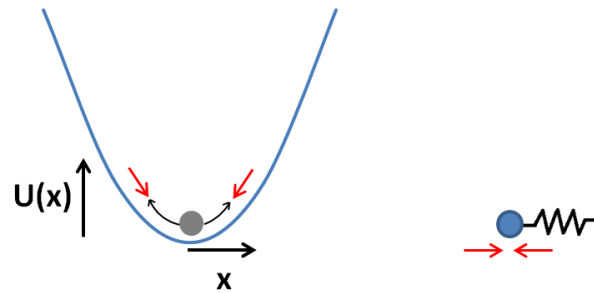


Figure 2.2. Schematic shows a bead in a potential well (blue line) created by an optical trap. The horizontal and vertical axes represent displacement from the center of the trap (minimum position in the well) and potential energy, respectively. The trap acts as a Hookean spring (right) where the force exerted on the bead is proportional to its displacement from the center of the trap. (Red arrows show directions of the forced motion.)

2.2. The Optical Tweezers Apparatus

Figure 2.3 shows a schematic diagram of our home-built optical tweezers apparatus, for which details have been previously reported [108,111]. In order to reduce mechanical noise, the whole setup is built on a vibration-isolated optical table. An infrared (IR) laser (Spectra Physics, J20-BL-106C, 4 Watt CW, 1064 nm) is used for trapping. The laser beam passes through an optical isolator and is expanded to a diameter of approximately 8 mm. Then a combination of a half-wave plate and polarizing beam splitter cube allows for manual adjustment of the laser power in the experiment (see Appendix A). Typical laser powers directed from the cube and used here were 100-150 mW. After passing the cube, mirror M1 reflects the beam onto the liquid-crystal display, which is a Spatial Light Modulator. This part provides the ability to holographically trap particles and control their positions in three dimensions; however, I have not used this ability for the current thesis. Thus, for the purpose of this work, the SLM acts as a mirror. (Holographic trapping is discussed in [108] and in Chapter 7.) After passing through lenses and mirror L1, M2 and L2, the laser beam is sent to a water immersion objective lens with high numerical aperture (Olympus UplanApo/IR, 60 \times , 1.2 NA, water immersion, reference focal length $L=180$ mm) in order to create a trap (tight focus) inside the sample chamber. After laser light passes through the chamber, a second objective lens collects it, and the dichroic mirror, D2, and lens, L3, direct it to a

quadrant photodetector (QPD; QP154-Q-HVSD, Pacific Silicon Sensor). The position of the QPD and lens L3 are set such that displacements of the laser in the back focal plane of the second objective lens are reimaged on the QPD. The QPD has four photodiodes each of which is in one quadrant. As shown in Figure 2.4, the analog circuitry outputs voltage V_x (the difference between the total voltages on the photodiodes located on the right and left) and V_y (similarly for the vertical direction) as well as the total voltages on all quadrants (Sum). V_x and V_y are proportional to the actual position (x and y directions) of the laser light on the QPD, and hence to the displacement of the trapped particle (Figure 2.1). The voltage output of the QPD is sampled at the desired bandwidth (here, 100 kHz) by a DAQ board (National Instruments, PCI-6052E) on the computer. Then, in order to eliminate the effect of light intensity variation, V_x and V_y are both normalized by the total voltage (Sum). The resultant data are analyzed as will be described in Section 2.4.

Moreover, the trapped particle is imaged by illuminating light directed into two cameras: a CCD camera (Point Grey Research, FL2-03S2M) that runs during operation at typical video frame rates for real-time observations; and a high-speed CMOS camera (PCO, 1200 hs, 1280×1024 pixels, pixel size 12×12 μm^2) that provides the high bandwidth (>1 kHz) required for our displacement measurements. The high-speed camera images were calibrated for position detection (pixel to μm conversion) using a stage micrometer. In this thesis, images were then analyzed to calibrate the QPD signal (Volts) to displacement (μm) of each probe particle, as will be described in Section 2.4.

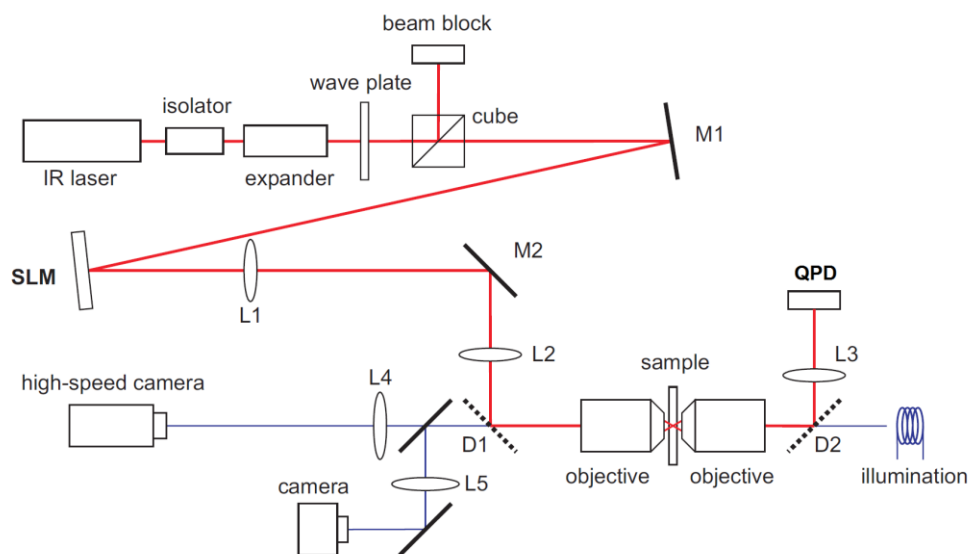


Figure 2.3. Schematic diagram of our optical tweezers instrument. Figure is adapted with permission [111].

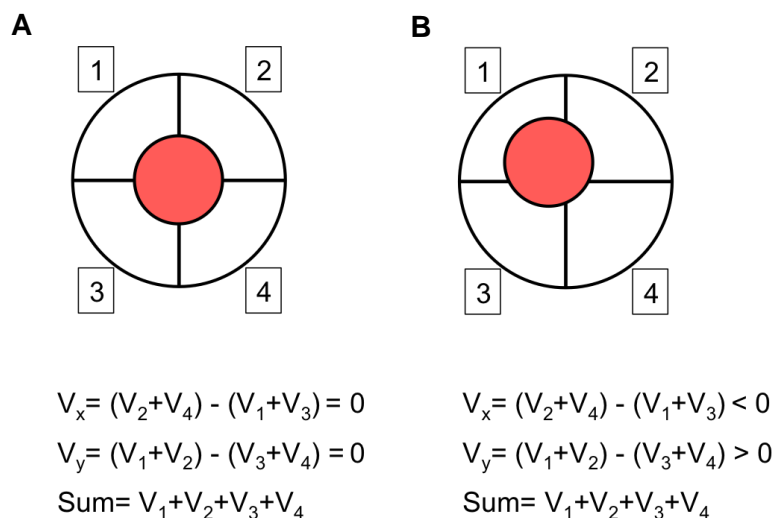


Figure 2.4. The position of the light spot on the QPD surface determines the voltages V_x and V_y , values of which are calculated as the differences between the output voltages from the right and left, and up and down, respectively. The total voltage on the four quadrants also is calculated as the Sum value. When (A) the light spot is located at the center, both V_x and V_y are zero, while (B) when it is off-centered they are both non-zero values (with the same Sum value).

One technical problem with the high bandwidth readout of QPDs is the limited response time of conventional photodetectors at a wavelength of 1064 nm. As Berg-

Sørensen *et al.* [112] have described, parasitic filtering of a photodiode's detection is caused by silicon's reduced transparency to 1064 nm light. Photons are absorbed and create charge carriers mainly in the n-layer (where they have to be transported via thermal diffusion) rather than the depletion area (where they are detected in nanosecond timescales). This will have a low-pass filter effect and unintentionally the signal will be lost at high frequencies. To overcome this issue, the photodiode used here incorporates dopants to increase response time to 1064 nm wavelength.

2.3. General Sample Preparation for Microrheology Experiments

Trapping of particles occurs in a sample chamber made of two microscope coverglasses separated by a gasket cut from Parafilm, which is then heated to melt and seal (thickness $\sim 100 \mu\text{m}$). A diagram of the sample chamber is shown in Figure 2.5. For the experiment, the sample chamber is mounted on a three-axis stage, allowing it to be positioned in three dimensions relative to the optical trap.

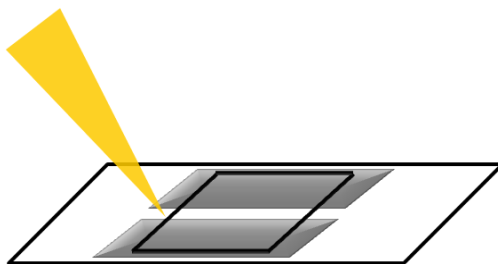


Figure 2.5. Diagram of a sample chamber consisting of two coverslips sandwiching two pieces of parafilm (in gray). A micropipettor can be used to inject the sample (by capillary flow) into the chamber.

For microrheology experiments, polystyrene microspheres (Spherotech) were added to the system of interest at a final concentration of $\sim 5 \times 10^{-4}\%$ w/v. This low concentration of probe particles ensures that one could still search within the sample and find probe particles to trap while there are not too many beads available to change the properties of the medium itself. Details of size and surface chemistry of the microspheres are discussed later in the Experimental section of each chapter.

Approximately 20 μl of prepared samples were pipetted into optical tweezers sample chambers, and the edges were sealed with candle wax to prevent evaporation. All measurements were conducted at room temperature (21°C).

2.4. Principles of Analyses for Microrheology

As described in the Introduction (Chapter 1), the thermal fluctuations of a particle can be used to obtain viscoelastic properties of its host medium. The following procedure has been used to calculate those properties; it is illustrated in Figure 2.6 as the fundamental processing steps in one-particle passive microrheology. It involves tracking the position of a bead within the medium as a function of time (normalized V_x), $x(t)$, as an input and performs analyses to obtain the characteristic properties of the medium as the frequency-dependent complex shear modulus, $G^*(f) = G'(f) + iG''(f)$, where G' and G'' are elastic or storage modulus and viscous or loss modulus, respectively. These steps were developed by others [113] and were used here with slight modifications as needed.

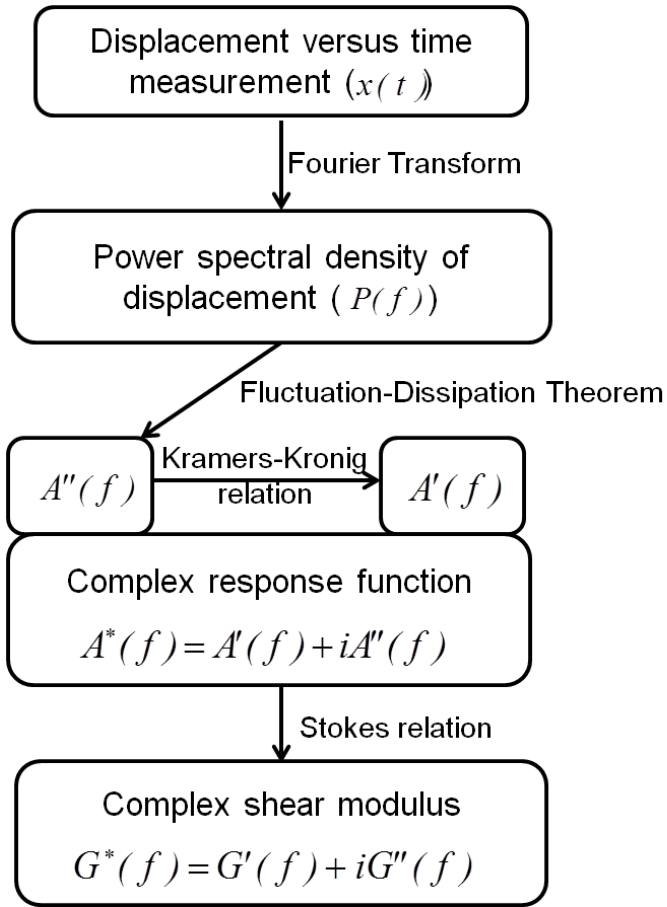


Figure 2.6. Flowchart diagram of analysis for microrheological measurements using optical tweezers. The details are described in the text.

Power spectral density: Starting with the particle's displacement obtained from the signals of the QPD (deflection of laser light due to the displacement of probe particle), the first step is to calculate the power spectral density (PSD) of the particle's position. The PSD of a signal is calculated by the square of its transformation from the time to frequency domain (Fourier transform):

$$P(f) = \frac{2|\tilde{x}(f)|^2}{T_{msr}}. \quad (2.4)$$

Here, $\tilde{x}(f)$ is the Fourier transform of the particle's position, $x(t)$, which is obtained from the QPD signal in Volts. T_{msr} is the measurement time. Therefore, $P(f)$ possesses units of V^2/Hz . Because in this work, the signal is normalized by the total

intensity on the photodetector, $P(f)$ is reported as $(V/V)^2/\text{Hz}$. QPD voltages were usually collected at 100 kHz for a duration of 100 seconds. Data from each second were Fourier transformed separately using a LabVIEW program ($T_{msr} = 1\text{ s}$), then in order to reduce noise, averaged power spectra were calculated from the 100 sets of 1-second measurements. A typical averaged power spectrum obtained for a 2.1 μm polystyrene bead trapped in water is shown in Figure 2.7.

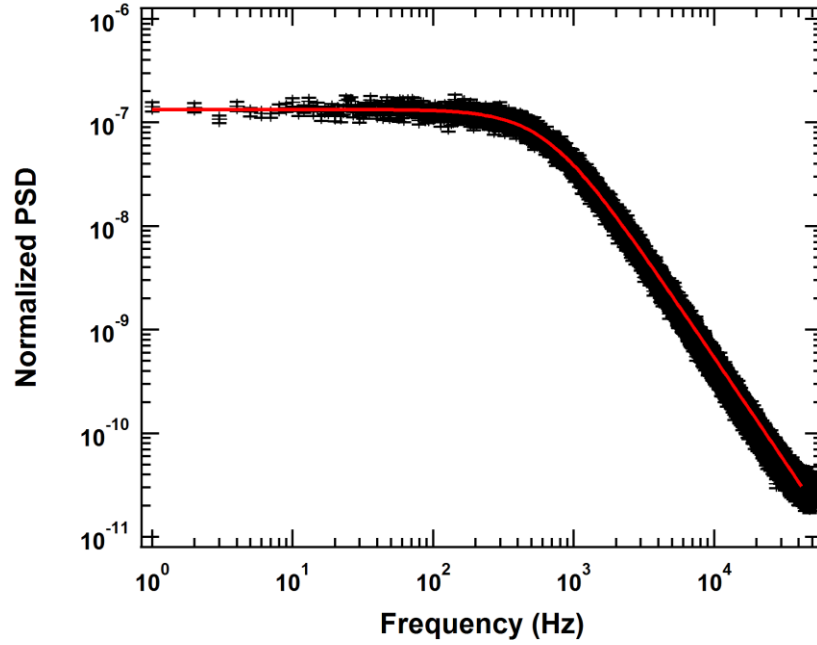


Figure 2.7. Power spectrum of a 2.1 μm polystyrene particle trapped in water. The red line shows the corresponding fit of Eq. 2.5 to this data. Fitting parameters were $A = 0.054 \pm 8.4 \times 10^{-5} ((V/V)^2 \cdot \text{Hz})$, $f_c = 638 \pm 28\text{ Hz}$.

It has been shown that for Brownian motion of a particle in a purely viscous medium (e.g. water), the PSD is described by a Lorentzian function [114]. The following equations describe this.

$$P(f) = \frac{A}{(f^2 + f_c^2)}, \quad (2.5)$$

$$A = \frac{D}{\pi^2},$$

where D is the diffusion coefficient of a freely moving particle and is equal to the ratio of the thermal energy and drag coefficient, $\frac{k_B T}{\gamma}$, in a purely viscous medium (k_B is Boltzmann's constant, T is the temperature in Kelvin, and γ is the drag coefficient). f_c in Eq. 2.5 is the corner frequency of the trap; this critical frequency marks the transition between the low frequency plateau of $P(f)$ corresponding to restricted long range motion (at longer times) of the probe particle due to the trap and an f^{-2} decay at high frequencies. This latter behaviour, specifically, corresponds to the short-range diffusive motion of the probe particle (inside the harmonic potential well of the trap; Figure 2.2) because the mean squared displacement of the particle increases linearly with the time for this travel. The value of the corner frequency can be used to calculate the stiffness of the trap, which physically corresponds to the spring constant in Hooke's Law (Eq. 2.3):

$$\kappa = 2\pi\gamma f_c, \quad (2.6)$$

where γ , the drag coefficient, is defined as:

$$\gamma = 6\pi\eta R. \quad (2.7)$$

Here, η is the viscosity of the solvent, and R is the radius of the probe particle. A fit to Eq. 2.5 is shown in Figure 2.7. (Note that in this thesis $P(f)$ is the single-sided Power Spectral Density.)

The trap stiffness depends both on the characteristics of the instrument such as laser wavelength, the objective's numerical aperture and laser power, and on the characteristics of the sample including refractive index of the particle and medium, and also the size of the probe particle. The greater the trap stiffness, the more constrained are the particle's movements. In the microrheological measurements performed here, constraining the long-range motion of the particle is an advantage of the method because it allows studying the local properties of the medium. Conversely, a lower stiffness of the trap is more desirable because the particle will experience less external stiffness due to the trap and thus the influence of the thermal fluctuations of surrounding molecules will impact its motion relatively more. Later in this chapter, correction of the

complex shear modulus for the effect of the trap will be discussed and verified for different laser powers (trap stiffnesses).

Because the trap stiffness is related to the refractive index of the medium (relative to the probe particle), it is important to have information on the refractive index of collagen solutions. The refractive indices of collagen solutions of different concentrations were measured using a bench-top Abbe refractometer at 21°C (Zeiss, ambient light as the light source located in Dr. Haunerland's lab). As shown in Table 2.1, the maximum difference between the refractive index of collagen solutions and solvent was 0.12%, which is not significant for our trapping experiments. Therefore, adding collagen in this concentration range should not change the trap stiffness.

Table 2.1. Refractive indices of collagen solutions compared with solvent (20 mM acetic acid) at 21°C

Collagen Concentration (mg/ml)	Refractive Index (± 0.0001)	Refractive Index change (%)
5	1.3339	0.12
4	1.3335	0.09
2	1.3331	0.06
1	1.3329	0.04
0.5	1.3326	0.02
0.25	1.3325	0.01
0 (20mM acetic acid)	1.3323	0
0 (water)	1.3323	0

In order to express the PSD in physical units ($\mu\text{m}^2/\text{Hz}$ rather than V^2/Hz), a conversion factor has to be applied. This factor depends not only on the refractive index of the particle, which is identical for all of our beads, but also on the particle size. Due to the fact that there is always some polydispersity in particle size, the conversion factor was determined as follows for each bead, separately.

The position of the trapped particle can be monitored in two ways, via the laser deflection and by imaging with the camera. By correlating position measurements by the QPD, in Volts, with those by the camera, in μm , one can extract this conversion factor. For a bead in a trap, the thermal motion is very restricted, to the order of a few tens of nm or less. Because the position detection resolution for both camera and QPD is on the

order of 1 nm, the conversion factor can be determined more reliably if the bead is intentionally displaced in x and/or y directions, which provides a wider range of displacements on the order of hundreds of nm. Here, displacements were done manually by shifting the chamber back and forth using the stage holder knobs. If this is done gently but quickly, hydrodynamic drag forces displace the bead while it remains within the harmonic range of the trap. For each bead, position measurements were collected simultaneously by the QPD and high-speed camera (at different rates, 10 kHz and 500 Hz, respectively). Images from the camera were then analyzed using a LabVIEW program written by Astrid van der Horst [111] based on convolution analyses. For that purpose, a template image of the bead (usually from the first frame) is selected, which is compared to the next frame and the convolution of their spatial intensity distributions is calculated. The template is moved pixel by pixel throughout the desirable search area of the second frame until the highest value for the convolution is achieved, which corresponds to the best match between template and current frame. The sub-pixel accuracy of bead position is obtained by fitting a two dimensional parabolic surface to the constructed matrix of the convolution values. The maximum of this surface gives position of the bead in this frame. This process is repeated for each frame subsequently in order to obtain the position of the bead over time.

In order to temporally align measurements by the QPD and by the camera, both illumination light and laser beam were blocked by quickly inserting a card between the second objective and mirror D2 (Figure 2.3). This was done before and after each manual shifting of the sample chamber. Figure 2.8(A) shows an example of the particle's position versus time measured with the camera (on the left axis) and by the QPD (on the right axis), excluding the blocking parts. Figure 2.8(B) replots a section of the results to obtain the conversion factor. In order to have a uniform distribution of data points (not accumulated at the equilibrium position), the obtained data in Figure 2.8(A) were divided into sections, conversion factors were found for each section, from which the averaged value was determined for later use.

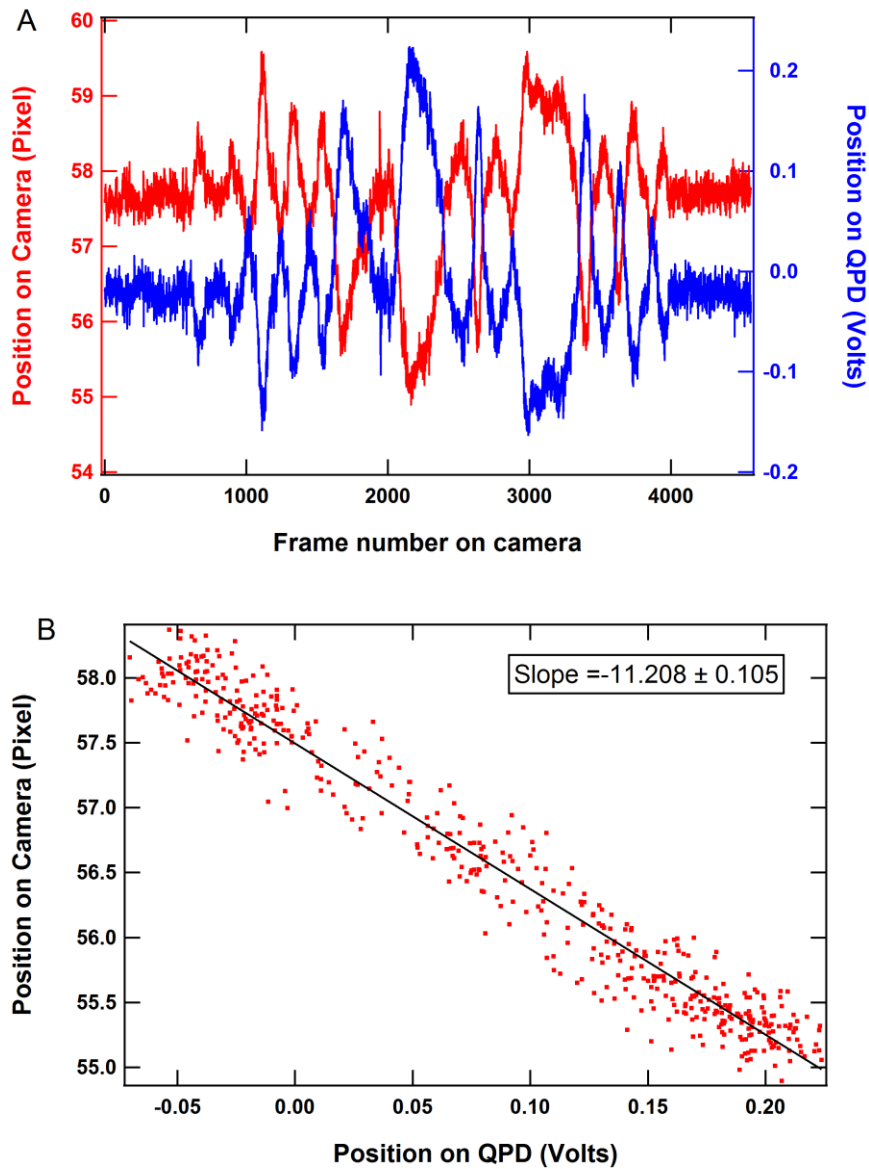


Figure 2.8. (A) Positions measured by the camera (red line) plotted together with the displacement read out by the QPD (blue line) when the particle is intentionally displaced back and forth within the trap. (B) A subset of the data from (A) are replotted to extract the conversion factor (here, 1 Volt = 11.2 pixel and because in our setup 1 pixel = 52.0 nm, 1 Volt = 0.582 μm).

Now that the conversion factor is calculated, the PSD can be converted to displacement units and comparisons between power spectra for different particles and solution conditions become meaningful. Figure 2.9 shows power spectra obtained for beads (diameter ~ 2.1 μm) in water and in a collagen solution (2 mg/ml). A first striking observation is that the PSD at high frequency scales differently with frequency for water

compared to collagen solution. A scaling factor of -2 in the high-frequency region is expected according to the Lorentzian function (Eq. 2.5) since water does not have elasticity. However, this behaviour significantly changes for the collagen solution. The smaller slope seen for collagen solution suggests that the particle exhibits subdiffusive motion. Such anomalous diffusion has also been noted in several other viscoelastic media such as inside living cells [115] and actin networks [80]. This observation for collagen is evidence that in collagen solutions elasticity is present along with viscosity.

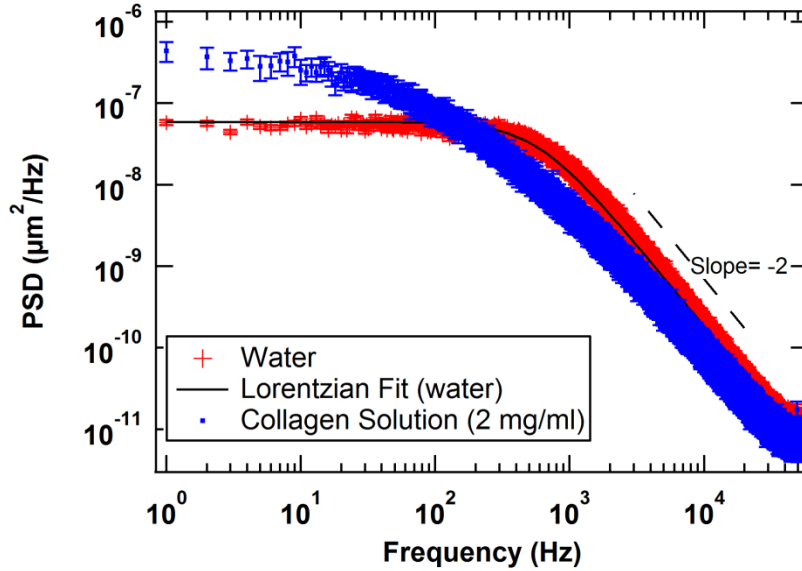


Figure 2.9. The power spectrum of a particle in water (red crosses) is significantly different from that in a collagen solution of 2 mg/ml concentration (blue dots). The latter does not show a -2 slope at high frequency (dashed line), which is a characteristic of normal Brownian motion in purely viscous media. The red line shows the corresponding fit (Eq. 2.3) to the data obtained from water. Fitting parameters were $A = 0.0185 \pm 2.5 \times 10^{-5} \text{ (}\mu\text{m}^2 \cdot \text{Hz)}$ and $f_c = 638 \pm 28 \text{ Hz}$. This value of A corresponds to a bead radius of $1.17 \text{ }\mu\text{m}$, in agreement with the stated size.

Complex response function: As shown in Figure 2.6, the next step for data analysis is to determine the complex response function using the fluctuation-dissipation theorem followed by the Kramers-Kronig relation [73,113,116]. All of the following steps were performed in a program I wrote in MATLAB software. The complex response function relates the Fourier transform of the particle's displacement, $\tilde{x}(f)$, to the Fourier transform of the force applied to the particle, $\tilde{F}(f)$:

$$\tilde{x}(f) = A^*(f) \cdot \tilde{F}(f), \quad (2.8)$$

where $A^* = A'(f) + iA''(f)$.

When the system is in thermal equilibrium and there is no external force present, the fluctuation-dissipation theorem relates the magnitude of the fluctuating force to the dissipation of energy [117]. In one of the most general formulations of the fluctuation-dissipation theorem, the power spectrum of a particle's displacement (fluctuations) is related to the imaginary part of the complex response function (dissipation through thermal energy, $k_B T$) as follows:

$$A''(f) = \frac{\pi f}{2k_B T} \cdot P(f), \quad (2.9)$$

Figure 2.10 shows the imaginary part of the complex response function for water (red crosses).

The Kramers-Kronig relation can then be used to obtain the real part of the complex response function:

$$A'(f) = \frac{2}{\pi} \int_0^{\infty} \frac{\xi A''(\xi)}{\xi^2 - f^2} d\xi. \quad (2.10)$$

Figure 2.10 also shows the results obtained for this real part of the complex response function for water (blue circles). Note the very sharp drop in $A'(f)$ at $f > 3$ kHz. This is due to the finite high-frequency cut-off of the integration in Eq. 2.10. As will be shown, this leads to significant distortion in the real part of the complex shear modulus (elastic modulus) at $f > 3$ kHz.

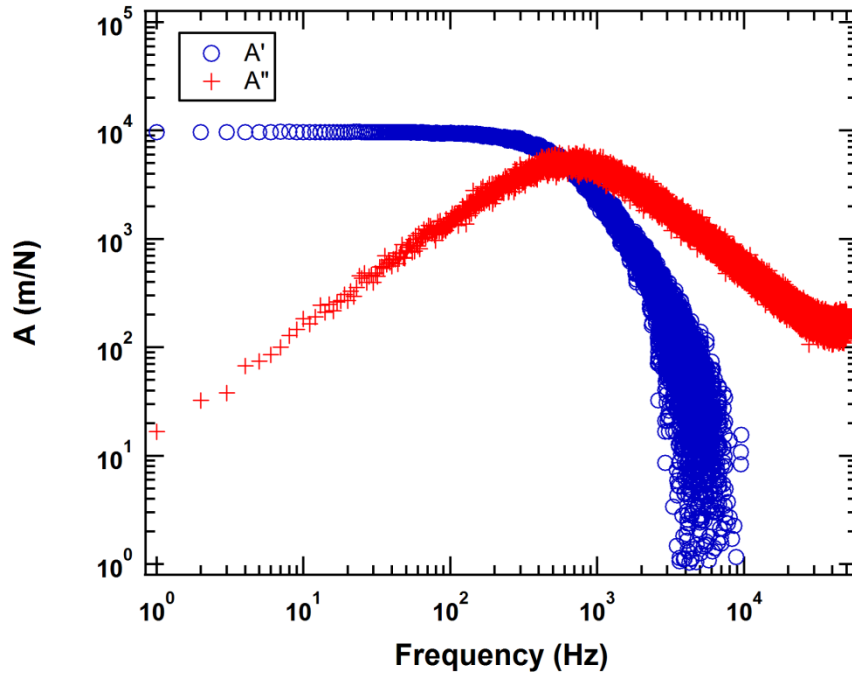


Figure 2.10. Real (blue circles) and imaginary (red crosses) parts of the complex response function for a 2.1 μm bead trapped in water.

Complex shear modulus: As the final step, viscoelastic properties of the medium in the form of the complex shear modulus can be determined from the complex response function using the generalized Stokes-Einstein relation [73,113]:

$$G^*(f) = \frac{1}{6\pi A^*(f)R}, \quad (2.11)$$

in which R is the radius of the probe particle. By definition, G'' is negative [113,118,119] (since A'' is positive), but following convention, throughout this thesis, the magnitude of the viscous modulus is presented. Figure 2.11(A) shows the results obtained for the elastic and viscous moduli as a function of frequency for water.

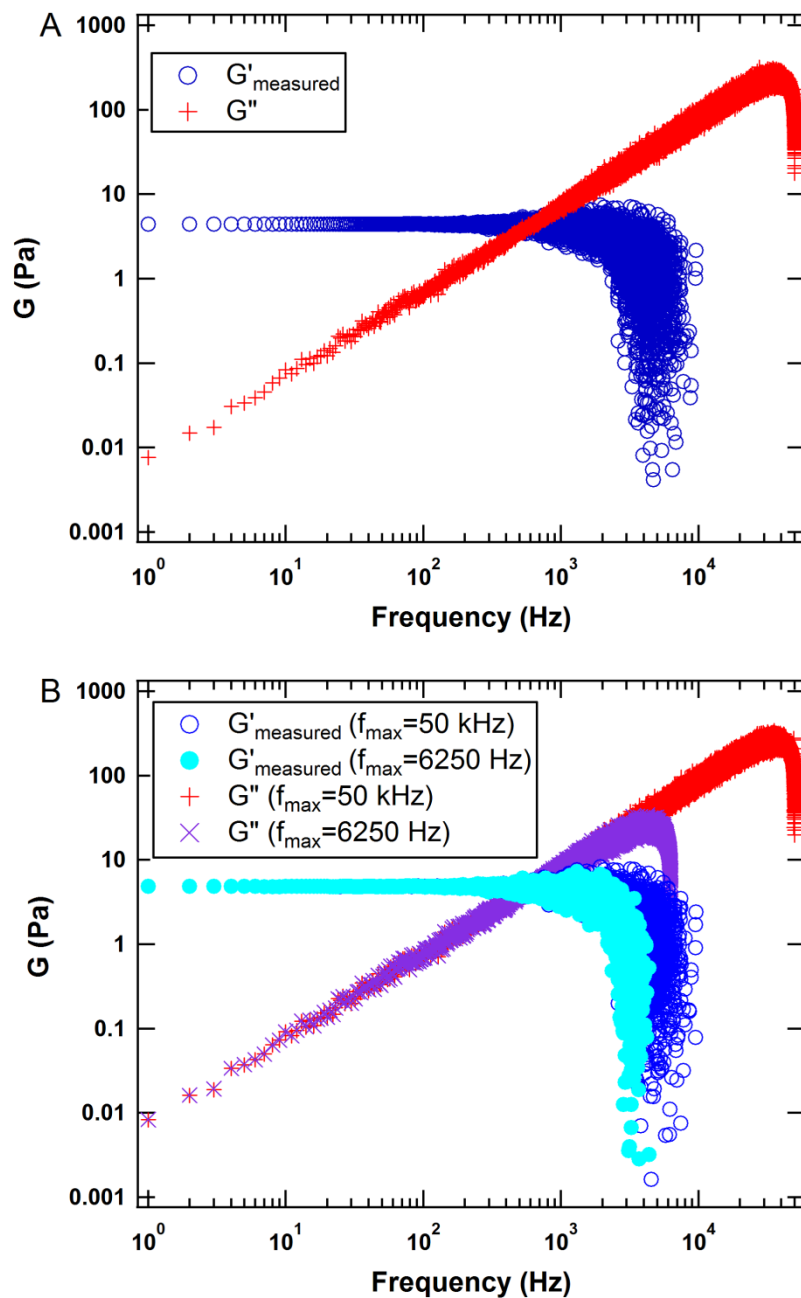


Figure 2.11. (A) Real (blue circles) and imaginary (red crosses) parts of the complex shear modulus measured for a 2.1 μm bead trapped in water. (B) Comparison of the obtained shear moduli from the original data ($f_{\text{max}}=50$ kHz) and as if the data were sampled at $1/8^{\text{th}}$ of the original bandwidth ($f_{\text{max}}=6250$ Hz). Each plot shows an average of 100 sets of 1-second measurements.

As described for Eq. 2.10, the significant distortion in both the real and imaginary parts of the complex shear modulus is due to the frequency cut-off of the integration in that equation. In order to verify this, the original displacement data were manipulated as

if the experiment were made with a bandwidth equal to $1/8^{\text{th}}$ of the original one (simply by using every eighth point of the original $x(t)$ data). This changes the maximum frequency (f_{max}) from 50 kHz to 6250 Hz. Figure 2.11(B) shows that the distortion starts at smaller frequency for the manipulated data compared to the original one. This demonstrates that the distortion is predominantly due to the finite sampling rate.

Correction for the effect of the trap: A purely viscous medium such as water has no elastic modulus, however, as seen in Figure 2.11, calculated elastic modulus values are not insignificant, and were found to vary with the laser power (Figure 2.12). This results from the confinement of the beads because of the laser trap [113]. That is, $G'_{measured} = G'_{medium} + G'_{trap}$. In Appendix B, I show mathematically that the viscous modulus is not influenced by this effect, and that the trap's effect on the elastic modulus can be corrected using the following equation:

$$G'_{medium} = G'_{measured} - \frac{\kappa}{6\pi R}, \quad (2.12)$$

in which κ is the trap stiffness and R is the bead radius [113].

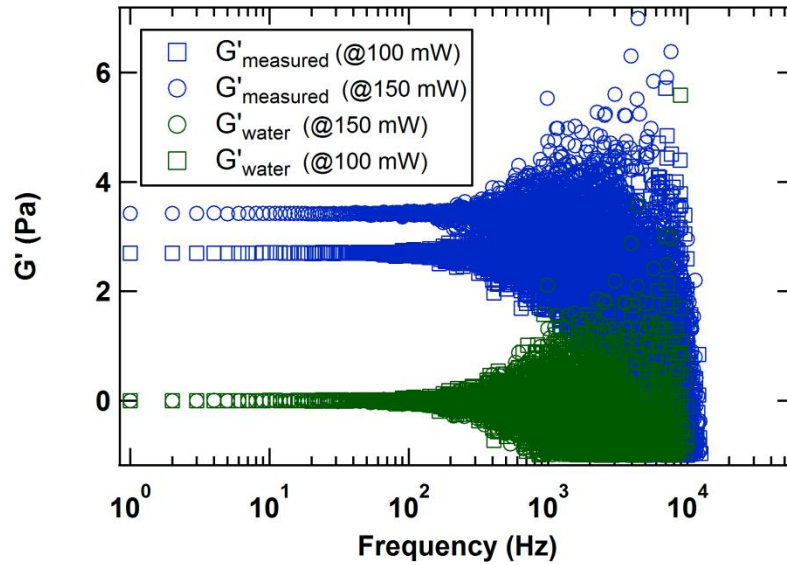


Figure 2.12. The measured elastic modulus of water (blue circles/squares) scales with laser power. By correcting for trap modulus via subtraction of the low-frequency G' values (see text), the curves collapse to zero (green circles/squares). This plot is shown in semi-log scale. The large dispersion at high frequencies ($f > 200$ Hz) is predominantly due to the finite sampling. This issue is discussed more in Appendix C.

Three different methods can be used to correct measured data for the elasticity of the trap. The first applies to a purely viscous (Newtonian) fluid. Here, bead radius can be found from Eq. 2.5 and trap stiffness from Eq. 2.6. Thus, first $G'_{measured}$ can be correctly determined for each bead, using Eq. 2.11. Then, R and κ can be used in Eq. 2.12 to correct the measured modulus for the trap. An example of this type of analysis is shown in Figure 2.13 for two different beads, which were found to be of different size (~25% difference in radius).

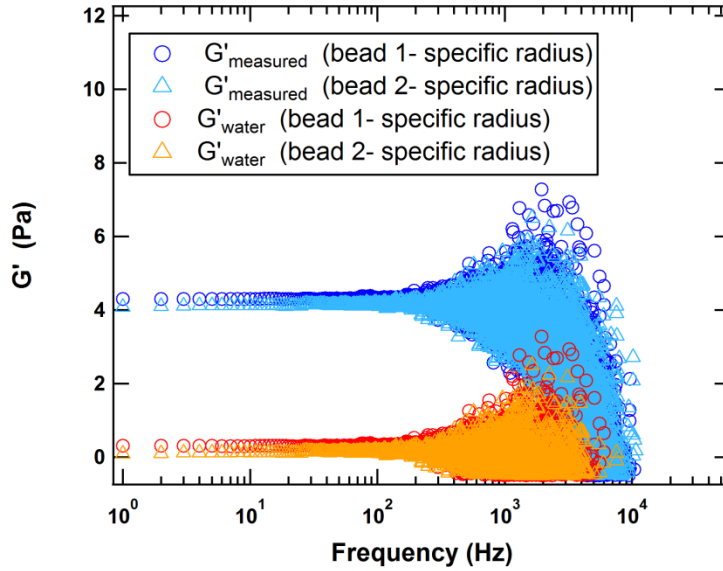


Figure 2.13. Two examples of the $G'_{measured}$ values obtained for two different beads in water for a laser power of 150 mW. The actual sizes of the beads were determined by Eq. 2.5 and elasticity for the trap was corrected using Eq. 2.12. This plot is shown in semi-log scale to facilitate reading the data.

Although this first method works well for the trap correction of a viscous medium, it is not applicable for viscoelastic media. This is because it is not possible to use Eq. 2.5 to extract the actual bead size; instead, for a viscoelastic medium, this second correction method uses the average bead size to determine $G'_{measured}$ (Eq. 2.11). Then, in order to correct for elasticity of the trap, this method uses the average elastic modulus of the trap determined for the beads in water ($N=28$): $G'_{trap} = 3.9 \pm 0.7 Pa$ at the laser power of 150 mW. Applying this method, I found that small differences in bead radius cause large error in the resultant G'_{medium} . For example, Figure 2.14 shows the $G'_{measured}$ results obtained for two different beads with the same laser power (150 mW), using the average bead size in the calculations. When the average elastic modulus of the trap, $G'_{trap} = 3.9 \pm 0.7 Pa$, is used, the measurement with higher $G'_{measured}$ will have non-trivial elasticity ($>1 Pa$) while the one with lower $G'_{measured}$ won't have any (actually, non-physical negative values). Therefore, this second method has less reliability, especially when $G'_{measured}$ is close to G'_{trap} .

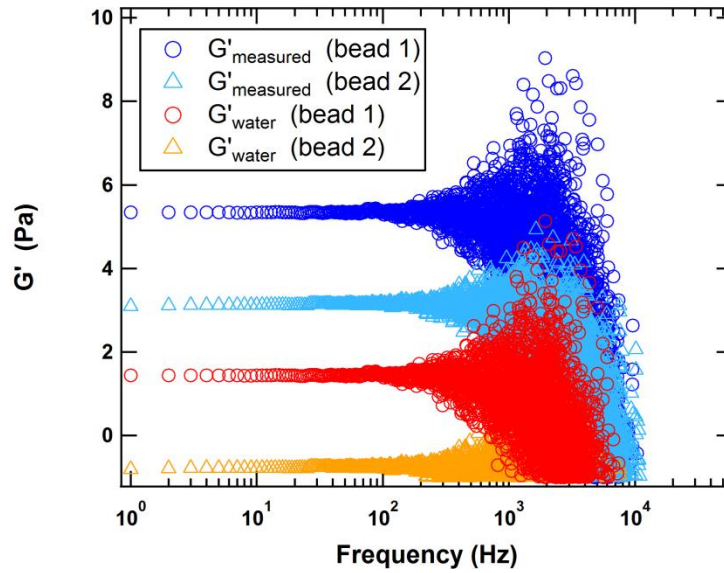


Figure 2.14. Similar data as in Figure 2.13 when an average bead size is used instead of the actual size (Eq. 2.5). A small variation in bead size causes a large error in G'_{medium} , if Eq. 2.12 is used for correction of the trap.

To overcome this issue, Addas *et al.* [113] suggested an alternative method which requires knowing the exact value of neither the trap stiffness nor the particle radius. For solutions which do not have elasticity at low frequencies, $G'_{measured}$ at low frequency is due only to the trap. Based on this, they suggest using the average value of the first few data points of $G'_{measured}$ as G'_{trap} and subtracting this value from the values of elastic moduli at all other frequencies. Figure 2.15 shows the elastic modulus measured for water before and after correction for the trap for the two different beads at the same laser power. Figure 2.12 also shows the results after correction for the trap when different laser powers are used. The variation in $G'_{measured}$ obtained for two different beads (or laser powers) is eliminated after correction for the trap by subtracting the mean value of $G'_{measured}$ at $f < 10 \text{ Hz}$. This method is recommended for viscoelastic examples with no elasticity at low frequency.

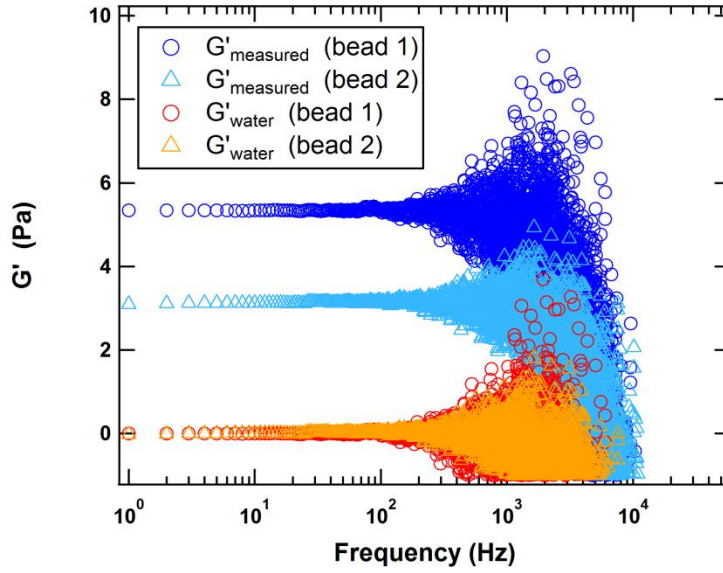


Figure 2.15. Dark and light blue symbols are similar data as in Figures 2.13 and 2.14 when an averaged bead size is used instead of the actual size (Eq. 2.5). When the average value of the first few data points of $G'_{measured}$ is used as G'_{trap} , G'_{water} become similar and equal to zero for both measurements.

In viscoelastic media, depending on the polymer concentration, a plateau at low frequency, representing G'_{trap} only, may not be observed. In such a case, a modification of the above approach has been used in order to extract G'_{medium} from the measured values. The correction method used for each studied medium in the following chapters (Chapter 5 for solutions of collagen molecules and Chapter 6 for collagen gels) will be mentioned.

Finally, in order to obtain shear moduli equally spread in frequency on a log scale, the data are logarithmically binned into N bins such that the width of each bin is:

$$\log(f_{i+1}) - \log(f_i) = \log(a) \quad (2.13)$$

where a is a constant equal to $f_{max}^{1/N}$. Selecting $N = 22$, for our experiments where $f_{max} = 50$ kHz, $a = 1.63$.

After logarithmically binning the data for each bead, the final results are averaged among different beads. Figure 2.16 shows an example of the results for the averaged

values of both moduli obtained for ten different beads in water. The values for elastic modulus are statistically close to zero (as expected for water). The viscous modulus is analysed in the following section.

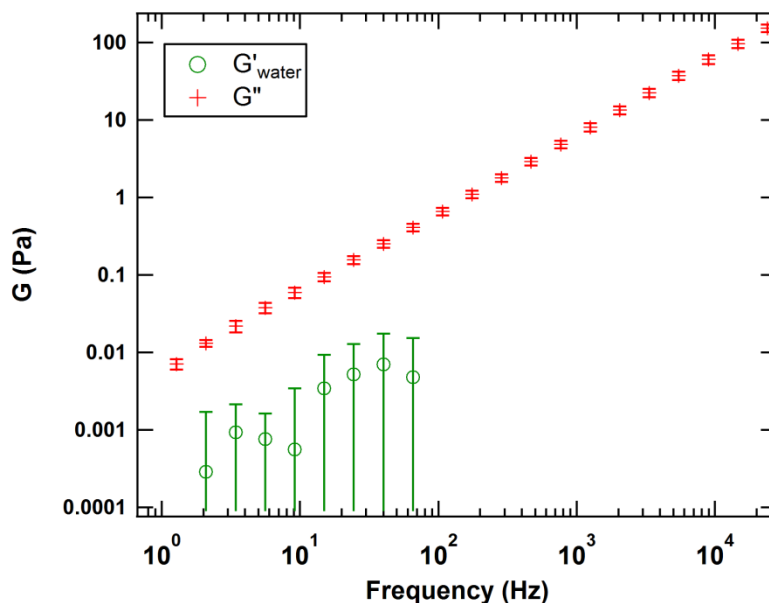


Figure 2.16. Elastic (green circles) and viscous (red crosses) moduli of water are presented in logarithmically equally spaced format and averaged over ten different beads. Error bars show the standard deviation among these ten measurements.

2.5. Verification of the Microrheological Characterization Technique

In order to validate the values of shear moduli (viscous and elastic moduli) obtained from my optical tweezers microrheology measurements, two model systems were examined. First, water was tested as a purely viscous medium, and viscosity was extracted from the microrheology measurements and compared to the expected value. Second, a simple uncrosslinked polymer solution, polyethylene oxide (PEO), was also tested as a viscoelastic medium, and the viscoelastic properties obtained from my microrheology measurements were compared to the ones in the literature [120]. The following sections include experimental details for these measurements followed by the results and discussions for each of the experiments.

2.5.1. *Experimental Details*

For the purpose of microrheology experiments, a solution of polystyrene microspheres (2.1 μm in diameter) in water was prepared as explained in Section 2.3. The preparation of the PEO solution followed that of Dasgupta *et al* [120], who studied bulk and microrheology properties. A 6.7 wt% solution was prepared by mixing 200 kDa PEO powder (Sigma Aldrich) with distilled water. This concentration is much higher than the overlap concentration (0.48 wt% [120]) for 200 kDa PEO solution. This ensures that the solution exhibits significant viscoelasticity because of the overlap and entanglements between neighboring molecules. To allow the polymer to dissolve thoroughly and homogenize, it was gently mixed at 40°C for 10 days. Sodium chloride was added to a final concentration of 25 mM to ensure an identical salt concentration compared to Ref. [120].

2.5.2. *Microrheology of water*

I showed in Figure 2.16 that, after correction for the effect of the trap, values for the elastic modulus of water are statistically equivalent to zero. Another verification method for characterizing a viscous medium (water) is to extract viscosity from the viscous modulus. The equation below shows the relation between viscous modulus and dynamic viscosity, η [41]:

$$G''(f) = 2\pi\eta f, \quad (2.14)$$

where f is frequency. In a purely viscous fluid, η is frequency-independent and hence, when viscous modulus is plotted versus frequency on a logarithmic scale, a straight line with the slope of 1 and y-axis intercept of $\log(2\pi\eta)$ should describe the data.

Figure 2.17 shows the viscous modulus obtained for water (averaged among ten beads, replotted from Figure 2.16) and its corresponding fit (Eq. 2.14). The value obtained for viscosity ($(1.01 \pm 0.03) \times 10^{-3}$ Pa.s) agrees well with the expected value for the viscosity of water at 21°C (1.002×10^{-3} Pa.s).

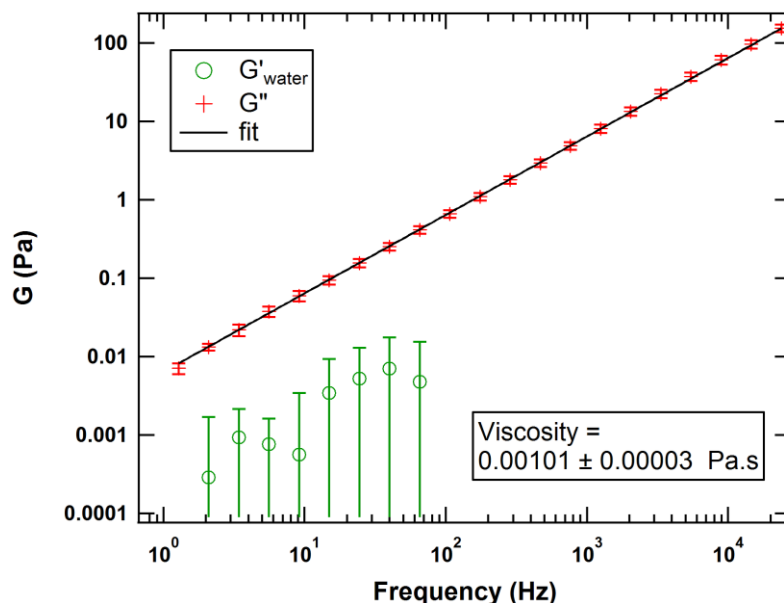


Figure 2.17. Elastic (green circles) and viscous (red crosses) moduli of water (replotted from Figure 2.16). The black line shows the corresponding fit (Eq. 2.14) to the values of viscous modulus. The fitting parameter (viscosity) obtained is 1.01×10^{-3} Pa.s.

2.5.3. Microrheology of PEO

In order to confirm the correct implementation of our optical-tweezers-based microrheology measurements and analysis for a viscoelastic system, the response of a flexible polymer solution, PEO, was characterized. This choice allowed me to compare the microrheological results with that from the bulk rheology, and with another microrheology technique, diffusing-wave spectroscopy (DWS) [120]. The graphs in Figure 2.18 compare elastic and viscous moduli of PEO obtained from our optical tweezers (OT) technique (crosses) with those obtained in [120] via bulk measurements (open squares/circles) and DWS measurements (solid lines). For these data, the third correction method ($G'_{measured}$ at the lowest frequency) was used to subtract the elasticity of the trap from the measured elastic modulus.

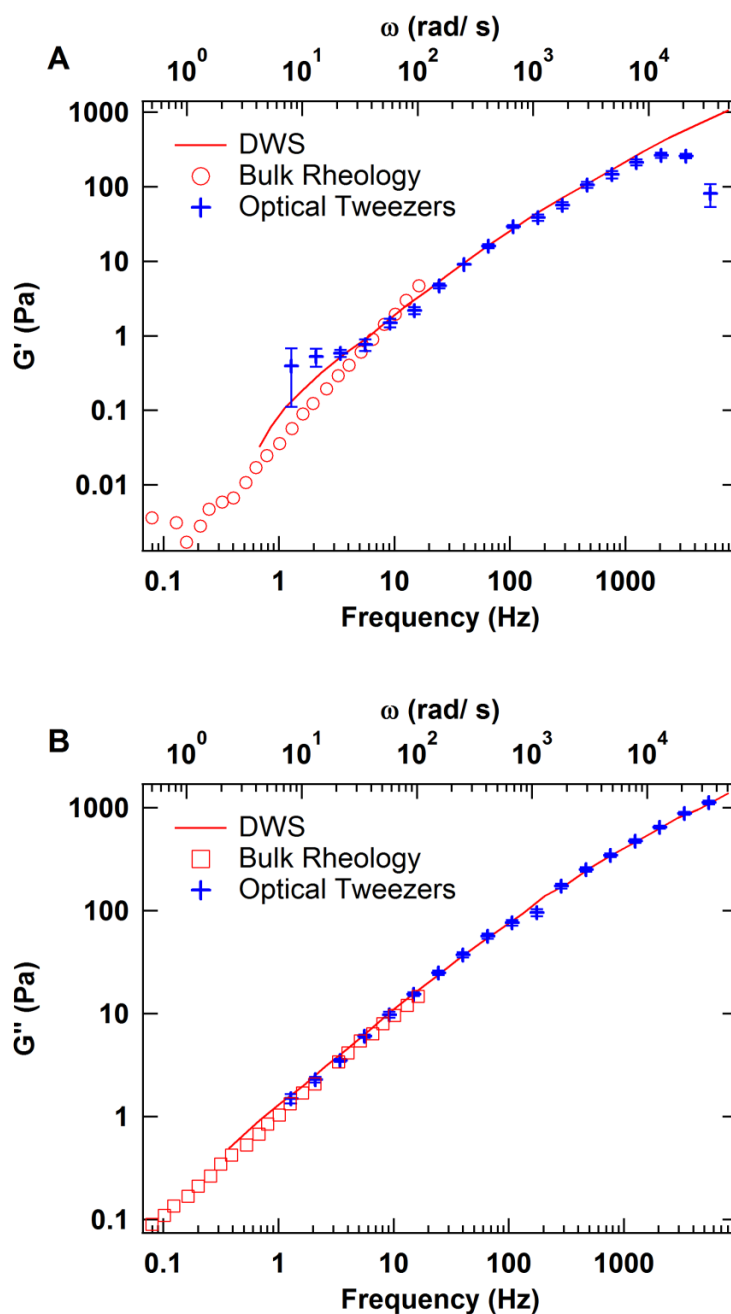


Figure 2.18. (A) Elastic and (B) viscous moduli of 6.7 wt% PEO obtained using our optical tweezers technique (crosses), compared with bulk rheology (open symbols) and microrheology via diffusing-wave spectroscopy (DWS; solid line) from reference [120]. Crosses indicate the mean values over 5 independent measurements, and error bars represent the standard error of the mean.

It is clear that our extracted values of G'' show excellent agreement over our entire measured frequency range, as do values for G' for most of the frequency range.

At higher frequencies, the extracted values of G' underestimate the true G' , a well-known problem in microrheology that stems here from the finite bandwidth of our measurements compared with the infinite integration range in the Kramers-Kronig relation (Eq. 2.10 and Figure 2.11) [113].

In this last section, I have shown that the optical-tweezers-based microrheology technique and analyses methods of this work give the expected results for both a viscous fluid and a viscoelastic solution.

Chapter 3.

Collagen and its characterization

In this chapter, I first present an introduction to the structure of collagen at the molecular and self-assembled levels. Then, several methods of characterization of single molecules and fibrillar collagen systems are explained. These methods include gel electrophoresis to determine the presence and purity of collagen, ELISA to quantitatively determine collagen concentration, turbidity measurements to monitor kinetics of self-assembly, and electron microscopy to verify the formation of fibrils.

3.1. Collagen structure and self-assembly

The collagen superfamily in vertebrates includes more than 50 types of collagen (more than 25 different collagens in humans), for example defined as types I, II, III, V (Table 1.1), which vary in amino acid sequence of their chains [22]. One of the most abundant types of collagen is collagen type I, which falls in the sub-family of fibrillar collagens and is the focus of this thesis work.

A triple-helical molecule of type I collagen with a molecular mass of approximately 300 kDa consists of two identical α chains (α_1) and one α chain with slightly different composition (α_2) [22]. Table 3.1 shows the amino acid composition of the two types of chains. Together the three chains of collagen form a triple-helical structure including short non-helical regions at both ends (-NH₂ and -COOH terminal domains). These non-helical regions, also called telopeptides, can be digested by the enzyme pepsin, the process of which is discussed in Chapter 5.

Table 3.1. Amino acid composition of the chains (including telopeptides) in triple-helical collagen type I from rat tail tendon. (This information is sourced from the Universal Protein Resource, UniProt, for genes COL1A1 and COL1A2).

Amino Acid	α_1	α_2
Ala (A)	115	104
Arg (R)	53	53
Asn (N)	14	22
Asp (D)	34	21
Cys (C)	0	0
Gln (Q)	31	24
Glu (E)	49	45
Gly (G)	346	344
His (H)	2	9
Ile (I)	7	21
Leu (L)	20	35
Lys (K)	38	32
Met (M)	8	5
Phe (F)	14	10
Pro (P)	236	201
Ser (S)	44	42
Thr (T)	20	20
Trp (W)	0	0
Tyr (Y)	5	2
Val (V)	20	33
Total number of amino acids	1056	1023

A type I collagen molecule (as well as other fibrillar collagens) is known to be about 300 nm in length and 1.5 nm in diameter [121,122]. It is worth mentioning that telopeptides comprise less than 5% of the total length of the molecule (only 43 and 11 amino acids in α_1 and α_2 chains, respectively). However, it is known that they play a key role in the self-assembly process [22,123]. In the extracellular matrix, individual collagen molecules (fibrillar types) assemble hierarchically into fibrils with highly ordered structures of tens of micrometers in length and 30-300 nm in diameter [124]. Successively, collagen fibrils can assemble into fibres or networks. *In vivo*, depending on the tissue, these may contain other proteins as in skin or minerals as in bone [22,125]. *In*

vitro, the process of self-assembly to form fibrils can be replicated in appropriate chemical environment (e.g. neutral pH and appropriate salt concentration) [126].

The hierarchical pathway of collagen assembly is shown in Figure 3.1. The initial step is suggested to be the lateral association of five triple-helix molecules to form microfibril units which then longitudinally and laterally associate with other microfibrils and form fibrils [127–129]. At neutral pH and body temperature, this process is spontaneous and entropically driven, which is favored by hydrophobic interactions. In other words, the loss of hydrating water around the hydrophobic residues of collagen is entropically favorable [130,131]. Other than hydrophobic interactions, which are known to have a predominant role in self-assembly of collagen, electrostatic and van der Waals interactions [132] and hydrogen bonding [133] also contribute to the process. Therefore, depending on the chemistry of the molecule as well as its environment, different fibrillar morphologies can be achieved [124,132].

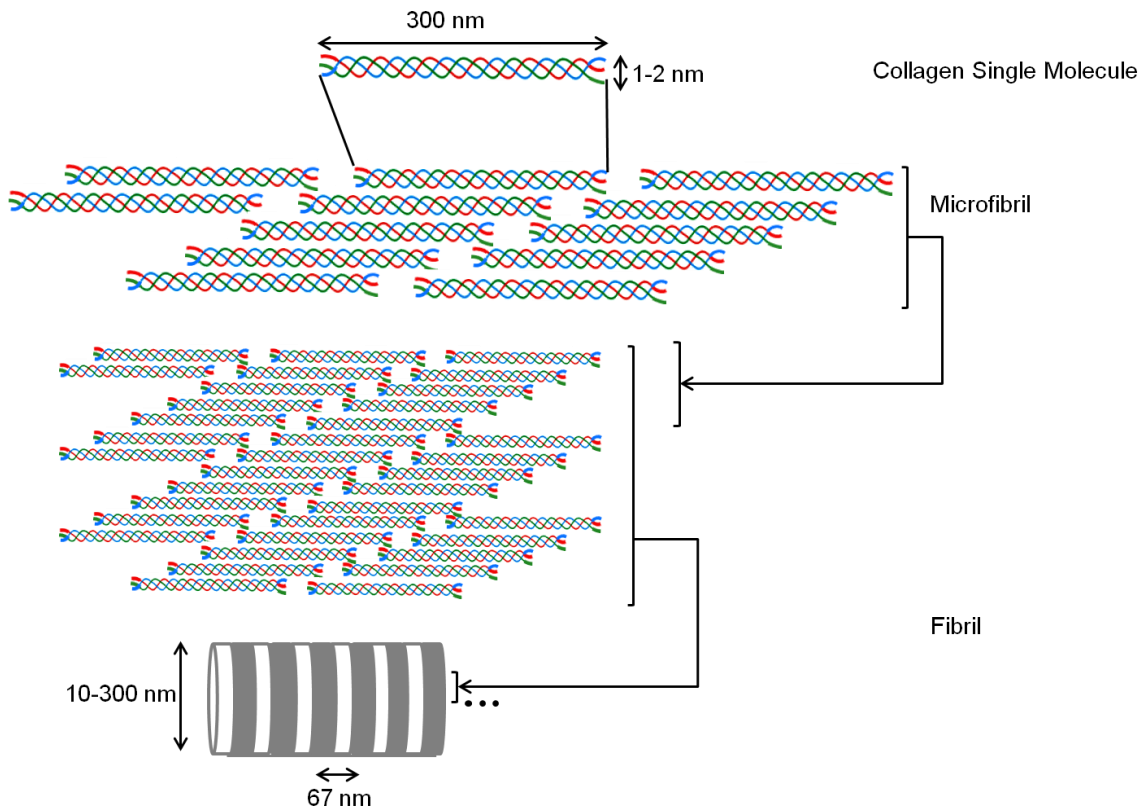


Figure 3.1. Hierarchical self-organization pathway of fibrillar collagen. Triple-helical molecules of collagen associate laterally to form fibrils with characteristic 67 nm D-banding patterns.

An alternating dark/light (gap/overlap) pattern is a well-known characteristic of collagen fibrils that have been appropriately stained for electron microscopy imaging. This is called “D-periodic spacing” or “D-spacing” or “D-banding” [22]. For hydrated tendon, the reported D-spacing is ~67 nm [134]. However, environmental parameters such as pH, presence of salt and its concentration affect the *in vitro* morphology. For instance, when fibrils are made at pH=8 versus 7.3, the average D-spacing is measured to be 62 and 64 nm, respectively [135]. Salt can affect the D-banding substantially. The D-periodicity has been found to be 49 nm when fibrils are formed in the presence of Na_2SO_4 versus 59 nm in the presence of Na_2HPO_4 [135]. Table 3.2 summarizes this information.

Table 3.2. D-spacing values of type I collagen fibrils: formed *in-vivo* or *in-vitro* with different solvent conditions.

Collagen fibril obtained <i>in vivo</i> or <i>in vitro</i>	pH / salt	D-spacing (nm)	Reference
<i>In vivo</i> (Tendon)	-	67	[134]
<i>In vitro</i>	8.0 / Na ₃ PO ₄ , NaCl	62	[135]
<i>In vitro</i>	7.3 / Na ₃ PO ₄ , NaCl	64	[135]
<i>In vitro</i>	7.4 / Na ₂ SO ₄	49	[135]
<i>In vitro</i>	7.4 / Na ₂ HPO ₄	59	[135]

In order to be able to correlate rheological observations to molecular interactions of collagen, it is important to first characterize the chemical and physical properties of the system. Therefore in the rest of this chapter, the techniques that are used to characterize collagen systems are described.

3.2. Materials

Collagen I from rat tail tendon was purchased from Cultrex Invitrogen as a stock solution of collagen in 20 mM acetic acid with collagen concentration of 5 mg/ml. In this acidic condition (pH=3.3), collagen does not form fibrils. The company provided us with two different types of collagen samples depending on their purification procedures: pepsin-treated (without telopeptides) and acid-solubilized (including telopeptides). Concentrations below 5 mg/ml were prepared by dilutions in 20 mM acetic acid.

3.3. Sodium Dodecyl Sulfate Polyacrylamide Gel Electrophoresis (SDS-PAGE)

The most commonly used biochemical assay to investigate protein purity and size is SDS-PAGE [21,136]. The technique is based on separating protein constituents by their electrostatic mobilities followed by qualitatively visualizing the fraction of each constituent. For the protein collagen, the first step was denaturing collagen to its polypeptide chains (2 chains of α_1 and 1 chain of α_2) in the specific loading buffer: 3.9 ml deionized water, 1 ml 0.5 M Tris-HCl (pH 6.8), 0.8 ml 100% Glycerol, 1.6 ml 10% SDS

(sodium dodecyl sulfate), 0.4 ml 2-mercaptoethanol, 0.4 ml 1% bromophenol blue. This was done by incubating each sample including SDS at 80°C for 10 minutes. After loading denatured protein into the wells of the previously prepared 6% polyacrylamide gel, application of an electric field allows for migration of protein fragments towards the anode. This is because the polypeptides are coated with SDS, which is negatively charged. Although less charged, because of their ability to more easily thread through the pores of the gel, smaller proteins migrate faster than larger proteins. This allows for the separation of proteins based on their molecular weights. The voltage used for this work was 200 V in a standard gel tank. In order to see bands for collagen with proper separation, this voltage was applied for 50 minutes. The final step is staining the gel with dye, Coomassie blue, to visualize the protein bands.

Figure 3.2 shows the presence and purity of the collagen samples used in this work. The two existing bands close to 120 kDa corresponds to α_1 and α_2 chains, as introduced in Table 3.1. The α_1 chain has slightly higher molecular weight than α_2 and appears darker because there are twice as many α_1 as α_2 chains. The fainter bands at molecular weights above 200 kDa are called β bands and correspond to two crosslinked α chains, either α_1 and α_2 chains together (lower band) or two α_1 chains (upper band). The γ band, which is barely seen in Figure 3.2 at the top of the gel, corresponds to a crosslinked trimer $(\alpha_1)_2\alpha_2$.

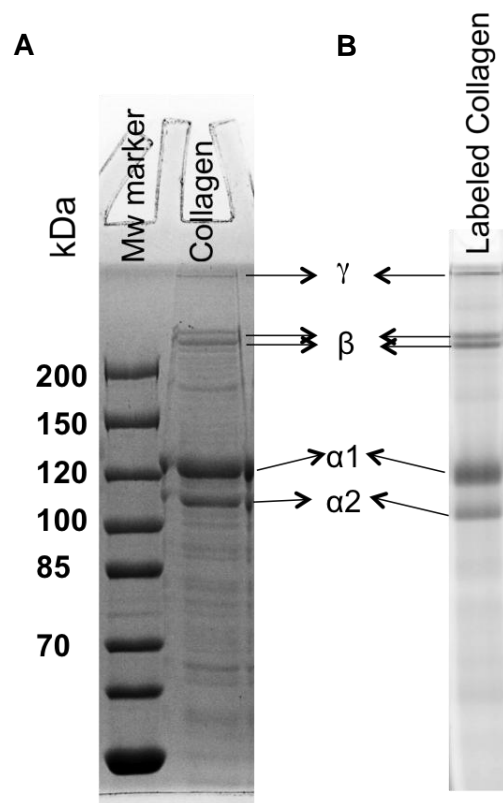


Figure 3.2. SDS-gel electrophoresis reveals the presence (sharp bands corresponding to the α_1 and α_2 chains) and purity of the collagen stock solution using a gel stained with Coomassie blue dye in (A), and visualizing a fluorescently labelled collagen in a separate gel (B).

Coomassie blue dye preferentially binds to aromatic amino acids: phenylalanine (F), tryptophan (W), histidine (H), tyrosine (Y) and basic amino acids (mainly Arginine (R)) [137]. According to Table 3.1 collagen has only a few aromatic amino acid groups, therefore, staining of collagen molecules does not lead to a strong signal (in comparison to other proteins). In order to compensate for this problem, in a separate experiment collagen molecules were labelled with a fluorescent dye (Alexa Fluor® Succinimidyl Ester, Invitrogen). The dye selectively binds to primary amine (R-NH₂) groups such as in lysine (K) side chains. Appendix D explains the protocol used for labelling the collagen with the Alexa fluorophore. After collagen was labelled, the same protocol for separating proteins using gel electrophoresis was used. Then, the Typhoon scanner (Typhoon 9410 Gel and

Blot Imager) was used to visualize the bands within the gel. Figure 3.2(B) verifies the purity of the collagen stock solution.

3.4. Enzyme-Linked Immunosorbent Assay (ELISA)

ELISA is an analytic biochemistry assay that is based on the detection of a substrate in a liquid sample or on a wet surface by using an antibody. It is so sensitive that it can be used for quantitative determination of the substrate concentration. In this thesis, I used this technique to determine collagen concentration for the original samples or the treated ones, e.g. after sonication (Chapters 4 and 5). The protocol is explained in Appendix E.

3.5. Turbidity Measurements of Fibril Formation Kinetics

Turbidity has been used widely to measure the rate of collagen fibril formation [39,124,132,138–140]. Turbidity profiles are acquired by monitoring the optical density as a function of time, because it has been shown that optical density is proportional to the amount of the product capable of precipitation (*i.e.* collagen in fibrillar form) [39]. Here, in order to investigate the kinetics of fibril formation and the effect of parameters such as temperature, concentration, and the presence of telopeptides, turbidity measurements were performed. In general, fibril formation was induced by adding 10X PBS (phosphate buffered saline) with excess phosphates (this buffer is defined as “fibril formation buffer”) to the collagen solution to attain a final concentration of 0.5 or 1 mg/ml collagen, with the final salt concentrations of 273 mM NaCl, 5 mM KCl, 42 mM Na₂HPO₄ and 9 mM KH₂PO₄ (final pH=6.9). Samples were prepared on ice to avoid fibril formation before readings had been started.

The kinetics of collagen self-assembly were monitored at 20°C and 30°C, by recording the increase in optical density at 347 nm as a function of time while fibrils form. For the 30°C experiments, a microplate fluorescence reader (Bio-Tek FL600) was used, which allows for monitoring several wells (replicates of the sample of interest) in one single run. For the 20°C experiment, however, due to the instability of the plate-reader’s

temperature control near room temperature, turbidity measurements were done in a spectrometer (1700 UV-Vis Spectrometer, Shimadzu). In the spectrometer, a quartz cuvette was used and turbidity measurements were repeated on three identically prepared samples. In all turbidity experiments, 100 μL of collagen sample were probed either in each well or in the cuvette.

Figure 3.3 compares the results for two different concentrations of collagen undergoing self-assembly into fibrils at 30°C. A typical sigmoidal curve [39,131,138] is seen. The increase in optical density is due to the fact that the larger collagen fibrils scatter much more than the smaller molecules of collagen (which contribute no optical density at this wavelength). It has been shown that collagen assembly into fibrils follows first-order kinetics with respect to collagen concentration [141]. There exist three distinct regions in these sigmoidal curves: lag phase, growth phase and plateau phase.

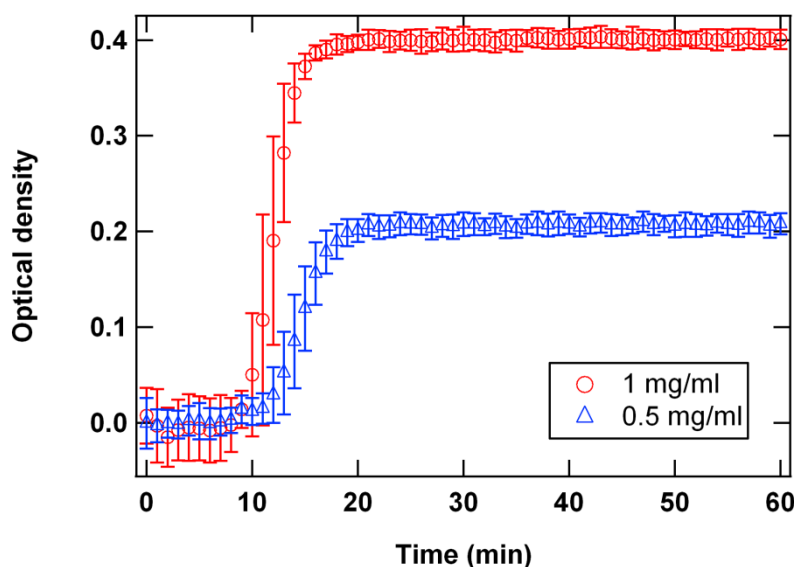


Figure 3.3. Turbidity measurements of collagen fibril formation kinetics at 30°C as a function of collagen concentration: 0.5 and 1 mg/ml. Here, collagen has its telopeptides intact. Error bars represent standard deviations from 5 replicate measurements.

The lag phase occurs before the onset of the increase in optical density, and is associated with fibril nucleation. This phase is known to be affected the most by the removal of telopeptides [142] which has been verified in Figure 3.4. This figure also suggests that the growth kinetics are affected.

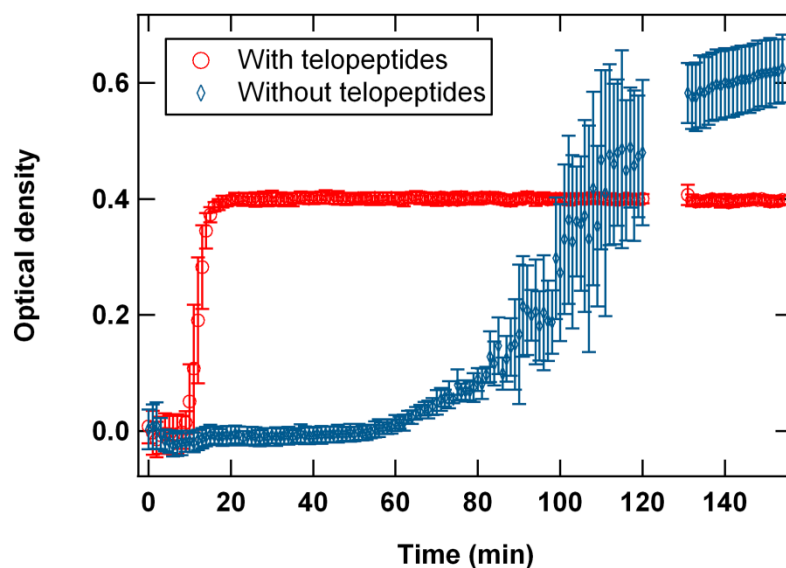


Figure 3.4. The effect of telopeptide removal on the kinetics of collagen fibril formation at 30°C and 1 mg/ml concentration. The gap between 120 and 130 minutes is because the experiment was stopped and re-run. Error bars represent standard deviations from 5 replicate measurements. The larger error bars obtained for the telopeptide-removed collagen versus collagen including telopeptides are due to their morphological difference: the former was a solution including white patches whereas the latter was a milky and macroscopically more homogenous solution.

The growth phase is defined as the period during which fibrils increase in size (assembly of microfibrils to fibrils) [39,124,138–140]. Finally, there exists a plateau phase at which the optical density of the sample reaches its maximum value and does not vary over time [39,124,138–140]. It has been shown that all of these three regions are dependent on environmental conditions such as temperature (also studied here), pH, presence of salt, and molecular modifications [39,124,132,140]. Figure 3.5 compares the kinetics of fibril formation for 0.5 mg/ml collagen at 20°C and 30°C measured in the spectrometer and plate reader instruments, respectively. In order to compare the results from the two measurements, optical densities were normalized by the maximum value obtained in each measurement. The difference between kinetics of fibril formation at 20°C and 30°C (especially during the growth phase) corresponds to the fact that the process is entropically driven and hence, temperature-dependent. Furthermore, Figure 3.5 shows that at 20°C, the fibril formation process does not reach completion before ~ 50 min, while at 30°C, it reaches the plateau phase after ~20 min. In order to monitor microrheological properties during fibril formation (Chapter 6), room temperature

conditions were selected. This is because there is enough time to monitor the properties in the growth phase.

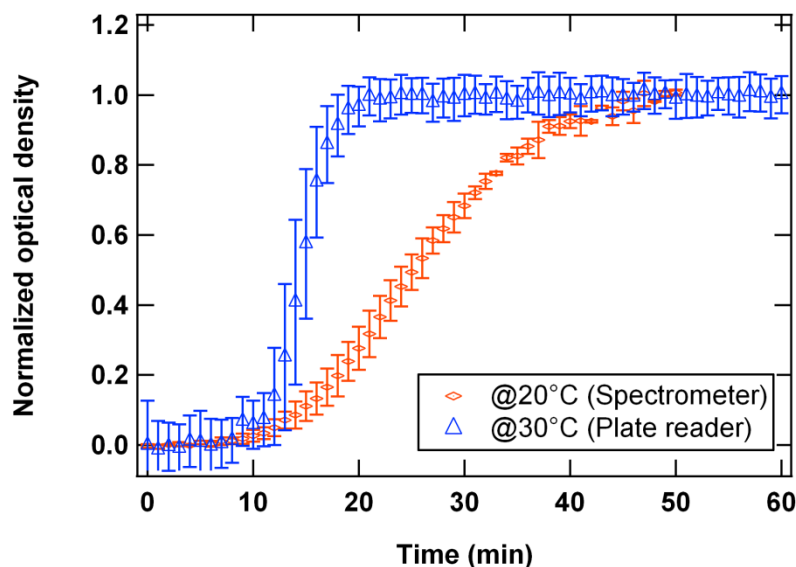


Figure 3.5. Turbidity measurements of collagen fibril formation at a collagen concentration of 0.5 mg/ml at 20°C and 30°C. Collagen has intact telopeptides.

3.6. TEM study of collagen fibrils

Transmission electron microscopy (TEM) is known to be a technique well-suited to studying the morphology of collagen fibrils. From TEM images, the lengths, diameters, and perhaps more interestingly D-spacing can be determined [132,140]. In this work, in order to verify the formation of well ordered collagen fibrils, they were imaged via TEM.

In order to create contrast between a collagen fibril and the background, staining with heavy metal is usually used. Because of the high electron density of the heavy metal, more stained regions appear as dark regions and less stained regions appear brighter. For a collagen fibril with a gap/overlap pattern, stain molecules preferentially penetrate into the lowest collagen packing regions (gaps) rather than the overlap regions (Figure 3.1). Therefore following staining, a collagen fibril with a D-periodic banding pattern should exhibit a dark/bright pattern corresponding to the gap/overlap regions.

Details of the sample preparation are as follows. Collagen fibrils were formed by adding fibril formation buffer (as described in the previous section) and incubating

overnight at room temperature. Formvar carbon-coated copper grids (200 mesh, Ted Pella) were used on which the fibrils were adsorbed. The grids were floated with the coated side facing down on 20 μl drops of collagen fibril suspension on a piece of Parafilm. The specimens were allowed to adsorb to the grid for 1 hour. Then the grids were washed three times by floating them on 50 μl drops of deionized water for 2-3 minutes. Finally, grids were floated with the sample side facing down on 20 μl drops of 2% uranyl acetate for 45 seconds. Excess stain was removed by filter paper and the grid was allowed to air dry at room temperature for ~ 1 min. Images were collected on a Hitachi 8100 TEM at an accelerating voltage of 200 keV.

Figure 3.6(A) shows an example of the fibrils formed at 20°C and Figure 3.6(B) correlates the arrangement of the triple helical collagen molecules in a gap/overlap pattern to the dark/bright pattern observed in the TEM image. The average D-spacing obtained from this image is 73 ± 2 nm. The slight difference between D-spacing obtained here and fibrils formed *in vivo* (67 nm) could be due to the uncertainty of image calibration or the different temperature and chemical environment in which fibrils are formed. In any case, the presence of D-banding pattern is an indicator of well ordered collagen fibrils under the conditions used here. With this verification, it is possible to investigate and interpret the microrheological properties of collagen fibril systems (Chapter 7).

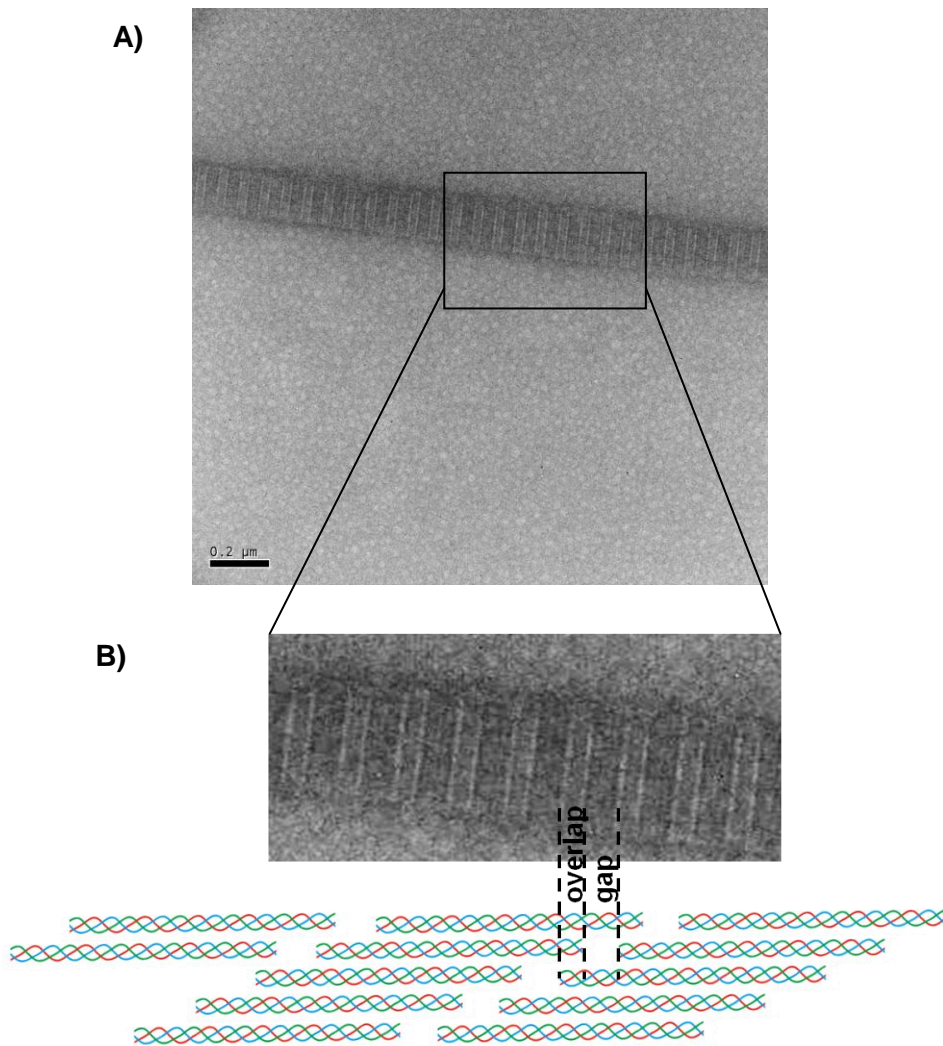


Figure 3.6. (A) Transmission electron micrograph of collagen fibrils formed at 20°C and (B) its correlation with the staggered organization of the individual molecules.

Chapter 4.

Dynamic Light Scattering

One of the fundamental requirements to investigate molecular interactions in a polymeric solution is to understand the characteristic physics of the polymer molecule. The size and shape of the polymer molecule, which correspond to its flexibility, determine the overlap concentration (see Chapter 1). In the field of rheology and polymer dynamics, there is considerable interest in determining the overlap concentration, at which molecules overlap and become entangled. Knowing the overlap concentration of collagen solutions not only provides information to interpret the concentration-dependent microrheological properties, but also helps interpreting the changes in these properties arising from variations in other molecular parameters (e.g. addition of salt or removal of telopeptides, Chapter 5).

In this chapter, dynamic light scattering (DLS) is used to study collagen size, with the purpose of determining an appropriate concentration range for microrheology experiments. These measurements may also provide some insight into the flexibility of collagen. In the following, first the theory of dynamic light scattering is introduced, followed by experimental studies on two well-characterized systems of sphere and rigid rod particles. Then, studies on collagen are performed and challenges for this system are explained followed by two different techniques used to overcome those challenges: ultrasonication and ultracentrifugation.

4.1. Theory

Light scattering is a technique that uses information from the dynamic fluctuations in the light scattered off a particle within a solution to learn about the particle's size and shape. When an incident beam of light passes through a polymer

solution, it scatters in all directions. In the technique of dynamic light scattering, dynamic fluctuations of the scattered intensity are measured via a detector at particular angle(s). The schematic drawing in Figure 4.1 represents the geometry for light scattering.

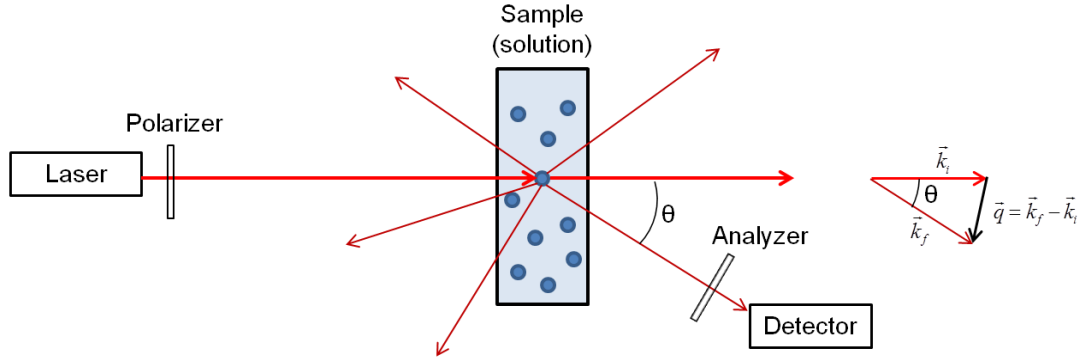


Figure 4.1. Schematic diagram of the light scattering technique: The laser light interacts with particles in a solution and scatters in different directions. When the scattered beam is monitored at an angle θ , the scattering vector \vec{q} is defined as the difference of the wavevector after and before scattering; this is shown geometrically on the right.

An incident beam with wavevector \vec{k}_i can scatter in several directions, each of which a wavevector, \vec{k}_f . The magnitudes of \vec{k}_i and \vec{k}_f are $\frac{2\pi n}{\lambda_i}$ and $\frac{2\pi n}{\lambda_f}$, respectively, where λ_i and λ_f are respectively the wavelengths of the incident and scattered laser beam in vacuum and n is the refractive index of the solvent. The scattering vector, \vec{q} , can be defined as the difference between the final and initial wavevectors. If the wavelength is only changed very little by the scattering process (as is the case for elastic scattering), the magnitude of scattering vector can be calculated as [143,144]

$$q = \frac{4\pi n}{\lambda_0} \sin\left(\frac{\theta}{2}\right), \quad (4.1)$$

where λ_0 is the wavelength of the laser beam in vacuum ($\lambda_0 = \lambda_i = \lambda_f$) and θ is the angle of the scattered beam with respect to the original direction of the light.

Fluctuations of the scattered light intensity as a function of time, $I(t)$, obtained by the detector, are related to the diffusion of particles within the solution. In order to obtain their diffusion constant, data analysis includes calculating the normalized autocorrelation function of the intensity of the scattered light. This is given by the following equation for a particular delay time, τ

$$g^{(2)}(\tau) = \frac{\langle I(t) \cdot I(t+\tau) \rangle}{\langle I(t) \rangle^2}, \quad (4.2)$$

in which $I(t)$ and $I(t+\tau)$ are the scattering light intensities at time t and $t+\tau$, respectively [144]. Because there is high correlation at very short delay times and almost no correlation at long delay times, the autocorrelation function decays, the rate of which depends upon the diffusion of particles. The numerator in Eq. (4.2) ranges from $\langle I^2 \rangle$ (for $t \rightarrow 0$) to $\langle I \rangle^2$ (for $t \rightarrow \infty$) [144]. Therefore, when the autocorrelation function is normalized, it ranges from a value greater than 1 to 1.

In the simplest case, a solution of monodisperse spherical particles, these measurements can be used to obtain their translational diffusion constant according to the following equation [144]

$$g^{(2)}(t) - 1 = \text{baseline} + b_0 \cdot \exp(-2Dq^2t), \quad (4.3)$$

in which q is given by Eq. (4.1) while *baseline*, b_0 , and D (diffusion coefficient) are the fitting parameters.

In the following sections, experimental details of the light scattering instrument are first presented, then, the results obtained for three different systems, microspheres, tobacco mosaic virus, and collagen, are described.

4.2. Details of the Light Scattering Instrument

All of the dynamic light scattering measurements presented in this work were performed on a light scattering instrument, ALV DLS/SLS 5000 spectrometer/goniometer (ALV-Laser GmbH) with a laser power of 23 mW at a wavelength of $\lambda_0 = 632.8$ nm in Dr. Frisken's lab.

4.3. DLS of a Spherical System

Polystyrene microspheres (diameter: 0.29 μm , Interfacial Dynamics) were tested as an example of a measurement on spherical particles of similar dimensions to collagen's molecular length (~ 300 nm, Section 3.1). Figure 4.2 shows the obtained curve and its corresponding fit with Eq. 4.3.

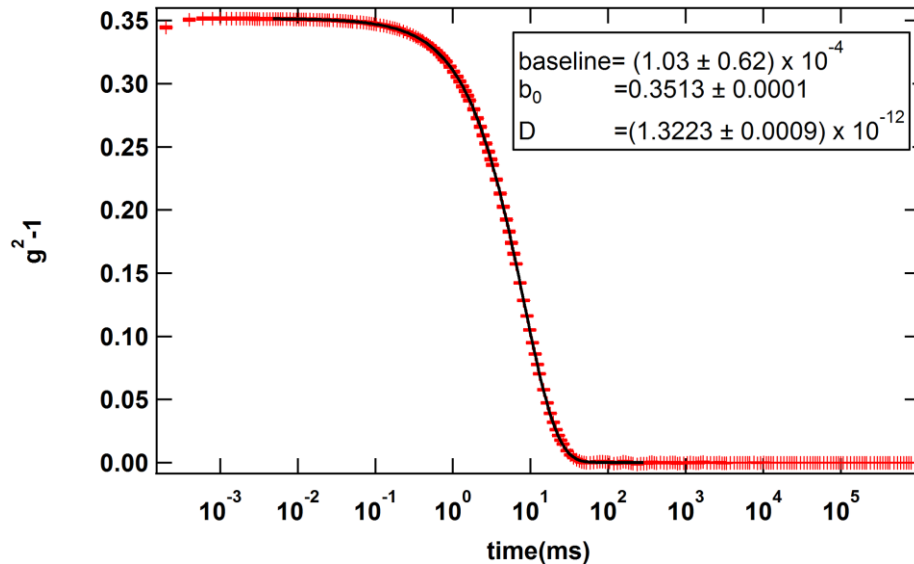


Figure 4.2. Correlation function for a solution of polystyrene microspheres (diameter= 0.29 μm , concentration ~ 0.004 wt % in nanopure water) measured at an angle of $\theta = 30^\circ$ (red crosses). The black line corresponds to the fit (only over the range shown) obtained from Eq. 4.3.

From the diffusion coefficient of the microsphere, the particle size can be found using the Stokes-Einstein equation [144]:

$$R_h = \frac{k_B T}{6\pi\eta D} \quad (4.4)$$

where k_B is the Boltzmann constant, T is the temperature in Kelvin, η is the solvent viscosity, and R_h is the hydrodynamic radius. Similar data were recorded and analysed at other angles, 40°, 54°, 70°, 90°, 120°. Using the average diffusion constant obtained from fits to the data at each angle, $(1.35 \pm 0.05) \times 10^{-12}$ m²/s, and the viscosity of water at 20°C (0.001 Pa.s), the hydrodynamic radius was calculated to be 159 ± 6 nm, which is very close to the nominal size of the microspheres, 145 nm.

4.4. DLS of a Rigid-Rod System

Tobacco mosaic virus (TMV) was chosen as an example of a rigid rod system similar in length to collagen and well-characterized with the dynamic light scattering technique [145,146]. Dimensions of these viruses as determined from electron microscopy technique are approximately 300 nm in length and 20 nm in diameter [147,148]. For this thesis, TMV was generously provided by Dr. Craig's lab as a stock solution of 22 mg/ml within a solvent of 50 mM Tris (pH=8). For these light scattering experiments, a final concentration of 0.1 mg/ml in 50 mM Tris was prepared.

The main difference in studying these particles compared to the spherical particles is that a rod-like or ellipsoidal particle has rotational diffusion in addition to translational diffusion [149]. For a rigid rod system, Eq. (4.3) changes to the following formula [150]

$$g^{(2)}(t) - 1 = \text{baseline} + \beta \cdot \exp(-2D_t q^2 t) \cdot (1 + B \cdot \exp(-6D_r t))^2, \quad (4.5)$$

where D_t and D_r are diffusion constants corresponding to the translational motion and rotational motion, respectively. In this equation *baseline* and β are additional fitting parameters, while B is an angle-dependent constant. Cummins *et al.* [146] suggested a mathematical method to calculate B , defined as a constant dependent only on $q \cdot L$, where L is the length of the particle.

Figure 4.3 shows the autocorrelation function and its corresponding fit obtained from a light scattering measurement on TMV particles. Both the translational and rotational diffusion coefficients obtained for TMV ($D_t=3.5\times 10^{-12}$ m²/s and $D_r=358$ s⁻¹) fall in the range of the values in literature [146], which range from 2.8×10^{-12} - 4.7×10^{-12} m²/s and from 290- 420 s⁻¹, respectively. The correlation data were recorded and analysed for other angles (35°, 40°, 47°, 54°, 62°, 70°, 80°, 90°, 104°, 120°), and obtained diffusion coefficients at all angles were in close agreement with the values in literature.

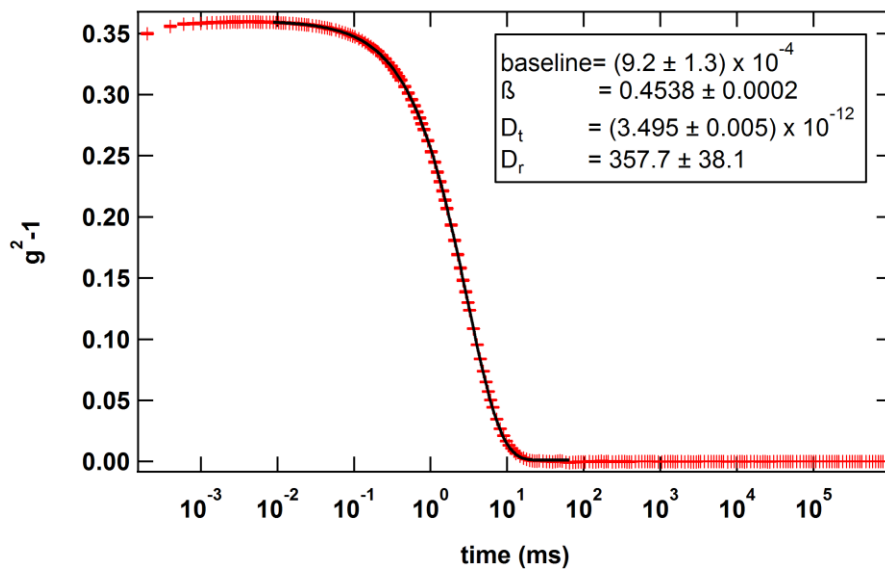


Figure 4.3. Correlation function obtained for a solution of TMV at a 30° angle. The black line shows the fit with Eq. (4.5), considering $B = 0.00925$. B is mathematically calculated using Ref. [146] at $\theta = 30^\circ$.

4.5. DLS of Collagen Solutions

The flexibility of collagen has been considered to lie anywhere from a rigid rod to a semi-flexible polymer [25,51] because the estimates of collagen's persistence length, l_p , range by an order of magnitude, from 15-160 nm [25,49,51,151], 20-2 times smaller than its contour length (~300 nm). Dynamic light scattering studies have been used to characterize the translational and rotational diffusion of collagen molecules in solution and consequently to quantify the size and flexibility of the collagen molecules

[51,150,152]. However, in some of these studies, the authors acknowledged that large nonspecific aggregates were present, which they tried to remove. In the following, my first attempts to use dynamic light scattering to obtain information about collagen flexibility will be presented. Because these initial results disagreed with previous reports, two different purification techniques were explored which will be presented, and the resultant DLS measurements compared to the expected values for collagen in the literature.

In all of the light scattering results presented here, the solvent is 20 mM acetic acid, therefore, no fibril formation is expected.

4.5.1. Effect of Collagen Concentration

For these measurements, collagen concentrations of 0.75, 0.5, 0.375, 0.25, and 0.1 mg/ml were tested at 11 angles each at 30°, 35°, 41°, 47°, 54°, 62°, 71°, 80°, 91°, 104°, and 120°. For each sample, data were collected for one hour at each angle. Figure 4.4 shows examples of the correlation function results obtained for 0.1 mg/ml collagen at 30° and 90°.

Hwang and Cummins [150] found for collagen that >99% of the scattering at 30° scattering angle is a result of translational diffusion, while at larger angles both translational and rotational diffusion are involved. Based on this observation, here, the translational diffusion coefficient, D_t , was first calculated by fitting the following equation to the 30° correlation data (Figure 4.4(A)):

$$g^{(2)}(t) - 1 = baseline + b_0 \cdot \exp(-2Dq^2t) \left(1 + \frac{\mu_2 t^2}{2}\right)^2, \quad (4.6)$$

in which μ_2 is the variance of the size distribution. Eq. (4.6) is a modification of Eq. (4.3), suitable for polydisperse samples. The equation is derived using the cumulant method [153]. Eq. (4.6) was more successful in fitting these data than Eq. (4.3). This may indicate that the collagen solutions used here were not monodisperse but included particles with different sizes. This will be further investigated later in this chapter.

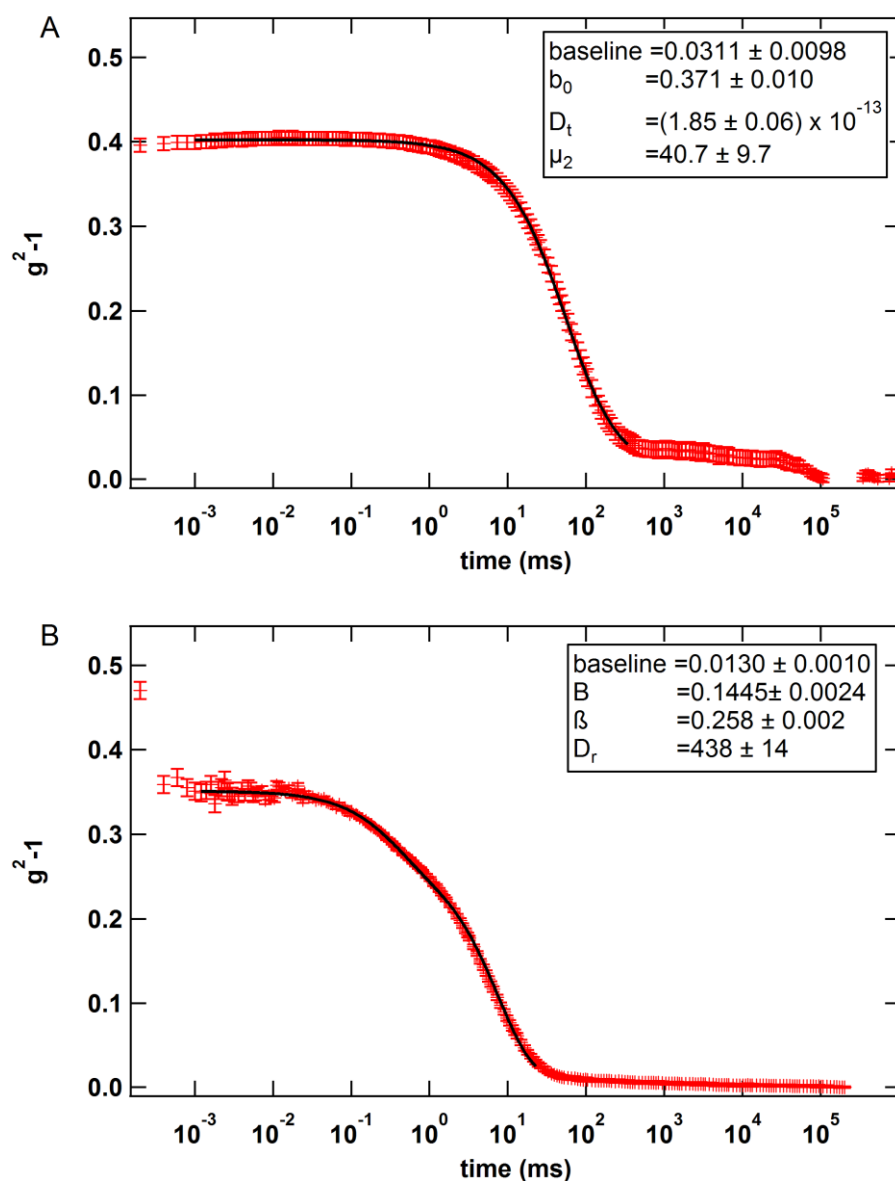


Figure 4.4. Correlation function for a solution of collagen (concentration: 0.1 mg/ml) at two angles of (A) 30° and (B) 90°. Translational diffusion is extracted from the data at 30° in (A) and it was fixed for the analysis in part (B). For definitions of the parameters and fit functions, see the text.

Following the analysis at a small angle, 30°, measurements at higher scattering angles were used to extract the rotational diffusion coefficient, D_r , using Eq. 4.5 and the value of D_t determined at 30°. As an example, the results obtained at 90° are shown in Figure 4.4(B). The light scattering measurements and analysis were similarly repeated for other concentrations and the results for both D_t and D_r are reported in Table 4.1.

Table 4.1. Calculated translational and rotational diffusion coefficients for different concentrations of collagen solutions

Concentration (mg/ml)	D_t (m^2/s)	D_r (1/s)
0.1	1.85×10^{-13}	438
0.25	1.11×10^{-13}	513
0.375	1.10×10^{-13}	403
0.5	6.76×10^{-14}	37.4
0.75	6.26×10^{-14}	24.1
Hwang and Cummins [150] (≤ 0.5 mg/ml)	7.20×10^{-12}	735
Clair and Pecora [51] (< 0.25 mg/ml)	8.4×10^{-12}	1110

There is a significant difference between the diffusion coefficients obtained for collagen solutions with concentrations of 0.5 and 0.375 mg/ml. This may have relevant meaning to the overlap concentration. That is, at collagen concentrations below 0.5 mg/ml, diffusion coefficients are not changing significantly with concentration. However, at concentrations of 0.5 mg/ml and greater, the diffusion coefficient drops significantly, due to fact that molecules are overlapping and their motion is restricted more than before.

It is clear from Table 4.1 that there exist discrepancies between the values of my measurements and the literature. The smaller diffusion coefficients obtained here suggest the presence of large structures, of which only a few in the solution can affect the results [150]. The origin of these large structures can be other proteins as an impurity in collagen stock solution or large aggregates of collagen. The first possibility seems to be less probable because of the fact that no significant traces of other proteins were observed in the protein gel electrophoresis experiment (Figure 3.2). In either case, the following experiments were performed in attempts to remove these large structures, with the aim of characterizing solutions of individual collagen molecules.

4.5.2. Ultrasonication Technique

In an attempt to break up the aggregates, an ultrasonic probe sonicator (Branson 450 Digital Sonifier) with 20 kHz frequency was used. The power (pulse on/off) was chosen to be 40 Watts, 10% of the maximum power. (Higher powers were found to create foam in the solution.) The vial containing the collagen solution was held inside an ice-water bath to limit heating of the sample. After sonication, the solution was filtered through a Supor® polyethersulfone membrane with a pore size of 0.2 μm (Pall Corporation).

The experimental results of the correlation function obtained for collagen solutions before and after sonication are plotted in Figure 4.5. Also plotted are the expected curves using three sets of values obtained in Ref. [51]. Although the experimental curves still do not agree with the previous reports, ultracentrifugation results in a shift of the curves towards the expected values. The fact that the correlation function decays at shorter times for treated solutions compared to the untreated one suggests that large structures are removed by sonication and filtration. This may indicate that removing the aggregates using this treatment is successful and longer sonication may be even more beneficial.

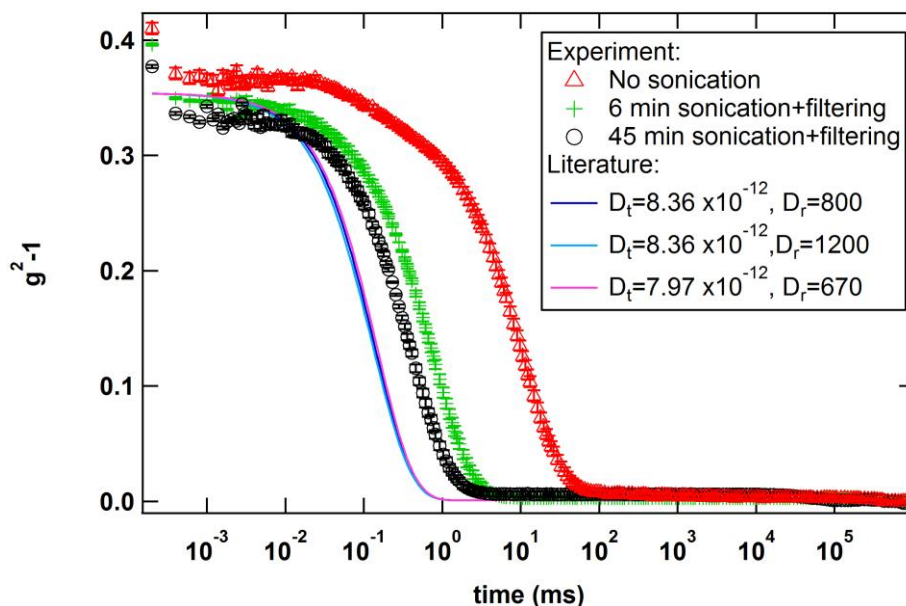


Figure 4.5. Comparison between correlation functions obtained for collagen solutions before sonication, after 6 minutes and after 45 minutes of sonication. The experimental data are compared with simulated curves based on three sets of values in Ref. [51] (all three of which appear indistinguishable here). All of the plots correspond to data taken at a scattering angle of 90° .

This finding is encouraging because the reduction of aggregates with this technique moves us towards individual collagen molecules in solution. However, it must be verified that what is left in the solution is collagen molecules. For this purpose, the two techniques of gel electrophoresis (Section 3.3) and ELISA (Section 3.4) were used to characterize the composition and concentration of collagen following sonication. Three collagen samples of untreated, 10-minute, and 20-minute sonication were examined. Figure 4.6 shows the gel image of these three samples when filtration is (A) and is not applied (B) following sonication. Unexpectedly, sonication results in the disappearance of collagen molecules from the samples.

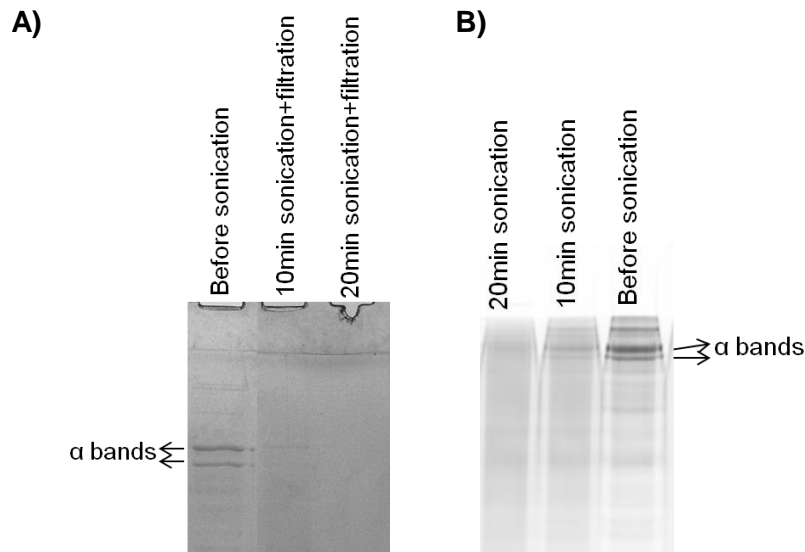


Figure 4.6. Gel image of A) sonicated (10 and 20 minutes) and filtered collagen samples and B) sonicated collagen samples. The sonication process seems to be disruptive to the collagen molecules due to the fact that collagen bands disappear after this treatment.

Concentrations of the three collagen samples described above obtained by the ELISA technique are shown in Table 4.2. These results are consistent with the observation in Figure 4.6, that collagen disappears from the sample.

Table 4.2. Collagen concentrations of the untreated, and 10- and 20-minute sonicated and filtered samples obtained by ELISA

Sample	Before sonication	10 min sonication	20 min sonication
Concentration (mg/ml)	1.1	0.57	N.D.

There exist two hypotheses regarding the disappearance of collagen even after sonication only (Figure 4.6(B)). Either collagen molecules are sticking to the probe of the sonicator, the extent of which increases with sonication time, or the ultrasonic waves are harmful for collagen molecules. Although there is not a detailed study on the effect of sonication on collagen molecules, ultrasound has been shown to affect covalent bonds in polymers and their reaction rates [154]. Also, studies on other proteins [155] have

shown that sonication can cause a wide range of changes in protein conformation and stability. Although the sonicated samples in this work still scatter light (Figure 4.5), it is not clear for us whether scattering is off the intact collagen molecules or molecules that lost their stability due to the sonication which perhaps made new aggregates with completely different conformations (e.g. amyloid [155]). Although both ELISA and gel electrophoresis experiments showed that the concentration of collagen is reduced by sonication, these techniques are not able to probe collagen's molecular conformation after sonication.

4.5.3. Ultracentrifugation Technique

As an alternative, gentler technique, high-speed centrifugation was used to separate larger aggregates from smaller sized molecules. As will be shown, this method is less destructive to collagen molecules compared to ultrasonication. This technique is also tunable since rotation speed and duration in the centrifuge can be chosen such that only aggregates greater than a particular size are settled (sedimented) while single molecules are still in solution.

In a centrifuge, the time needed for a particle to sediment can be calculated as the following [156]:

$$t = \frac{k}{S}, \quad (4.7)$$

where t is the time in hours, S is particle's sedimentation coefficient (in Svedberg units, symbol Sv), and k is the clearing factor (k-factor) of the centrifuge rotor, which represents its sedimentation efficiency in the units of Sv.hr. The higher the mass of a particle, the higher the sedimentation coefficient and hence, the faster it sediments at a particular centrifuge rotating speed.

The sedimentation coefficient is defined as the ratio of the sedimentation speed of a particle to its acceleration in comparable units [157]. One Sv is equal to 10^{-13} seconds. For example, a particle with the sedimentation coefficient of 10 Sv (10×10^{-13} s) and subjected to an acceleration of 10^7 m/s², moves with the speed of 10 μ m/s.

The following discussion explains the selection method for the centrifuge rotation time (Eq. 4.7) to separate large aggregates from collagen molecules. The goal is to choose a rotation duration (at a given speed), which is long enough for the aggregates to sediment, yet too short for the single molecules to sediment. To do this, the relationship between sedimentation coefficient and radius of the particle is defined. Then, the former parameter is estimated for the large aggregates. Finally, sedimentation times for collagen single molecules and aggregates are calculated, respectively.

The following equation relates the maximum possible sedimentation coefficient, S_{max} , to the molecular weight, M_w , in Daltons [158]:

$$S_{max} = 0.00361M_w^{2/3} \quad (4.8)$$

Assuming that $M_w \propto R^3$ (where R is the radius of the particle), then $S_{max} \propto R^2$.

In order to approximately quantify the size of the large aggregates, the method of CONTIN analysis of the DLS data was used. The CONTIN algorithm is based on the inverse Laplace transform of the autocorrelation function [159]. It produces the probability distribution of the decay times which can be used further to estimate the distribution of hydrodynamic radii within the system using the Stokes-Einstein relation, Eq. (4.4) [51]. An example of the results for the CONTIN analysis obtained for a collagen solution is shown in Figure 4.7. The main peak (here, >100 nm) provides a rough estimation for the hydrodynamic radius of large particles. The second peak located at smaller R_h may be attributed to single molecules of collagen because it corresponds to the same size as found by Claire and Pecora [51].

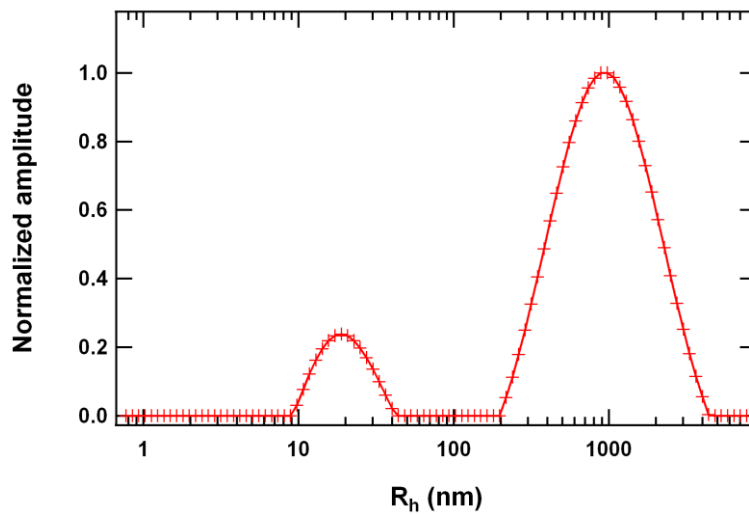


Figure 4.7. Size distribution spectrum obtained by CONTIN analysis of collagen solution at a 90° angle (data in Figure 4.4(B)). Note: this plot is an unweighted spectrum; therefore, large particles tend to have larger amplitude because they scatter more, not necessarily because they are more numerous in solution.

A collagen molecule with a hydrodynamic radius of ~ 30 nm [51] has a sedimentation coefficient of 3-4 Sv [160], and using $S_{max} \propto R^2$, for the aggregates of >100 nm, the sedimentation coefficient is calculated to be >30 Sv. Thus, I aimed to sediment these >30 Sv particles and not the $S \approx 3$ Sv collagen molecules.

A bench-top ultracentrifuge (Beckman Optima TLX) with a fixed angle rotor (TLA-45) was used. At a rotor speed of 40,000 rpm (72,128 g), the k-factor is equal to 126.3 Sv.hr. Therefore, Eq. (4.7) predicts that in order to sediment particles of $R_h > 100$ nm ($S > 33$ Sv), 3.8 hours will be needed. Based on these calculations, samples were chosen to be centrifuged at 40,000 rpm for 4 hours. This is still much shorter than the time to sediment single molecules (~ 40 hours).

Immediately after centrifugation, the sample was divided into four vertical layers by carefully pipetting out a quarter of the total volume from the top each time. Figure 4.8(A) shows a schematic and photograph of the four layers of a fluorescently labelled collagen solution after ultracentrifugation. Interestingly, there is a gradient in the blue color (presence of the collagen) going from the top to the bottom layer. This is a qualitative verification that large aggregates are collagen. A gel electrophoresis

experiment verifies this hypothesis (Figure 4.8(B)). The results show that after centrifugation, the bottom layers are enriched in collagen.

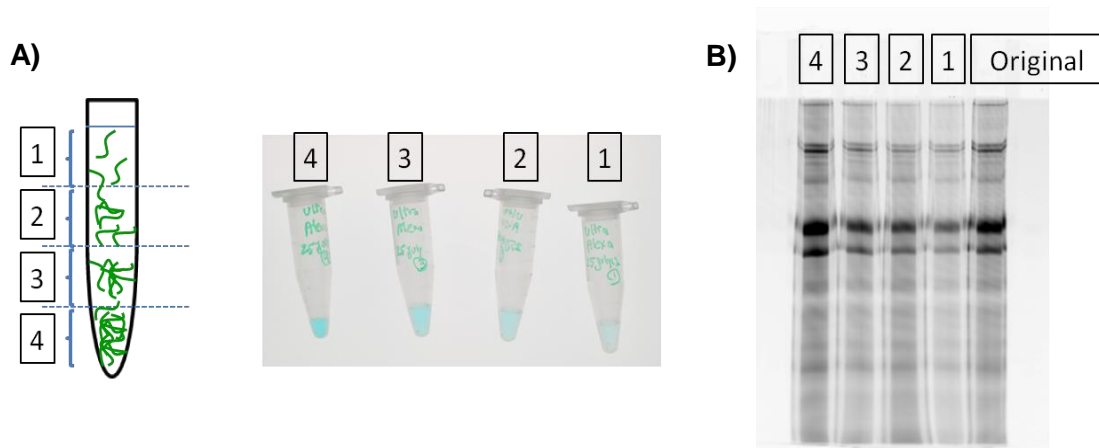


Figure 4.8. The total volume of the centrifuged collagen solution was divided into four layers and characterized (A) qualitatively by the gradient of the blue color in the labelled collagen and (B) by the intensity of the bands in the gel electrophoresis experiment. The schematic illustrates that the bottom layers are enriched in collagen after centrifugation.

Finally, a dynamic light scattering measurement was done on the top fraction of the ultracentrifuged sample. Figure 4.9 shows the autocorrelation function for this sample in comparison with the original collagen solution (non-centrifuged). For the ultracentrifuged sample, the measurement time (duration of the run) was selected to be 10 minutes (instead of 1 hour used for all previous light scattering measurements). The reason for this selection was to lower the chance of an aggregate (although much less frequent compared to the uncentrifuged sample) passing through the beam path and hence, its interference with the measurement.

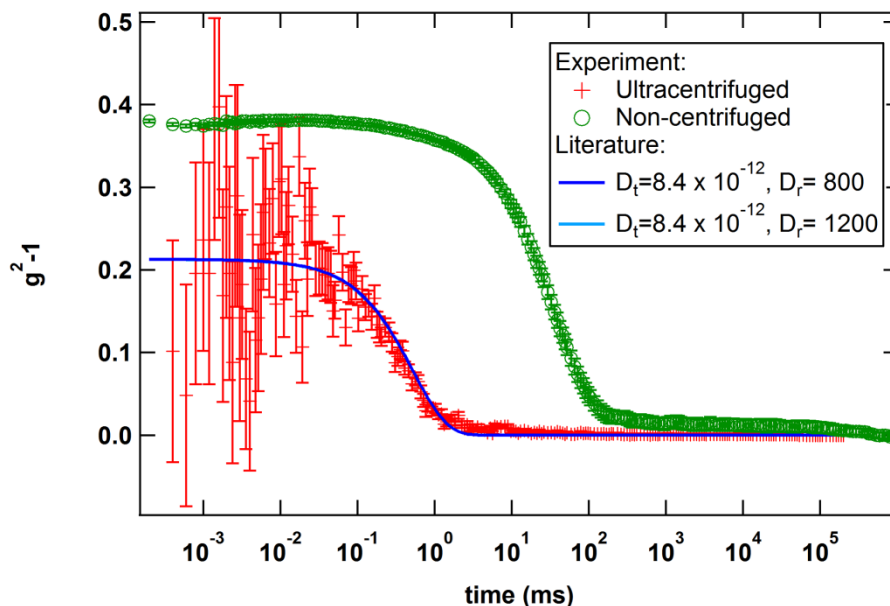


Figure 4.9. The correlation function for the ultracentrifuged collagen sample (red crosses) shows a significant reduction in decay time compared to the non-centrifuged sample (green circles). Results for the centrifuged sample are in a good agreement with curves plotted using values in the literature [51]. All curves correspond to data obtained at a scattering angle of 45° .

Due to the existence of the significant noise at short times, <0.1 ms, it is not possible to obtain a reliable fit to the obtained data for the centrifuged sample. However, two theoretical curves corresponding to the values obtained in the literature compare very well to these data, as shown in Figure 4.9. This suggests that ultracentrifugation separates the large aggregates to a great extent. The large noise at short times may be due to the fact that the ALV instrument used here is not sensitive enough to the scattering of these small molecules. Using a more powerful or shorter wavelength laser would be expected to increase the scattered light intensity and improve the signal to noise ratio of these data.

Claire and Pecora [51] have shown theoretically that diffusion coefficients obtained for collagen correspond to a semiflexible molecule ($l_p \sim 160\text{nm}$). The fact that my light scattering results are in agreement with these findings may suggest that collagen is a semiflexible molecule. However, a hypothetical correlation curve for a flexible molecule obtained by assuming $l_p \sim 15$ nm [25] for collagen is also in agreement with the experimental results (Figure 4.10). This hypothetical curve is simply a single

exponential correlation function (Eq. 4.3), in which the diffusion coefficient is estimated using Eq. (4.4) where R_h is related to R_g by $R_g/R_h \approx 1.5$ [161] and R_g is estimated as $R_g \approx \sqrt{\frac{l_p l_c}{3}}$ [59], in which l_c is contour length (300 nm). Also shown in Figure 4.10, the hypothetical correlation curve for a rigid rod molecule is in agreement with the experimental results, too. This hypothetical curve is based on Eq. (4.5) using translational and rotational diffusion coefficients estimated for a rigid rod molecule according to the following equations, theoretically found for rigid rod systems [51].

$$D_t = (k_B T / (3\pi\eta L)) [\delta - (1/2)(\gamma_{\parallel} + \gamma_{\perp})], \quad (4.9)$$

where,

$$\begin{aligned} \delta &= \ln(2L/d), \\ \gamma_{\parallel} &= 0.807 + 0.15/\delta + 13.5/\delta^2 - 37/\delta^3 + 22/\delta^4, \\ \gamma_{\perp} &= -0.193 + 0.15/\delta + 8.1/\delta^2 - 18/\delta^3 + 9/\delta^4, \end{aligned} \quad (4.10)$$

in which L is rod length and d is rod diameter (here, assumed to be 300 nm and 1.5 nm respectively). The rotational diffusion constant is given by

$$D_r = (3k_B T / (\pi\eta L^3)) (\delta - \xi), \quad (4.11)$$

where,

$$\xi = 1.14 + 0.2/\delta + 16/\delta^2 - 63/\delta^3 + 62/\delta^4. \quad (4.12)$$

In summary, using the series of light scattering measurements performed here, I was able to obtain a prediction for the overlap concentration (~0.5 mg/ml), however, it is not feasible to extract definite information for collagen flexibility based on this light scattering analysis (e.g. Figure 4.10). I will return to this issue of collagen's flexibility in the following chapter (Chapter 5), when viscoelastic properties of collagen solutions are compared to theoretical models.

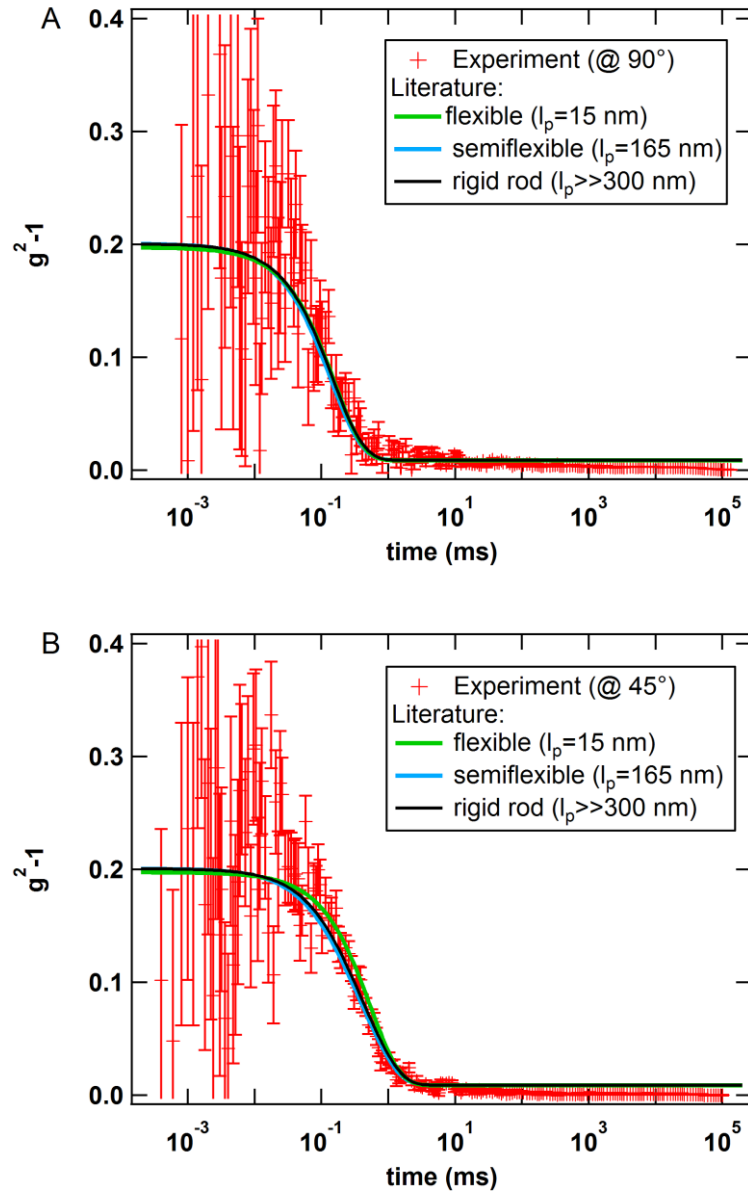


Figure 4.10. Results for the ultracentrifuged sample (red dots) are compared to theoretical curves assuming collagen to be flexible (green line; $l_p=15$ nm [25], $D_t=8.9\times 10^{-12}$ m²/s), semiflexible (blue line; $D_t=8.4\times 10^{-12}$ m²/s and $D_r=800$ 1/s [51]), or a rigid rod (black line; $D_t=7.8\times 10^{-12}$ m²/s and $D_r=660$ 1/s). It is not possible to easily distinguish which theoretical curve is in better agreement with my experimental data either at 90° (A), or 45° (B), although the larger difference at 45° suggests that measurements with improved signal to noise might help.

Chapter 5.

Solutions of Collagen Molecules

How the interactions of collagen molecules in solution correlate with their response to deformation is not known. In order to characterize the interactions between collagen molecules, the viscoelastic response of collagen solutions at acidic pH (where fibrils do not form) was studied. Tracking short-range motion of a probe particle allows us to obtain the frequency-dependent shear moduli at frequencies up to 20 kHz in our setup. This high-frequency microrheological measurement permits studies of viscoelasticity on timescales down to 50 μ sec, where transient interactions between constituent molecules can manifest and their effects on the mechanics of the system can be probed [65].

This chapter starts with a description of my studies on the concentration-dependent viscoelastic properties of collagen solutions. The frequency and concentration dependence of the shear moduli of these collagen solutions are interpreted based on viscoelastic models of polymeric systems. Then, the dependence of the size and charge of the probe particle on these measurements is investigated. The results of experiments aimed at uncovering the physicochemical basis for the observed viscoelasticity, which alter ionic strength and collagen's composition, are then presented.

Section 5.2 describing the viscoelastic properties and models of collagen solutions, and Section 5.4, describing the effect of salt, were adapted from my publications [162] and [163], respectively.

5.1. Experimental and Analysis Details

Collagen type I (rat tail tendon) was purchased as a stock solution with a concentration of 5 mg/ml in 20 mM acetic acid (Cultrex Invitrogen), acidic conditions (pH=3.3) in which collagen does not form fibrils. Concentrations below 5 mg/ml were obtained through dilutions in 20 mM acetic acid. Polystyrene microspheres were added to collagen solutions at a final concentration of $\sim 5 \times 10^{-4}$ % w/v. Throughout this thesis work, polystyrene microspheres were carboxylate-functionalized with diameter ~ 2.10 μm (Spherotech) except for experiments presented in Section 5.4, where amine-functionalized polystyrene microspheres (diameter ~ 2.19 μm ; Spherotech) and carboxylate-functionalized polystyrene microspheres with a different size (diameter ~ 3.17 μm ; Spherotech) were tested for comparison.

In Section 5.5 where the effect of salt is investigated, sodium chloride and potassium chloride were added to the acetic acid solution to give final concentrations of 273 mM and 5 mM, respectively. Removal of telopeptides is done using pepsin digestion (Section 5.6).

The complex shear moduli presented here are an average measured by ten different probe particles, with error bars representing the standard error of the mean values. Because collagen solutions possess little elasticity at low frequencies, as stated in Chapter 2, subtraction of $G'_{measured}$ at the lowest frequency (the third correction method) was used to correct for the elasticity of the optical trap.

5.2. Effect of Ultracentrifugation on Viscoelastic Properties

In order to validate my interpretations before studying concentration-dependent properties, here, one remaining question from the light scattering experiments (Chapter 4) is briefly discussed. In the previous chapter, it was shown that there exist some large aggregates within the solution and they seem to be mainly collagen. The question is whether or not they affect the results of the microrheology experiments.

Three hypotheses exist: 1) There are many permanently formed aggregates present and hence, microrheology experiments are looking at a multiphase system

containing single molecules and aggregates. Therefore, when the aggregates are removed, different rheological properties are to be expected compared with the original sample. 2) Aggregates are very sparse. Therefore, viscoelastic properties should be similar before and after removal of the aggregates. 3) Aggregates are only transiently formed. Therefore, even after removal of the aggregates by ultracentrifugation, aggregates may be re-formed depending on their formation rates. This latter hypothesis seems to be less plausible because aggregates were not seen neither shortly after nor a few days after ultracentrifugation.

To test for the first two hypotheses, the concentration of the top fraction of the ultracentrifuged collagen solution (Figure 4.8) was first obtained using the ELISA assay: ~ 0.7 mg/ml. Then, microrheological measurements were performed on the non-centrifuged and ultracentrifuged samples at this concentration, with results shown in Figure 5.1(A). There is not a significant difference observed between the properties of the two samples. The identical procedure was performed on a sample with higher initial collagen concentration, which led to 4.7 mg/ml concentration after centrifugation. Comparison of the viscoelastic properties before and after ultracentrifugation of this sample is shown in Figure 5.1(B).

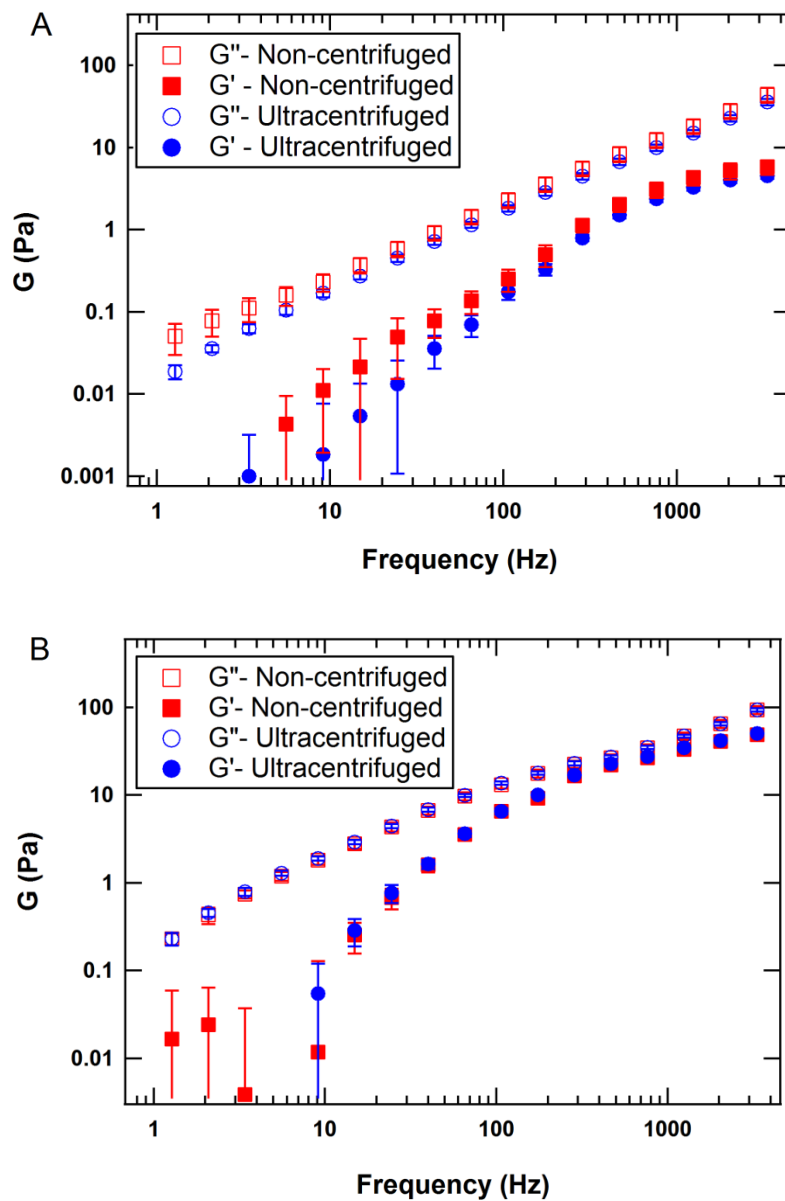


Figure 5.1. Viscoelastic properties of collagen solutions with and without ultracentrifugation treatment at concentrations of (A) 0.7 mg/ml and (B) 4.7 mg/ml.

Given that there is not a significant difference in viscoelastic properties of collagen solutions before and after ultracentrifugation, the second hypothesis is more consistent with my observations. Therefore, none of the following samples were centrifuged, and when interpreting the results, I treat the sample as a solution of collagen molecules.

5.3. Concentration Dependence of Viscoelastic Properties

Figure 5.2 shows the concentration dependence of collagen's viscoelastic response. Both elastic and viscous moduli increase with concentration. This behaviour is expected because the presence of more polymers in solution and interactions between them increase the viscoelasticity of the system.

The magnitudes of G' are smaller than G'' at all but the highest concentration studied, showing that collagen molecules in acidic solution represent a system dominated by viscous interactions. The low elasticity likely arises from limited entanglement between collagen molecules due to their short contour length (300 nm) [113,164] and from limited intermolecular attraction, arising from their overall positive charge at this acidic pH and the shielding of electrostatic interactions beyond intermolecular separations of ~ 13 nm (the Debye length for the 0.6 mM ionic strength of 20 mM acetic acid, described in more detail in Section 5.5).

There is, nonetheless, clear evidence that interactions between chains, whether through entanglement, local interactions such as electrostatic, hydrophobic, van der Waals, or hydrogen bonding, do occur, as the shapes of the frequency-dependent moduli change with increasing collagen concentration. At the highest concentration measured here (5 mg/ml), the elastic modulus becomes comparable in magnitude to the viscous modulus at frequencies above ~ 100 Hz (Figure 5.3), demonstrating the role that intermolecular interactions play in conferring elasticity to the system on the few millisecond timescale.

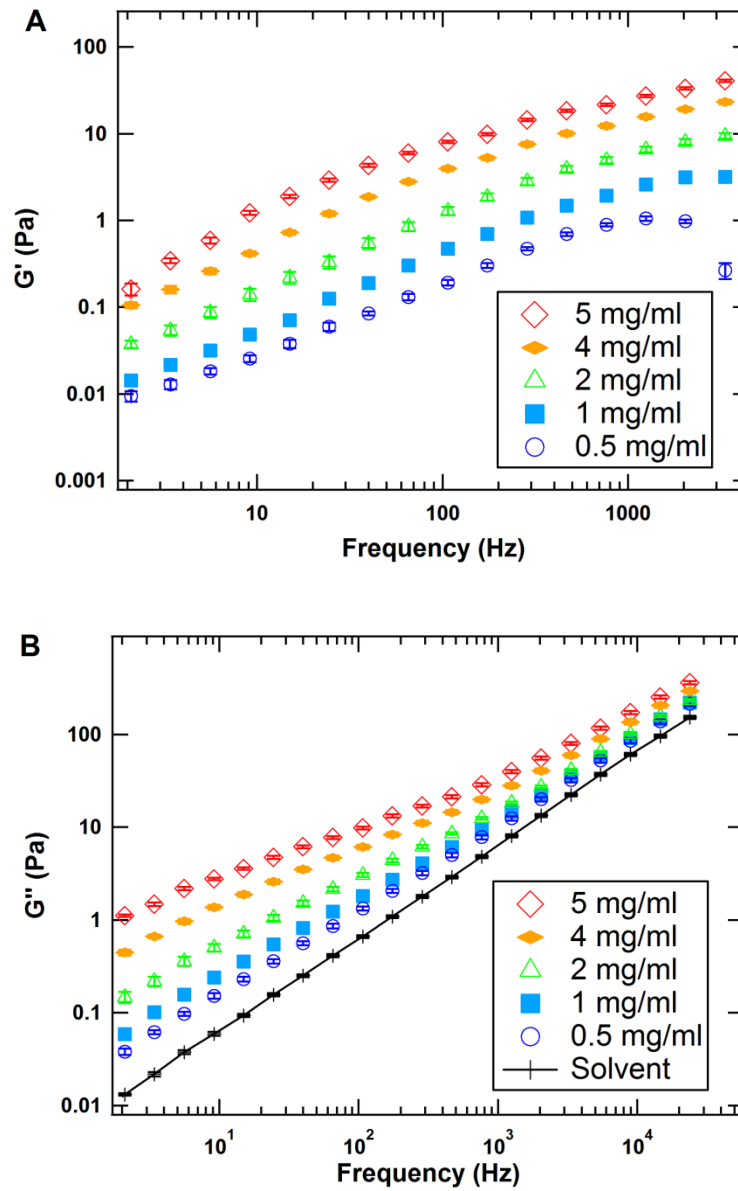


Figure 5.2. (A) Elastic and (B) viscous moduli increase with collagen concentration from 0.5 to 5 mg/ml (in 20 mM acetic acid). The viscous modulus of the solvent (20 mM acetic acid) is plotted in (B) for comparison. Values presented are averages over 10 independent measurements at each concentration of collagen, with error bars representing the standard error of the mean.

At this highest concentration, molecular collagen solutions clearly possess frequency-dependent viscoelasticity. To quantify this, the power law scaling of G' and of G'' with frequency is analyzed in different frequency ranges (Figure 5.3). For G'' , this scaling was determined from the reduced viscous modulus ($G''_R = G'' - (2\pi f)\eta_s$), in

which η_s is solvent viscosity) to reflect the properties of collagen and not solvent [60]. At low frequencies ($f < 15$ Hz), the log-log slope of G' with frequency is ~ 1.2 , while that of G''_R is ~ 0.6 . At intermediate frequencies ($100 \text{ Hz} < f < 2 \text{ kHz}$), this scaling decreases to ~ 0.5 for both G' and G''_R . At the highest frequency range of these measurements ($2 \text{ kHz} < f < 20 \text{ kHz}$), the scaling of G''_R with frequency is ~ 0.6 . (At this frequency range, the scaling of G' with frequency should not be determined because the extracted values underestimate the true G' due to the finite integration, as discussed in Section 2.5.)

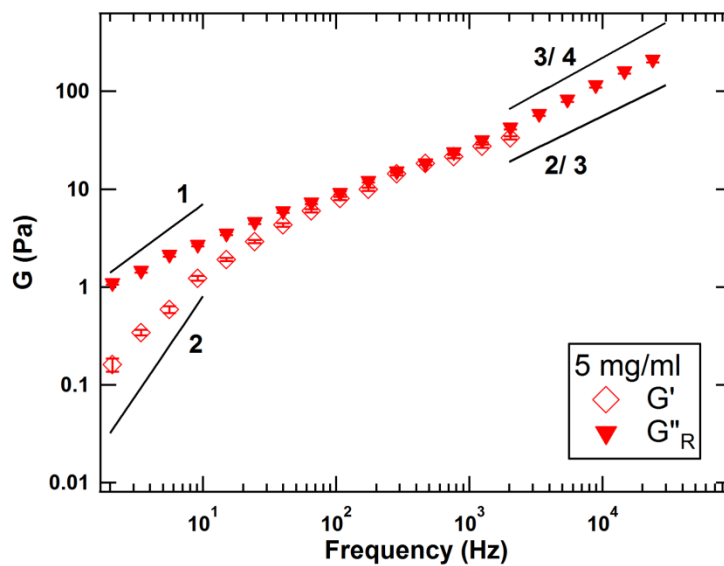


Figure 5.3. The reduced viscous modulus, G''_R (filled triangles), is plotted along with elastic modulus for solutions of 5 mg/ml collagen. The solid lines at low frequency represent the expected Maxwell scaling of the moduli. At high frequency, slopes of the lines indicate possible frequency-dependent scaling of moduli for flexible ($3/4$) and semiflexible ($2/3$) polymers.

The discussion below focuses on viscoelastic models which may describe the viscoelastic behavior of collagen solutions. At sufficiently low frequencies, the response of these collagen solutions is governed by their slowest relaxation process and should approach the Maxwell limit: $G' \propto f^2$ and $G'' \propto f$ (which are shown as solid lines at low frequencies in Figure 5.3). For dilute semiflexible chains in solution, the slowest relaxation process is governed by entropic orientational reorganization (well described by rotational diffusion of rigid rods) [165]. For higher concentrations, this relaxation

process involves disruption of interactions between chains, which can include hydrophobic interactions as well as physical entanglement [166]. At the lowest frequencies of my measurements, I find frequency-dependent scaling of G' that increases with concentration (from ~ 0.7 to ~ 1.2 ; Figure 5.2(A)), while the exponent best describing the low-frequency relationship between G''_R and frequency decreases with concentration (from ~ 0.9 to ~ 0.6 ; the trend can be seen in G'' versus frequency in Figure 5.2(B)). Thus, down to frequencies of 1 Hz, collagen solutions in this concentration range do not exhibit Maxwell scaling. Future studies extending the measurement times could investigate whether Maxwellian behavior is achieved and at what timescale. As introduced in Chapter 1, viscoelastic models can provide important analytical insights in predicting and simulating materials functions, for example stress relaxation behavior using the Maxwell model.

For the highest collagen concentration in our work, G' and G'' become comparable in magnitude and slope in the intermediate frequency range (~ 100 Hz – 2 kHz). The softening of the slope in this range, rather than a true plateau, indicates that relaxation via chain curvature and tension both likely contribute in this frequency interval [75].

At sufficiently high frequencies, the response of the system should be that of isolated chains in solution, at which point the power-law scaling of both moduli approaches the same limit in an isotropic system [63,75,113]. For the highest concentration probed, the slopes of G' and G'' are similar in the mid-frequency range ($100 \text{ Hz} < f < 2 \text{ kHz}$) of these measurements (Figure 5.3). Because only the viscous modulus $G''(f)$ can be correctly determined at high frequency ($f > 2 \text{ kHz}$) from these optical tweezers measurements, I examine its scaling in this short-time regime. At the highest concentration studied here, the high-frequency (2-20 kHz) slope of $\log(G''_R)$ vs. $\log(f)$ is approximately $\frac{2}{3}$ (Figure 5.3), a value commensurate with predicted scaling for Zimm polymers [60]. Numerous lines of evidence suggest, however, that measurements are not performed at high enough frequency to probe the dynamics of individual chains.

First, because estimates of collagen's persistence length (l_p) vary by an order of magnitude, from ~15-160 nm [25,49,151,167,168], giving a ratio of l_p/l_c ranging from $1/20$ - $1/2$ when compared with its contour length of $l_c=300$ nm, it may fall in the "crossover region" between rigid rods and random coils in which l_c is not much larger than l_p [165]. These previous measurements do not resolve whether collagen is better considered as semiflexible or as a freely jointed random coil, which the high-frequency scaling of the complex shear modulus could address. For semiflexible chains, the high-frequency scaling of both moduli should approach $G \propto f^{3/4}$ [62,75], while the Zimm model for random coils predicts a $2/3$ scaling, as observed for 5 mg/ml collagen at the highest measured frequencies. (Semiflexible chains may also exhibit $2/3$ scaling at intermediate frequencies, through the relaxation of long-wavelength ($> l_p$) modes [75].) Because this observed scaling does not hold at lower concentrations (see below), it is unlikely the short-range relaxation of isolated chains is captured in this frequency range. To resolve this, measurements at higher frequency (shorter relaxation timescales) could be performed to assess the true high-frequency scaling relationships attributable to individual chain dynamics. Computer simulations probing the viscoelastic response of a single collagen triple helix found that intramolecular relaxation occurs on the timescale of a nanosecond [167], orders of magnitude faster than accessible with optical-tweezers-based microrheology.

Second, I find that the high-frequency scaling exponent depends on collagen concentration. As concentration decreases, the exponent increases, reaching ~0.9 for 0.5 mg/ml. This is significantly larger than the conventional $3/4$ relationship expected for semiflexible chains and is in closer agreement with the $f^{7/8}$ scaling recently found for certain high-frequency relaxation modes in these systems [63]. $7/8$ scaling occurs for longitudinal relaxation (parallel to the local polymer chain), and these modes are likely to dominate over transverse relaxation ($3/4$ scaling) for anisotropic systems or strained polymers [63,169]. In the isotropic collagen solutions of this part of my study, $3/4$ scaling is expected for semiflexible chains, and my results thus suggest that even for the most

dilute samples studied here, interchain interactions contribute to the viscoelasticity at ~10 kHz (100 μ sec timescales).

Third, if viscoelasticity is due only to the dynamics of isolated chains, it is expected that the moduli scale linearly with concentration, as more (isolated) molecules simply increase the amount of elasticity and dissipation experienced by the probe particle. To investigate this concentration dependence, in Figure 5.4 the moduli G' and G''_R are rescaled by dividing by collagen concentration, c . In the intermediate frequency range, the linear rescaling with c provides curves of G' that appear to converge at the lowest concentrations. However, this does not happen with G''_R/c , where the relatively larger rescaled values for the lowest concentrations imply that the reduced viscous modulus scales sublinearly with concentration.

Correspondingly, it is tested whether the concentration range studied here might better be represented by a $c^{0.5}$ dependence of G''_R (see discussions below about specific viscosity for justification). As seen in Figure 5.5, rescaling G''_R by dividing by $c^{0.5}$ produces curves that more closely converge in the high-frequency limit, although this does not happen for G' .

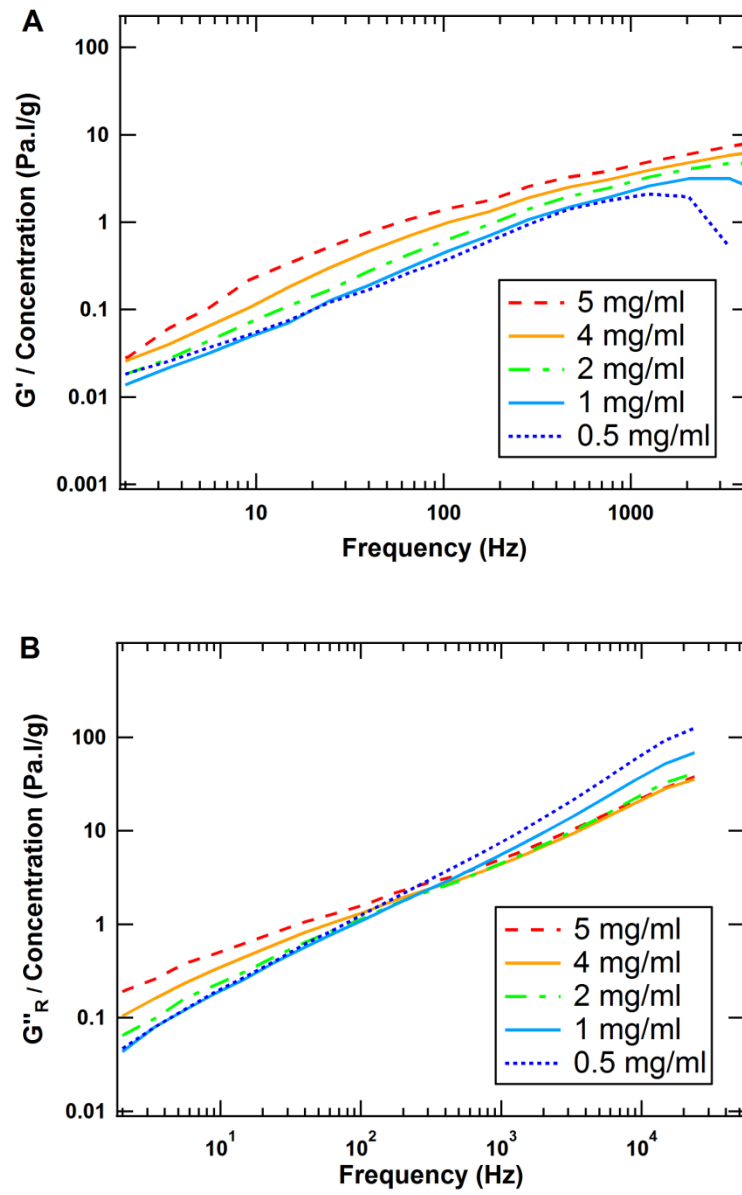


Figure 5.4. (A) Elastic and (B) reduced viscous moduli divided by sample concentration, c . While the lowest concentration of G' values appears to scale linearly with concentration, this is not the case for G''_R .

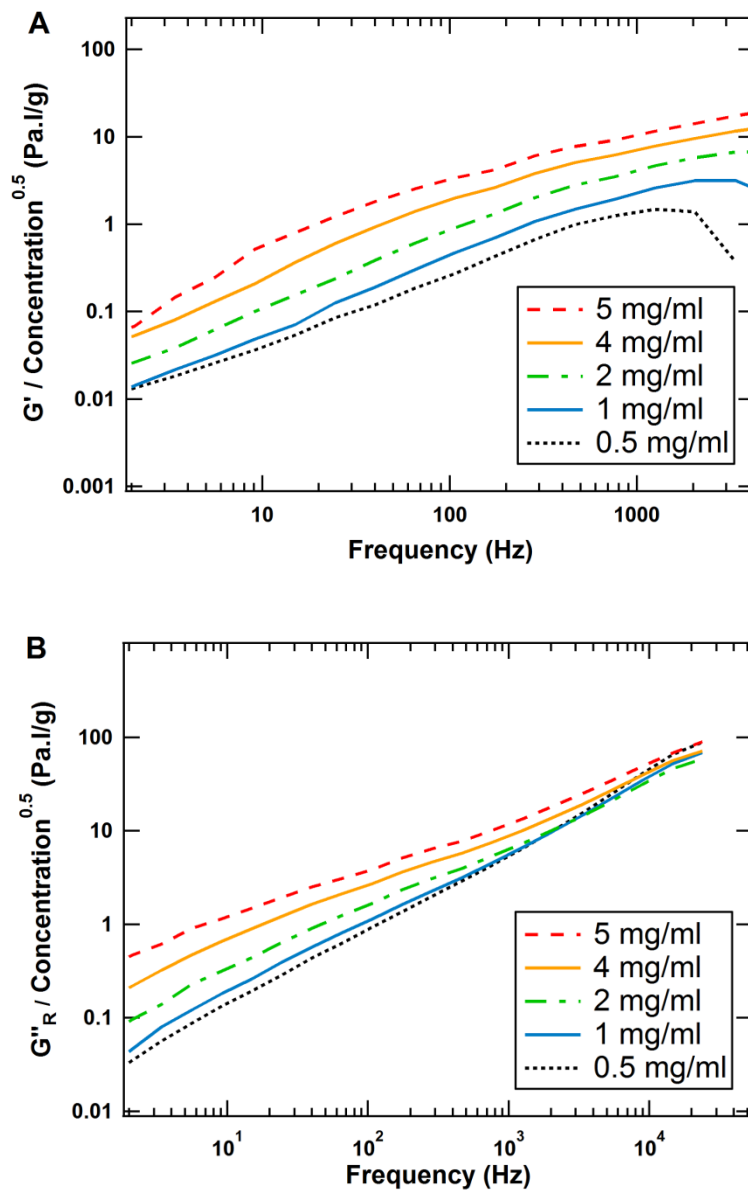


Figure 5.5. (A) Elastic and (B) reduced viscous moduli divided by the square root of sample concentration, c . The reduced viscous modulus, G''_R , appears better to rescale with $c^{0.5}$ at high frequency, although not the elastic modulus.

The frequency-dependent viscosity of collagen solutions, calculated from G'' using Eq. (2.14), is plotted in Figure 5.6(A) for different collagen concentrations. Moreover, the specific viscosities are calculated and plotted as a function of the concentration in the limit of $f \rightarrow 0$ (Figure 5.6(B)). Specific viscosity can be calculated as the following [170],

$$\eta_{sp} = \frac{\eta - \eta_s}{\eta_s}, \quad (5.1)$$

in which η_s is the viscosity of the solvent (here, 0.001 Pa.s).

The dependence of the values of specific viscosity extrapolated to zero frequency on concentration has been used to determine whether the solution is in the dilute, semidilute, or concentrated regime [93,171]. At low concentrations of uncharged polymers, specific viscosity increases linearly with the concentration [172]. However, it has been shown that at similar concentrations of polyelectrolytes, viscosity is proportional to the square root of concentration, $\eta_{sp} \propto c^{0.5}$ [173,174] and at higher concentrations, different scaling factors may be observed (e.g. scaling as $c^{1.5}$ in solutions of hyaluronic acid [93,175] or as $c^{4.1}$ in chitosan solution [174]). Having several ionizable groups along the collagen molecule, collagen solutions are likely best considered as polyelectrolyte solutions. As shown in Figure 5.6(B), analysis of my results for the power-law scaling of specific viscosity versus concentration shows a transition close to 1 mg/ml. This concentration is close, although not identical, to the 0.5 mg/ml concentration obtained from light scattering measurements (Chapter 4).

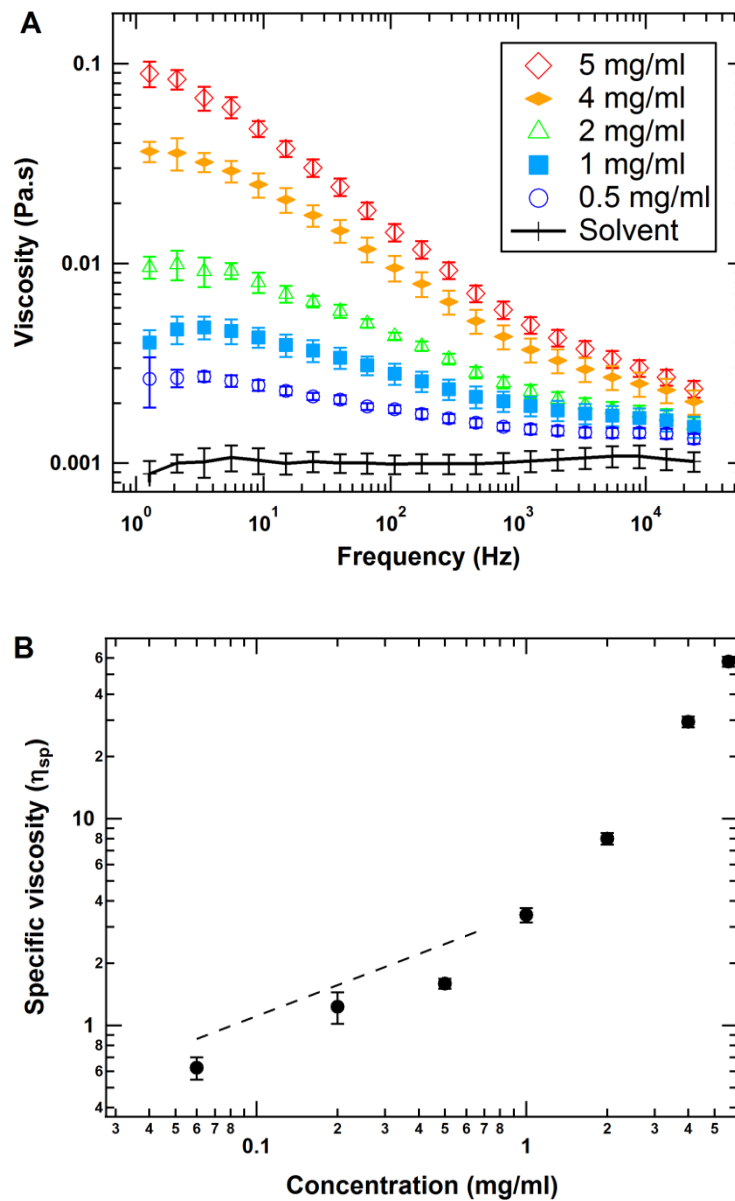


Figure 5.6. (A) The viscosity of collagen solutions (obtained from G'' using Eq. 2.14) is also frequency-dependent and increases with collagen concentration. Black symbols connected with lines show the viscosity obtained for the solvent, which is in good agreement with that of water at room temperature (0.001 Pa.s). (B) Specific viscosity of collagen solutions at different concentrations shows a change in slope between 0.5 and 2 mg/ml collagen concentrations. Dashed line corresponds to slope of 0.5.

The finding that, to be in the dilute regime, collagen concentration should be below 1 mg/ml, contrasts with an earlier estimate of an overlap concentration of ~ 2.5 mg/ml for collagen in acidic solution [176]. As discussed in Chapter 1, the overlap concentration is the concentration at which molecules in a solution start to physically

contact, which therefore changes the scaling of viscoelastic properties of the solution [60]. At a concentration of 1 mg/ml, the average distance between centers of isotropically distributed collagen molecules in solution would be 79 nm. Using a molecular weight of 300 kDa for collagen, 1 mg/ml concentration is equivalent to a volume per individual collagen protein of $4.9 \times 10^5 \text{ nm}^3$. This separation is less than collagen's contour length of 300 nm, while it is larger than its estimated radius of gyration were it a chain with the shortest estimated persistence length, $l_p = 15 \text{ nm}$ ($R_g \sim 38 \text{ nm}$). Thus, an overlap concentration below 1 mg/ml is physically reasonable. To achieve insight into the scaling laws of isolated collagens, and to confirm that they are semi-flexible, requires either extending the measurements to higher frequency and/or to lower concentrations.

The investigated concentrations are lower and the frequencies higher than most previous studies of collagen viscoelasticity [49,151,176,177], and, for the first time, apply the technique of microrheology to examine acidic solutions of collagen. There is wide variation among the few published values for G' and G'' for this low range of concentrations of collagen in acidic conditions. The magnitudes found here are very similar to the earliest published rheology studies by Nestler *et al.* across their entire studied frequency range (150-8000 Hz), and, consistent with their findings across a range of collagen concentrations $c < 1 \text{ mg/ml}$, that G'' is larger than G' [49]. A more recent study found G' and G'' to be considerably larger (e.g. $G' > 10 \text{ Pa}$ vs. $G'' \sim 3 \text{ Pa}$ for 5 mg/ml at 10 Hz) and have commensurately lower crossover frequencies, at which G' and G'' become comparable [177]. It is not clear why these latter values were found to differ from other reports, yet some plausible explanations are the difference in the source of collagen (bovine versus rat tail) and/or the different shearing environment between their experiment and ours. The latter means it is possible that the larger strain (5%) applied on the system in Ref. [177] pushes the rheological behavior to the non-linear regime (where polymer molecules are stretched out due to flow [36]).

5.4. Effect of Charge and Size of Probe Particles

In this section, I address two factors related to the probe particle, which may bias the microrheology results in a systematic way: surface charge and size of the probe particle.

Chae and Furst [178] investigated the effect of surface chemistry of the probe particle on microrheology of filamentous actin solutions. They found that depending on the interactions between the probe's surface and surrounding polymers, a depleted layer may be formed due to the exclusion of actin filament orientations near the particle. Although long length and rigidity of actin filaments play a significant role in creating the depleted layer, this phenomenon was also seen in solutions of DNA [179], which is more flexible than actin filaments.

In order to investigate the effect of surface chemistry, microrheology measurements of collagen solutions (5 mg/ml) were performed using beads with two different surface modifications, separately: carboxylate-functionalized (either neutral or negatively charged at pH~3.5) and amine-functionalized (positively charged at pH~3.5). As shown in Figure 5.7, there is not a significant difference in either the magnitude or the frequency-dependent variations of viscoelastic properties between the two probe surface charges. The slight difference between the two measurements is most likely due to the minor differences in collagen concentration.

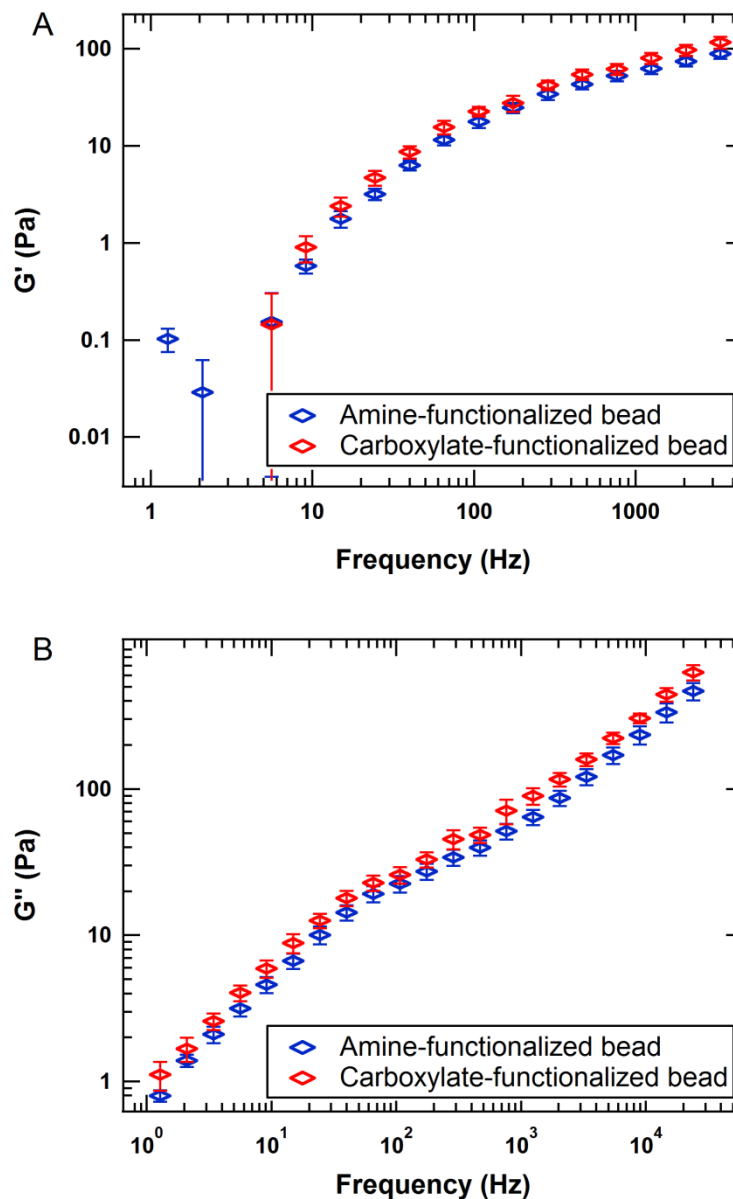


Figure 5.7. (A) Elastic and (B) viscous moduli for solutions of 5 mg/ml collagen probed with polystyrene beads (diameter $\sim 2 \mu\text{m}$) with two different surface chemistries: carboxylate-functionalized and amine-functionalized.

Another important factor related to the probe particle is its size. He and Tang [180] studied the probe-size-dependent microrheology of actin networks and found that as the probe diameter increases, the measured moduli change until they reach a plateau level. Thus, they suggest choosing probe diameter big enough to reduce the effect of probe size dependence. They find an optimal probe diameter several times larger than the network mesh size, in order to eliminate the probe size dependence [61,180]. Probe

sizes on the order of the mesh size, however, can be used to observe deviation of microscopic properties from macroscopic ones and hence, to map out spatial inhomogeneities in polymer systems [61]. The latter case is discussed more in Chapter 6.

It has also been shown that entropic depletion, due to the exclusion of certain filament orientation near the bead's surface, can be investigated using different sizes of probe particles [178]. The highest concentration of collagen in my experiments (5 mg/ml) is equivalent to a volume per individual collagen protein of $9.9 \times 10^5 \text{ nm}^3$, or an average spacing between collagens of 46 nm. Although the probe diameter of $\sim 2 \text{ }\mu\text{m}$ used in this thesis is several times greater than the hypothetical mesh size, an experiment was conducted to verify the independence of results from probe size. Figure 5.8 shows the results for the viscoelastic properties of a solution of collagen (5 mg/ml) measured using beads with diameters of 2 and 3 μm . Because of the concentration dependence of collagen's viscoelasticity, for these measurements one collagen solution was prepared. Because no significant difference in G' nor G'' is observed, it is verified that the viscoelastic properties measured with this range of probe diameter are not affected by the probe size. Given this observation, depleted layer thickness, if any, does not scale with probe size.

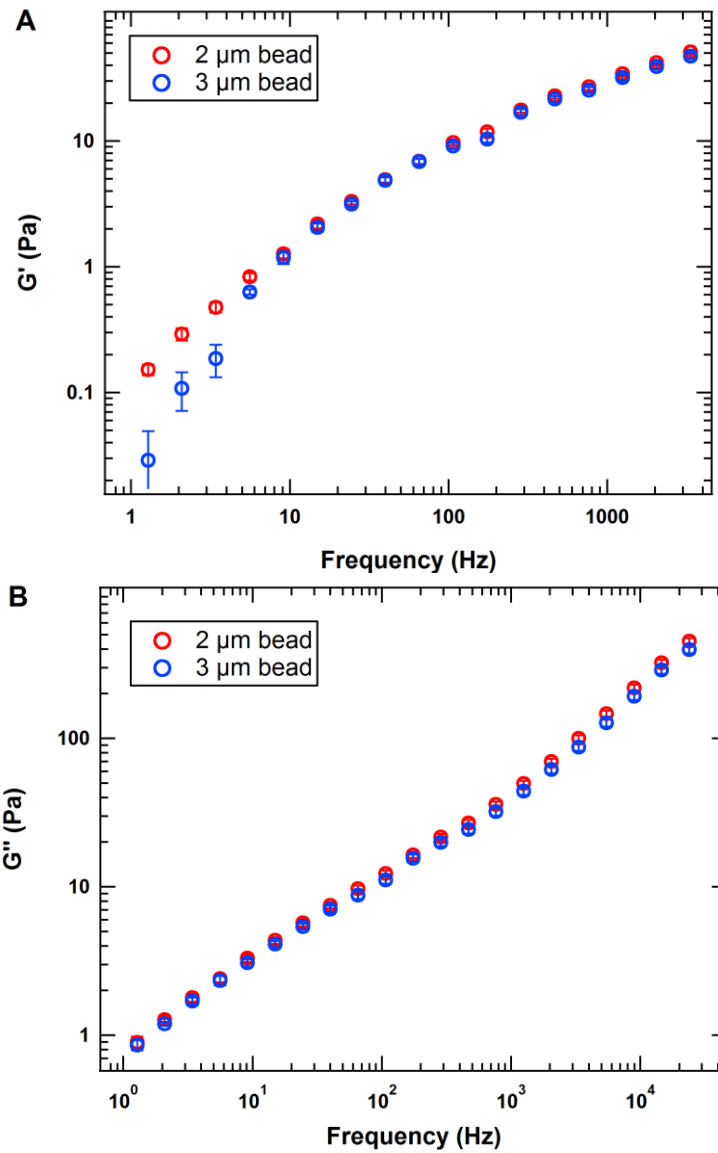


Figure 5.8. (A) Elastic and (B) viscous moduli for a solution of 5 mg/ml collagen probed with polystyrene beads with two different diameters: 2 μm and 3 μm . This work was performed in collaboration with Dr. Tuba Altindal, a postdoctoral researcher in the lab.

5.5. Effect of Salt

Collagen's intermolecular interactions are strongly affected by pH and salt concentrations [132]. By altering electrostatic interactions in the system at a specific pH, I investigated their role in conferring elasticity to collagen solutions. To do this, the highest collagen concentration of 5 mg/ml in 20 mM acetic acid (pH~3.5) was selected. In some samples, sodium chloride and potassium chloride were added (final concentrations of 273 mM and 5 mM, respectively). These concentrations were chosen to be identical to their concentrations when fibrils are formed (Chapter 6), though here because the solvent is not neutralized, fibrils do not form.

As shown in Figures 5.9(A) and (B), the moduli measured for solutions with and without salt are almost identical. Could this be due to the fact that the average distance between collagen chains in solution is larger than the effective electrostatic interaction distance? That is, is the length over which electrostatic charges are screened, the Debye screening length (λ_D), shorter than the average separation between molecules?

The Debye length is calculated using the following equation [181]

$$\lambda_D = \sqrt{\frac{\epsilon_0 \epsilon_r k_B T}{2N_A e^2 I}}, \quad (5.2)$$

where ϵ_0 is the permittivity of free space, ϵ_r is the dielectric constant of the medium, k_B is the Boltzmann constant, T is the temperature in Kelvin, N_A is Avogadro's number, e is the elementary charge, and I is the ionic strength of the electrolyte in units of mole/m³.

For my experimental conditions, the Debye length is calculated to be $\lambda_D=13$ and $\lambda_D=0.6$ nm for without (20 mM acetic acid; ionic strength of 0.6 mM) and with salt (279 mM ionic strength) samples, respectively. The average spacing between collagens of 46 nm (concentration of 5 mg/ml) is much larger than the Debye length. Therefore, at this pH and collagen concentration, electrostatic interactions are not predicted to influence elasticity, as observed. Slight effects of salt observed at low frequency, which lower G'

and G''_R closer to Maxwellian scaling, may be due to the repression of electrostatic interactions between fluctuating chains when salt is added.

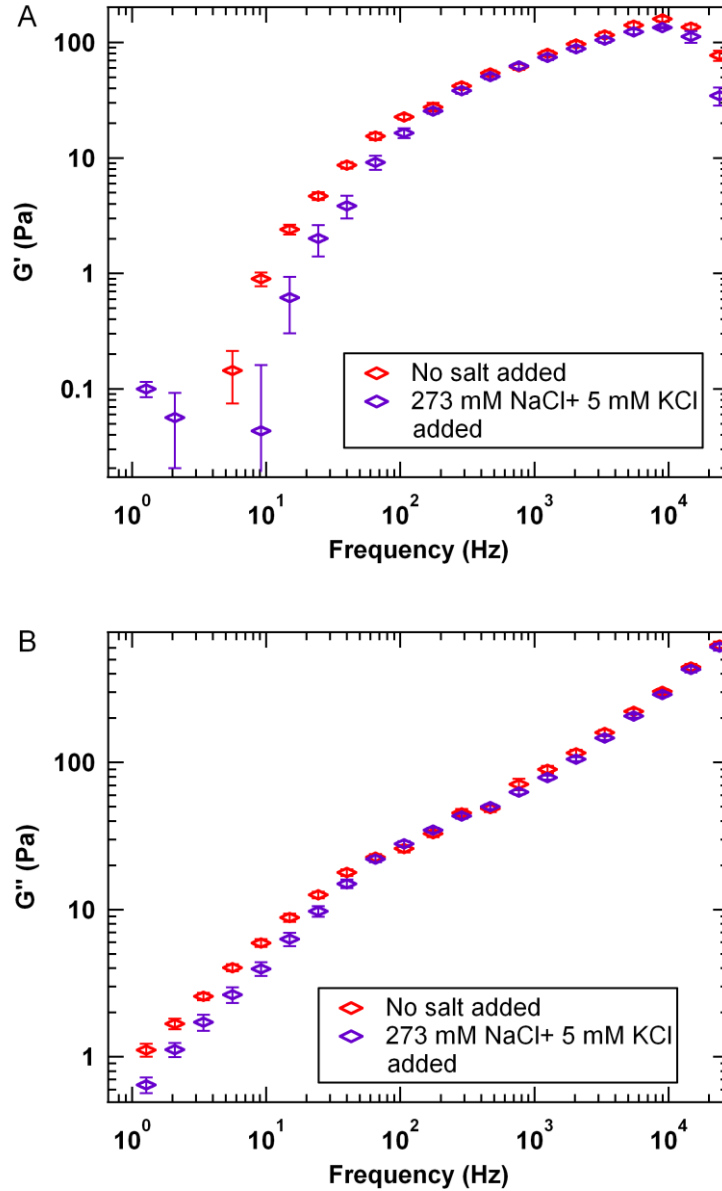


Figure 5.9. Effect of addition of salt on viscoelasticity of collagen solutions. Comparison of (A) elastic and (B) viscous moduli for collagen solutions of 5 mg/ml. Note that in these measurements telopeptides removed collagen was used.

5.6. Effect of Molecular Modification (removal of telopeptides)

Finally, I investigated the mechanical contributions arising from a specific region of the collagen protein: its non-helical ends (telopeptides). As discussed in Chapter 3, it has been shown that telopeptides play an important role in fibril formation. Their removal slows down the kinetics of fibril assembly and changes the final fibril morphology. However, it is not clear whether these short telopeptides confer mechanical properties to collagen solutions. To address this question, the shear moduli of solutions of collagen with and without telopeptides were measured at identical concentration. This work was performed in collaboration with Dr. Tuba Altindal, a postdoctoral researcher in the lab.

The removal of telopeptides is usually achieved by pepsin, which is a protease (protein digesting enzyme). Pepsin specifically digests the non-helical regions located at the two ends of the collagen molecule (telopeptides) and leaves the triple-helical part intact [182,183]. The digestive activity of pepsin is greatest at acidic pH, in correspondence with the fact that it is released by the chief cells in the stomach and degrades food proteins into peptides [184].

Here, in order to remove the telopeptides, a collagen solution of 2 mg/ml concentration was prepared by dilution of the stock solution (5 mg/ml) into 20 mM acetic acid at pH 2; lowered by addition of HCl. At this pH, pepsin is more active. Subsequently, half of the sample was treated with pepsin while the other half was treated identically in the absence of pepsin. Pepsin treatment was done in two doses (modified from the protocol in [182]): initially 1.6 mg/ml, with an additional 1.2 mg/ml added after 24 hours and incubated for another 3 days, with incubations of collagen at 4°C (final collagen concentration of 1.5 mg/ml). In separate experiments, collagen samples treated under the same conditions were analysed by SDS-PAGE to verify removal of telopeptides (Figure 5.10).

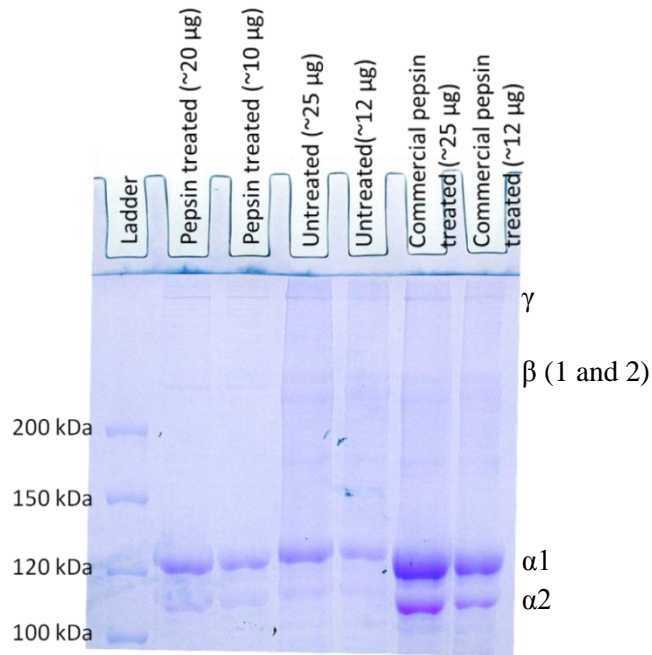


Figure 5.10. Comparison of the collagen-related bands for untreated (including telopeptides), pepsin-treated, and commercially available pepsin-treated collagen solutions analysed by SDS-PAGE. Removal of telopeptides results in a shift of collagen bands to lower molecular weights. For each sample, two different amounts of collagen were tested to verify that the shift in the position of collagen band was not related to the amount of collagen loaded in the gel.

Figure 5.11 shows the shear moduli measured for samples with and without telopeptides. The removal of telopeptides significantly alters the elastic modulus of collagen solutions at intermediate frequencies (~ 10 -200 Hz), while having little effect on the viscous modulus. This may result from an increased stability of (still transient) interactions between collagen chains in solution when telopeptides are present. In order to confirm that these changes are due to the telopeptide removal, rather than the presence of pepsin in solution, in a separate experiment, the treated collagen was salt-precipitated and re-suspended [183], here in 20 mM acetic acid (pH 3.3). In the salt precipitation process, collagen is separated from pepsin and small digested pieces of telopeptides. While one cannot be sure that the concentration of the resultant purified collagen is the same as the other samples, the shape and overlap of this curve with the pepsin-containing sample at all but the lowest frequencies for $G'(f)$ suggests that the concentrations are very similar, as suggested also by ELISA measurements of its concentration (1.2 ± 0.5 mg/ml). Furthermore, this demonstrates that the decrease in $G'(f)$ is not caused by the presence of pepsin in solution. It is also worth noting that at

this pH range (pH 2 and 3.3), the shear moduli are pH-independent. This is perhaps due to the fact that expected charge distribution of collagen does not change significantly over this range.

These results suggest that telopeptides strengthen interactions between collagen molecules on the tens of millisecond timescale. Transient binding of telopeptides to other collagen triple helices has been hypothesized to facilitate fibril formation [182,185]. While these measurements are performed in acidic pH to inhibit fibril formation, these results demonstrate evidence of this transient interaction through the increased elasticity of solutions of collagen molecules, which may contribute to the faster kinetics of fibril formation by collagen with intact telopeptides at neutral pH.

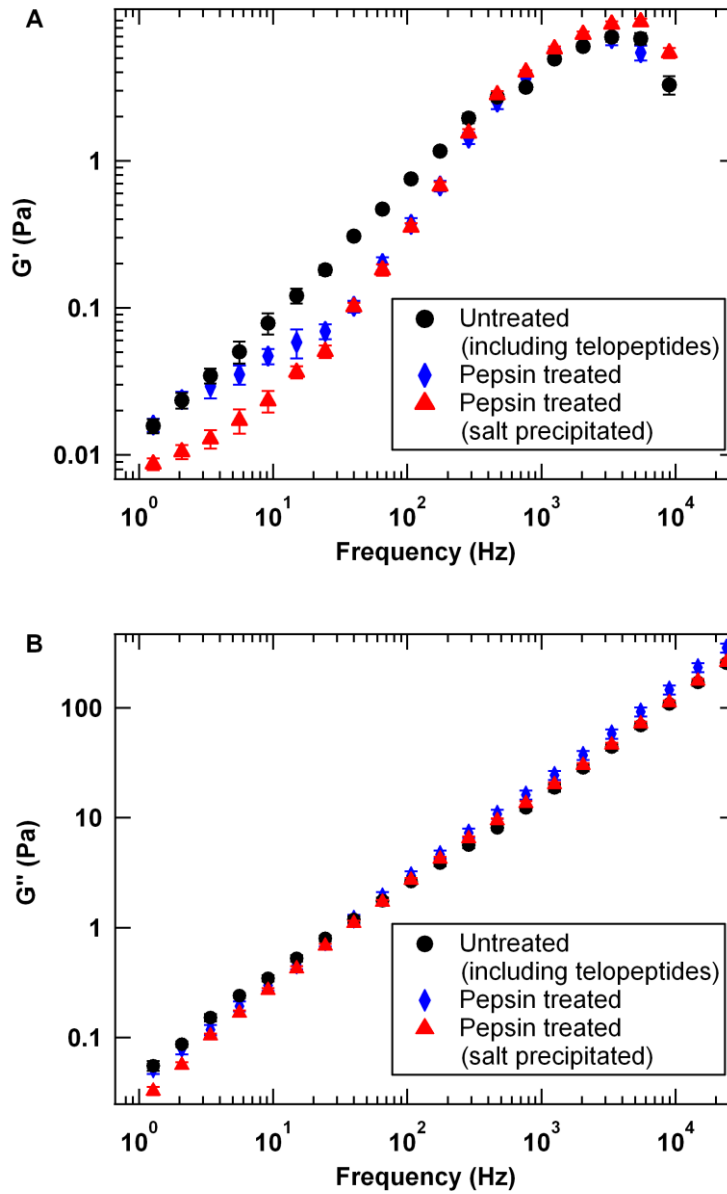


Figure 5.11. (A) Elastic and (B) viscous moduli for 1.5 mg/ml collagen with intact telopeptides (untreated, pH 2); collagen with telopeptides removed and digested telopeptides still in solution (pepsin-treated, pH 2); and collagen with telopeptides removed by pepsin and purified away from pepsin and telopeptide fragments (pepsin-treated, salt precipitated, pH 3.3). Values presented are averages over 6 measurements in each sample and error bars are the standard error of the mean.

5.7. Summary

In this chapter, I presented micromechanical properties of collagen solutions in conditions that do not lead to self-assembly (acidic pH). Concentration-dependent viscoelasticity was observed, suggesting that elasticity at the highest concentrations of my study is due to interactions between collagen molecules. Higher frequencies and/or more dilute samples could help to resolve the remaining uncertainty on collagen's flexibility. By probing the response using beads with different sizes and surface chemistries and by significantly increasing the ionic strength of the acidic solution, no significant change in the magnitudes of the moduli was found, demonstrating that electrostatic depletion does not significantly contribute to these results. However, molecular modifications (removal of telopeptides) significantly lower elasticity of collagen solutions on the tens of millisecond timescale (frequencies from ~10-100 Hz). This study shows that microrheology can serve as a probe for contributors to intermolecular interactions and their timescales.

Chapter 6.

Networks of Collagen Fibrils

In this Chapter, the utility of optical tweezers to probe collagen's mechanical response throughout its hierarchical assembly is demonstrated. By determining the local complex shear modulus, it is found that mechanical heterogeneity at the microscale appears during early phases of fibrillar growth, developing further during this growth phase. This is in contrast to the homogenous response observed for collagens in solution (Chapter 5).

In Section 6.2, the viscoelasticity of collagen gels resulting from self-assembly into fibrils at neutral pH is probed. Then in the following section (6.3), I discuss how our measurements show that the development of viscoelasticity correlates with the kinetics of fibril formation in solution. Previous dynamical measurements of rheological changes occurring during protein or peptide self-assembly have been limited to frequencies <100 Hz [186–191]; our optical-tweezers-based probe system extends the range of frequencies spanning from 1 Hz to > 1 kHz, thus enabling study of interactions in more dilute systems and for more transient interactions. The results obtained in this section suggest that it is during the growth phase of fibril formation that mechanical heterogeneity develops on the microscale. Finally in Section 6.4, I complement these data with measurements on gelatin, which is formed when collagen is first denatured in solution and then allowed to cool into a gel, forming a distinct supramolecular structure with significantly different microrheological properties.

Sections 6.2 and 6.3 for the viscoelastic properties and models of collagen systems after and during fibril formation and Section 6.4 for the viscoelastic properties of gelatin gels were adapted from our publications [162] and [192], respectively.

6.1. Experimental and Analysis Details

For microrheological measurements probing collagen fibril assembly and gels, carboxylate-functionalized polystyrene microspheres (diameter 2.10 μm ; Spherotech) were added to collagen solutions at a final concentration of $\sim 5 \times 10^{-4}$ % w/v. Fibril formation was induced inside the optical tweezers sample chamber at room temperature ($\sim 21^\circ\text{C}$) or 30°C by adding “fibril formation buffer” to 5 mg/ml acid-soluble collagen (intact telopeptides) to attain a final concentration of 0.5 or 1 mg/ml collagen. Detailed information on the salt concentrations can be found in Section 3.5. Because fibril formation was induced in the presence of the beads, control turbidity experiments were conducted and showed that this dilute concentration of beads did not affect the kinetics of fibril assembly (Figure 6.1), in contrast with observations at higher bead concentrations [193,194].

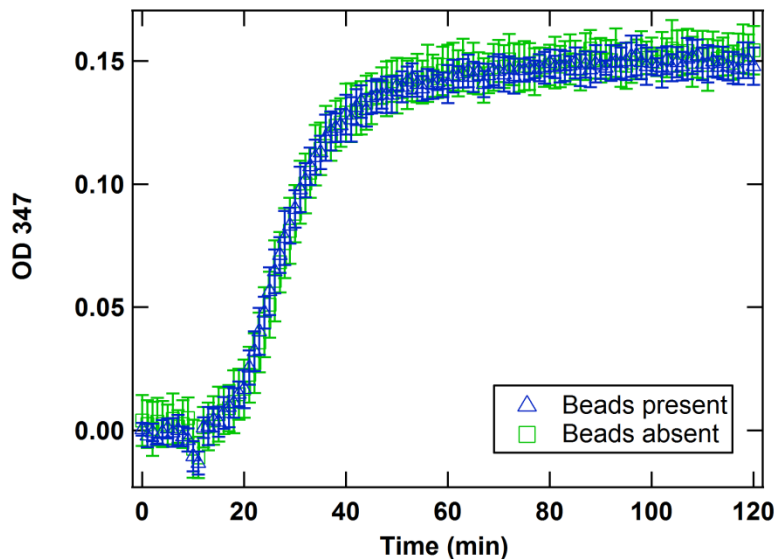


Figure 6.1. Presence of beads at low concentration ($\sim 5 \times 10^{-4}$ % w/v) does not affect the kinetics of fibril formation. Figure shows the kinetics of fibril formation with 0.5 mg/ml collagen at $\sim 25^\circ\text{C}$ (measured via the plate reader).

When probing dynamical changes in local viscoelasticity during fibril assembly, the chamber was immediately mounted and aligned in the optical tweezers instrument. The time required for this mounting, alignment and stabilization of the instrument resulted in a delay time of approximately 20 minutes before microrheology measurements on fibril growth could be performed. During long-duration measurements

monitoring collagen self-assembly, the laser beam was “blinked” off and on between measurements, so as to minimize radiation exposure and possible heating and reduce the likelihood of trapping growing fibrils in the optical trap, while attempting to maintain the same probe particle for multiple consecutive measurements.

For microrheological measurements on gelatin, samples were formed from two different sources and results were compared. In one type, pepsin-soluble type I collagen (telopeptides removed) was used as a source to form gelatin by heating a sample of the stock solution (in 20 mM acetic acid) to 80°C, then cooling to room temperature in the sample chamber. In another experiment, gelatin was prepared from commercial gelatin powder (Knox; bloom strength 225) by first softening with cold distilled water, then adding an equal volume of boiling water to dissolve and achieve the final desired concentration. Microspheres were added to the warm sample, which was pipetted into a heated sample chamber, sealed, and allowed to sit at room temperature for >24 hours before measurement.

For the analyses of the experiments presented in this chapter, the assumption of little elasticity at low frequencies is not generally valid, in contrast to that for collagen solutions (Chapter 5). To correct for contributions from the trap, I therefore subtracted from each $G'_{measured}$ the average G'_{trap} determined for these beads in water ($G'_{trap} = 3.9 \pm 0.7 Pa$ for the laser power of 100 mW used in these experiments). The variability in G'_{trap} likely arises from the dispersion of bead sizes in our sample.

6.2. Microrheology of Collagen Gels

Microscale inhomogeneity within collagen gels is clearly evident in our microrheology measurements. An example of different x-y trajectories of two beads at two different locations of an identical collagen gel are shown in Figure 6.2. The motion of the bead in Figure 6.2(A) is more constrained (higher local elastic modulus), while the bead in Figure 6.2(B) exhibits substantial anisotropy of its motion, where bead’s motion is elongated in one direction and suppressed in other direction. My microrheology

analyses, however, are only performed in one dimension because in these experiments, my goal was to study heterogeneity, rather than anisotropy of the materials.

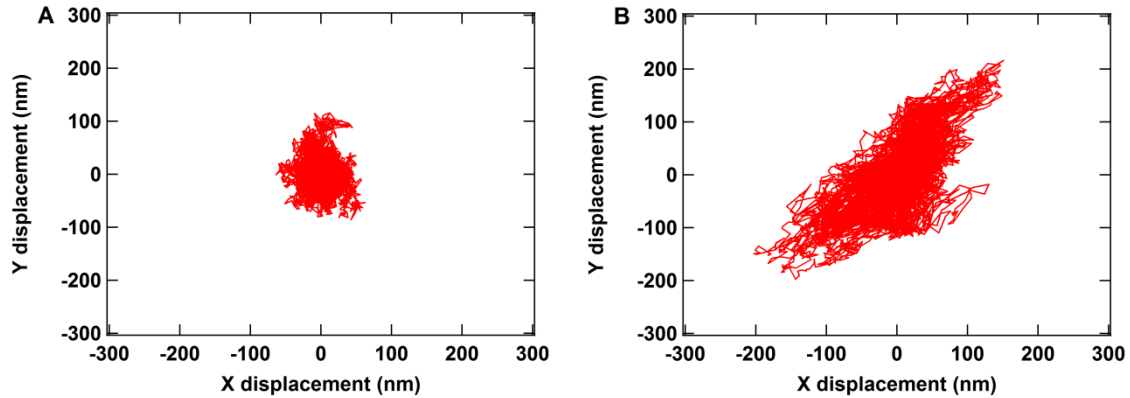


Figure 6.2. Heterogeneity of properties is observed within a collagen gel sample prepared from 0.5 mg/ml collagen at room temperature. Plots here show the x-y trajectories from two different beads (different locations) over ~9 seconds. In these measurements, the beads were not optically trapped.

This heterogeneity will be explored through the complex shear modulus. Figure 6.3 shows representative measured elastic and viscous moduli at different locations in collagen gels, formed from 0.5 mg/ml collagen at pH 6.9 at room temperature (21°C). As can be seen, the moduli (as measured using 2 μm -diameter probe particles) vary by more than an order of magnitude at different locations within the gel. This heterogeneity in viscoelastic properties is also shown in Figure 6.4 for a collagen gel formed from 1 mg/ml collagen at pH 6.9 at 30°C.

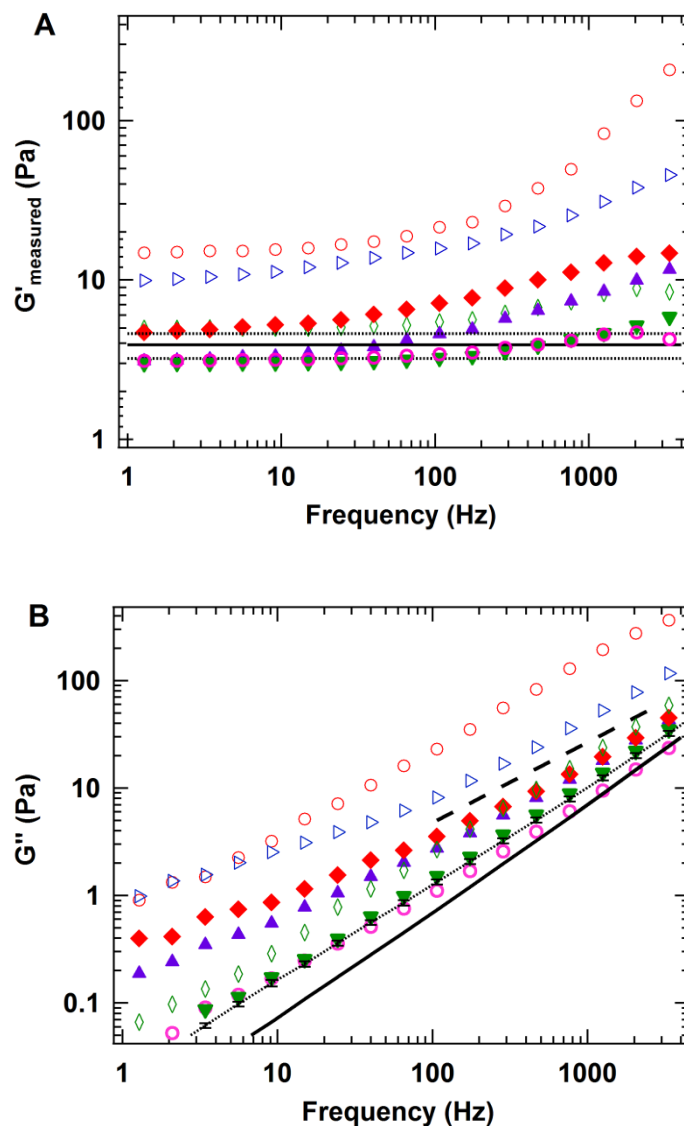


Figure 6.3. Measured (A) elastic and (B) viscous moduli at different locations in collagen fibrillar gels (prepared from 0.5 mg/ml collagen at 21°C and pH=6.9). Note the large variation in properties at different positions (within either the same gel or gels prepared under identical conditions). The solid and dashed lines in (A) represent the independently measured average elastic modulus of the trap and its standard deviation ($G'_{trap} = 3.9 \pm 0.7 Pa$) for the same laser power and bead size ($N=28$). In (B), the dashed line at high frequency is plotted to illustrate power-law scaling of $\frac{3}{4}$. For comparison, the solid and dotted lines plot the measured viscous modulus of water and of 0.5 mg/ml collagen in acidic solution, respectively. Gel data shown here include the maximal and minimal moduli measured in all of my experiments.

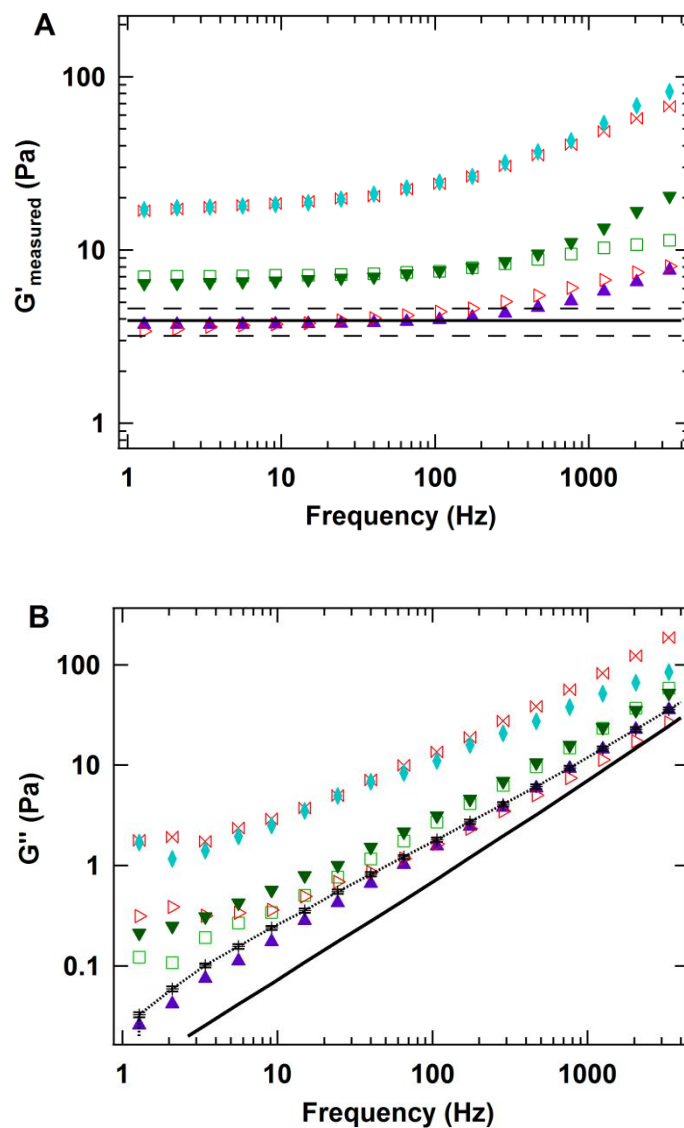


Figure 6.4. Measured (A) elastic and (B) viscous moduli at different locations in a collagen fibrillar matrix formed from 1 mg/ml collagen and prepared at 30°C and pH=6.9. The solid and dotted lines plot the measured viscous moduli of water and of 1 mg/ml collagen in acidic solution, respectively. Overall, the heterogeneity of viscoelastic properties within the gel does not change substantially with this different collagen concentration and formation temperature. Measurements were performed at room temperature.

It is important to note that the values plotted in Figure 6.3(A) and 6.4(A) for G' of these collagen gels are the measured values, which include a contribution of $G'_{\text{trap}} = 3.9 \pm 0.7 \text{ Pa}$ (indicated by the solid and dashed lines) that should be subtracted

from $G'_{measured}$ in order to extract the true elastic modulus of the fibrillar gel. The range of trap elastic moduli (most likely caused by the polydispersity of bead size) means that G'_{gel} cannot be determined accurately for each measurement. For regions of the gel with low elastic moduli, the uncertainty in trap stiffness leads to a significant range of possible slopes of $\log G'_{gel}$ vs. $\log f$, an issue that is not problematic for larger moduli (e.g. at higher frequencies) (Figure 6.5). Symbols in Figure 6.5 indicate the values obtained by subtracting the mean trap modulus from $G'_{measured}$, while the shaded regions for diamonds and error bars for circles represent the values obtained when considering the standard deviation of the elastic modulus of the trap ($G'_{trap} = 3.9 \pm 0.7 Pa$). The power-law scaling in regions of the gel with $G'_{gel} > G'_{trap}$ is affected very little by this uncertainty (upper curve), while the power-law scaling in regions of low elastic modulus is highly dependent on the specific value of G'_{trap} used (lower curve, particularly at low frequency where the slopes from the upper and lower bounds of G'_{gel} are clearly different). Thus, I do not attempt to quantitatively analyse the low-frequency scaling of the elastic response of the collagen gels. Nonetheless, it remains clear that there is a strikingly broad range of both elastic and viscous moduli within the 0.5 mg/ml fibrillar collagen gel matrix (at $f \approx 40$ Hz: $0 \leq G' \leq 13 Pa$, $0.5 \leq G'' \leq 13 Pa$; and at $f \approx 2000$ Hz: $0.4 \leq G' \leq 128 Pa$, $14 \leq G'' \leq 270 Pa$; $N=40$). The moduli obtained here span the values from bulk rheology measurements on collagen gels of comparable concentration at the appropriate comparison frequency [187,195–197]. For the more gel-like regions of the sample, G' dominates over G'' at low frequencies (confirming the elastic nature of these gels), while at high frequencies, G'' is larger.

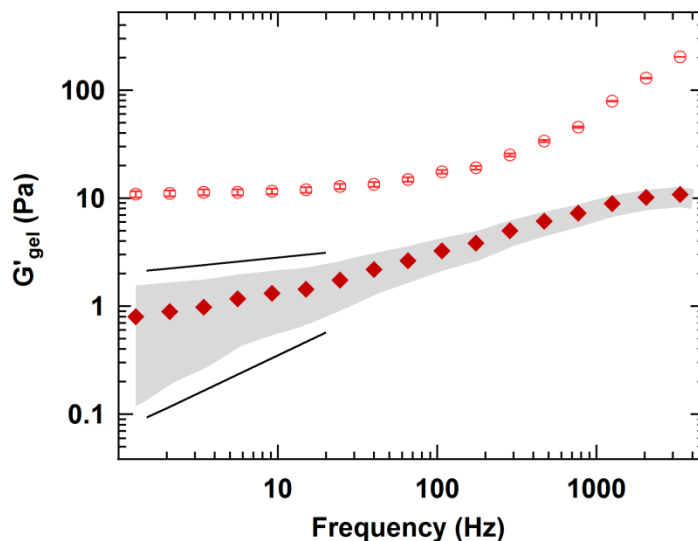


Figure 6.5. Uncertainties in trap modulus significantly affect observed power-law scaling. Here, two elastic moduli measured for collagen gels, G'_{gel} , are obtained by subtracting G'_{trap} from the measured values of $G'_{measured}$ (same symbols as used in Figure 6.3). See text for details on the shading.

Variation of microscale viscoelastic properties within formed collagen gels, ranging from solvent-like to elastic response, has been noted previously by others [30,31,198]. These previous microrheology studies on collagen gels used pepsin-solubilized collagen, which lacks its telopeptide ends and has a reduced ability to form fibrils [199]. Results presented in this chapter, on acid-solubilized collagen, demonstrate that this microscale variation in response applies also to fibrillar gels formed from full-length collagen (*i.e.*, including the telopeptide ends). In addition, the current work significantly extends the frequency range of response probed in these systems, which had previously been studied only up to ~ 10 Hz with passive microrheology [198] or at a specific frequency of ~ 5 Hz [31] or 100 Hz [30] with active microrheology. As a result, our results show not only the range of collagen gel moduli experienced by a microsphere at one frequency but also the variation in power-law scaling both of G' and of G'' at different regions within a gel (e.g. Figures 6.3 - 6.5). Such variation in scaling was not detected in the lower frequency measurements of [198], where G' appeared to be frequency-independent.

Measurements in regions of higher elasticity demonstrate a clear plateau of G' versus frequency which extends to frequencies at least as low as 1 Hz (Figures 6.3 and

6.4). Because in our measurements no crosslinking agents are used (similar to most other studies of collagen gels [195]), the interactions between fibrils generating gel-like behavior must be transient, resulting from entanglement and/or biochemical and electrostatic interactions rather than from permanent covalent crosslinks between segments of different fibrils. At sufficiently long times (low frequencies), the plateau in G' should turn over into the terminal regime [62].

At higher frequencies, a broad range of frequency-dependent power-law scaling of G' is observed (e.g. Figure 6.5), which at the highest frequencies in our measurements ranges from $\sim 1/4$ for regions of lower elasticity to $\sim 3/4$ for regions of higher elasticity. For G'' , the high-frequency scaling ranges from $\sim 3/4$ to \sim linear, as seen in Figure 6.3(B), where the dashed line represents a scaling of $f^{3/4}$. A similar frequency-dependent scaling exponent of 0.70 for G' and G'' was found in the growth of collagen fibrillar gels analysed using percolation theory [194]. A $3/4$ scaling is expected for semiflexible filaments when individual filament relaxation dominates the response. It is important to note that in contrast with the results discussed in Chapter 5, here, the semiflexible filaments would be fibrillar collagen (diameters ~ 200 nm; Figure 3.6) rather than single collagen triple helices (diameter ~ 2 nm). While fibrillar type I collagen can reach tens of μm in contour length, for gels, the relevant contour length, particularly at these high frequencies, is the distance between entanglements rather than the full contour length. For example, gels made from 1 mg/ml collagen have an average filament length between nodes of the network of $2.0 \mu\text{m}$ [200].

Work by Piechocka and colleagues has found that collagen gels undergo non-affine deformation, precluding detailed quantitative analysis [187]. Nonetheless, a question that arises is what contributes to the measured viscoelastic response for the wide range of moduli measured here. As described above, the “struts” in the collagen gel are fibrils, which individually have elastic moduli orders of magnitude higher than the shear elastic moduli of our gels [201]. Our lower measured values result from the very low strains imposed by this passive microrheology technique [202]. Between these struts are pores whose typical size is larger than our $2 \mu\text{m}$ probe particles [196,197], although there is a broad distribution of sizes that extends down to this particle size [196]. Using probe microspheres of a size similar to ours in active microrheology experiments,

Latinovic *et al.* specifically probed sparse regions of a 2 mg/ml collagen gel and found no detectable elasticity at 100 Hz [30]. Their values for G'' at 100 Hz in these regions were moderately larger than values measured in their control solvent, although similar within error. They interpreted this to mean that the sparse regions of their gel were completely depleted of molecular collagen, *i.e.*, that fibrillar gel formation had gone to completion. The interpretation of our results, from passive microrheology measurements on 0.5 mg/ml gels over a broad frequency range, is less clear cut. As seen in Figure 6.3, which shows representative frequency-dependent moduli (including the weakest modulus measured in our collagen gels), all of the G' curves show some frequency dependence, especially at high frequency. Were the response due only to the optical trap, G' would not increase with frequency. For G'' as well, the measurements that most closely approach solvent response, shown as a solid line in Figure 6.3(B), do so at high frequency but deviate significantly at low frequency, tending toward the values measured for 0.5 mg/ml collagen molecules in acidic conditions (dotted line in Figure 6.3(B)). (The complex shear modulus of molecular collagen solutions at neutral pH and high ionic strength likely differs from that in acidic conditions, but it was not possible for us to measure their response at ambient temperature due to their self-assembly into fibrils [48].) Because G' and G'' are determined over a broad frequency range, the changes in curvatures of these moduli (and not just their values at one given frequency, which have a considerable uncertainty for small G') indicate that the local response measured in this gel does not range simply from that of fully formed fibrils down to fully depleted solvent. The presence of elasticity and viscosity above that of the solvent in our measurements could potentially result from occasional interactions with nearby fibrils, or alternatively from unincorporated molecular collagen in void regions of the gel. The latter seems an unlikely explanation, since collagen has been found to be almost completely incorporated into gels at this concentration and temperature [39]. The significantly larger number of probed locations in our measurements ($N=47$ independent measurements on gels) compared with the active microrheology measurements of Latinovic *et al.* suggests that our probe particles do not often encounter a region of pure solvent. Experiments utilizing smaller probe particles and/or particles specifically bound to collagen fibrils would move toward measurements more comparable to the size of focal adhesions or to the sensing of fibril-specific viscoelastic response [201–203].

6.3. Microrheology During Fibril Formation

I next aimed to investigate viscoelastic properties during the process of assembly from molecules into fibrils. The development of viscoelasticity is then correlated with the self-assembly of collagen into higher-order structures as a function of time (turbidity measurements). As it is explained in Chapter 3, turbidity is sensitive to the size of particles in solution, measuring the attenuation of transmitted light via scattering in a sample and is the conventional means by which the kinetics of collagen self-assembly into fibrils is followed [39,124]. The turbidity measurements were performed on sample volumes of 100 μl (pathlength 1 cm) and thus were insensitive to μm -scale differences in solution composition. In contrast, the complex shear moduli from microrheology measurements reflect the environment around each μm -sized probe particle.

Given the results from turbidity measurements (Figure 3.5), a collagen concentration of 0.5 mg/ml was chosen for the microrheology measurements, enabling me to monitor mechanical changes at least from the early stages of fibril growth. Although lower collagen concentrations would further decrease the rate of assembly, allowing me to probe earlier stages of fibril assembly, the anticipated lower values of elastic and viscous moduli [204] would create further challenges for determination of the elastic modulus. As discussed in Chapter 3, besides concentration, molecular composition and solution conditions such as pH, ionic strength and temperature affect kinetics of collagen self-assembly [39,124,132,140]. In the following experiments, these parameters were kept constant between turbidity measurements (red diamonds in Figure 3.5) and the following microrheology experiments.

Here, I demonstrate the ability to probe the development of broadly distributed viscoelastic properties over a wide range of frequencies during collagen fibril growth. In the measurements discussed here, elastic and viscous moduli determined from 47 independent measurements (different probe beads and locations) during the process of self-assembly are presented.

In order to investigate development of mechanical heterogeneity, the individual values for elastic and viscous moduli as a function of time (after altering solution conditions to permit fibril assembly) were determined. To illustrate this development

more clearly, Figure 6.6 shows the moduli at a high frequency ($f = 2$ kHz) versus time. This high frequency was chosen for the purposes of display for two reasons. First, the modulus of 0.5 mg/ml collagen in acidic conditions (shown for representative purposes as time = 0 in Figure 6.6) is greater than the trap modulus. Second, our measurements on gels at long times (>1 hour after formation; Figure 6.3) indicated that most elastic moduli of the sample were significantly larger than G'_{trap} at this measurement frequency. Similar plots for both moduli at a lower frequency ($f = 100$ Hz) are shown in Figure 6.7.

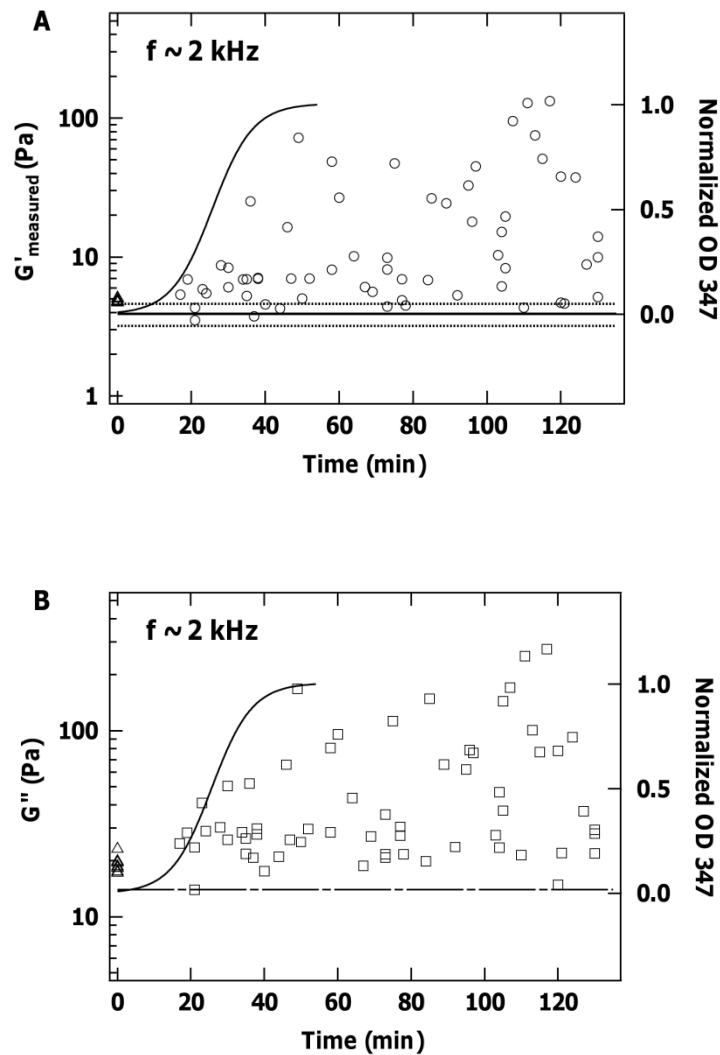


Figure 6.6. Heterogeneous microscale viscoelasticity is apparent even from the early growth phase of collagen fibril assembly. Measured (A) elastic and (B) viscous moduli at $f = 2$ kHz as a function of time during collagen self-assembly at 0.5 mg/ml (pH=6.9, 21°C). Solid and dashed lines in (A) show $G'_{\text{trap}} = 3.9 \pm 0.7$ Pa as described for Figure 6.3. The dot-dashed line in (B) plots the measured viscous modulus of water at $f = 2$ kHz. Triangles at zero time reproduce moduli measured at $f = 2$ kHz for 0.5 mg/ml collagen in acidic conditions (Figure 5.2), where assembly cannot occur. For comparison, the sigmoidal development of turbidity (Figure 3.5) is superimposed on the plot (solid line; right axis), rescaled vertically between solvent response and the maximum measured value of elastic modulus.

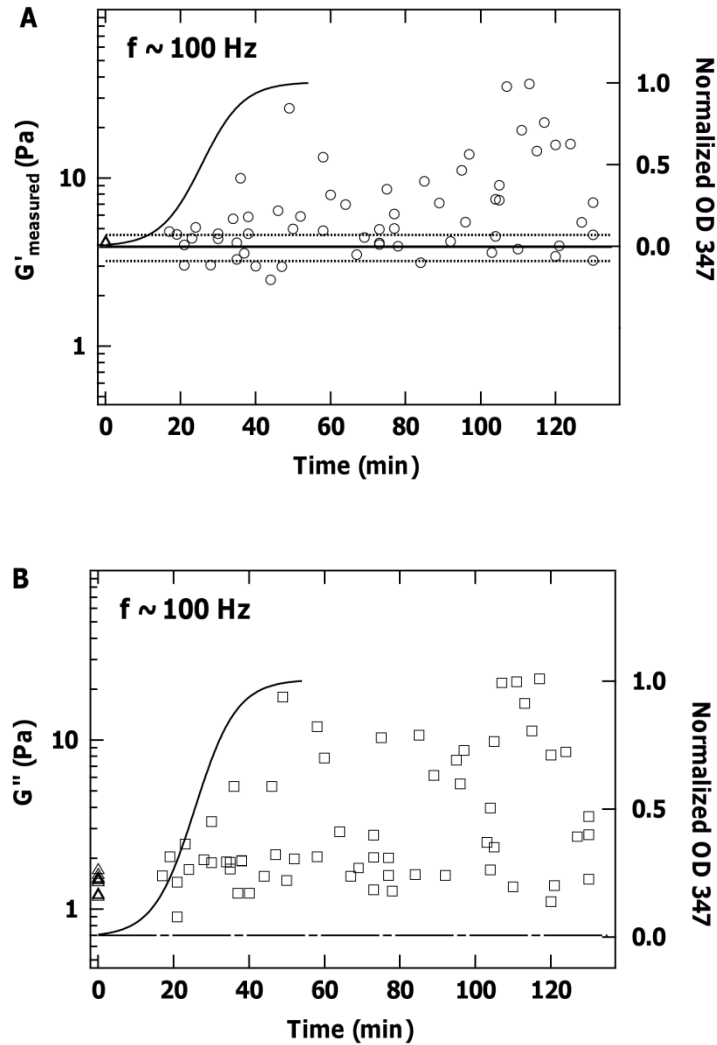


Figure 6.7. Measured (A) elastic and (B) viscous moduli from the same measurements as in Figure 6.6 but here at $f=100$ Hz.

The microrheology measurements during assembly indicate a dynamic system, in which mechanical heterogeneity is apparent even at the early stages of the growth phase. As time passes, the variation in moduli increases, reaching a plateau after ~ 50 minutes. For instance, according to Figure 6.6, at time ~ 20 minutes, G' (2 kHz) values at different locations were observed to range between that of the trap ($G'_{trap} = 3.9 \pm 0.7$ Pa) and ~ 7 Pa; whereas at longer times (e.g. ~ 50 minutes), they spanned a range between G'_{trap} and ~ 70 Pa. Similarly, development of heterogeneity was observed for G'' (2 kHz) (at $t=20$ min: $14 \leq G'' \leq 40$ Pa, while at $t=50$ min: $25 \leq G'' \leq 160$ Pa).

In Figures 6.6 and 6.7, triangles at zero time reproduce moduli (at $f = 2$ kHz and $f = 100$ Hz, respectively) of 0.5 mg/ml collagen in acidic conditions (Figure 5.2), where fibril formation cannot proceed. Although ten different probe particles (different locations) were included for this zero-time condition, as stated in Chapter 5 their lack of significant dispersion demonstrates that the collagen solutions are homogenous prior to the initiation of fibril formation.

The time-dependent measurements show that heterogeneity exists at timescales at least as early as 20 minutes after the initiation of assembly, and that it appears to develop further with time (Figures 6.6 and 6.7). Active microrheology measurements similarly have found an increase in G' and G'' with time, as collagen fibrils grow and the gel develops [30]. The range of moduli that remains long after assembly has completed (based on the plateau in the turbidity curve) is evidence of the variety of local environments within this gel (as described in the previous sections).

It was found to be challenging to monitor the development of viscoelasticity at any given location as a function of time. Interestingly, during fibril assembly, beads were frequently observed to be forced out of the optical trap, presumably by growing fibrils. From the trap stiffness and bead size of our measurements, this force is conservatively estimated as $F > 50$ pN. While this mechanism remains to be investigated, self-assembly of other proteins, such as actin and tubulin, into polar filaments is key to biologically critical force-generating processes [205,206]. Further challenges to following the local development of viscoelasticity resulted from our use of a “blinking” optical trap during these long duration measurements (see Section 6.1), resulting in loss of beads due to diffusion or fibril growth during the times when the laser was off. Occasionally, it was possible to monitor the local environment over extended periods of time, in one example observing a significant increase in G' and G'' well beyond an hour and in another finding no evolution of these values with time (Figure 6.8). In the former case, our measurements suggest that elasticity and viscosity may continue to evolve locally within a gel, even when these properties have reached their maximum values elsewhere in the sample and turbidity measurements indicate that the gel has fully assembled. Further experiments would also help to elucidate whether local moduli can both increase and decrease with time, or whether for example the transient decrease in moduli around 100 minutes is due to drift of the sample chamber.

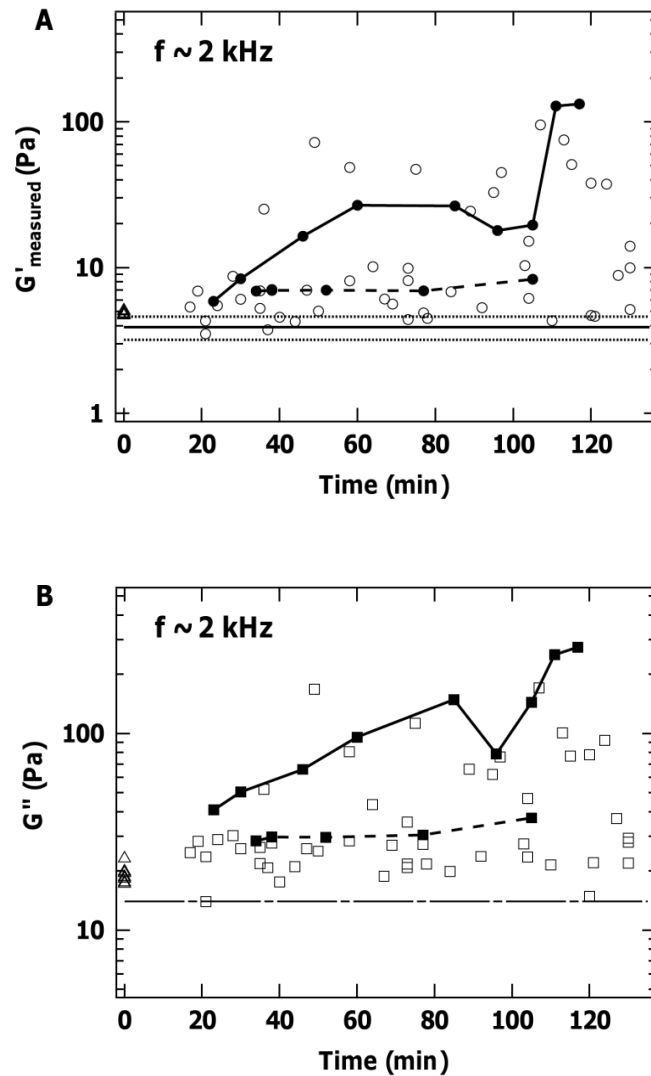


Figure 6.8. Measured (A) elastic and (B) viscous moduli in an assembling collagen fibrillar matrix, reproduced from Figure 6.6. In rare circumstances, it was possible to retain a given probe particle for measurements at multiple times. These results are indicated by filled symbols, and are connected by lines to guide the eye. A significant evolution in viscoelastic properties is seen at one location (solid line), while in another location, no significant change is observed (dotted line).

In order to interpret the correlations between our microrheology results and turbidity measurements, the percolation model discussed in [194] is followed. Forgacs *et al.* have shown that collagen fibrillar gel assembly is initiated by random nucleation of filaments that grow in the form of clusters [194]. These randomly distributed clusters grow both longitudinally and laterally during the growth phase [191], which in our measurements results in a rapid increase in turbidity. Once these clusters grow sufficiently large, they become interconnected. In microrheology measurements, while the complex shear modulus is a function of the local environment about a microsphere, its magnitude, particularly at lower frequencies, is strongly affected by interactions within a larger network. Thus, as time evolves, we expect to see a transition from the low viscoelasticity of the isolated molecules in solution, through a variable range of properties that reflects whether measurements are performed close to or far from isolated clusters, to finally locally probing the properties of the interconnected matrix. In Figures 6.6 and 6.7, the normalized turbidity curve is superimposed on the time-dependent measurements of complex shear moduli. As can be seen, the turbidity appears to form an envelope under which the shear moduli develop. By ~1 hour after initiation of fibril formation, both turbidity and the maximum measured elastic and viscous moduli appear to plateau, although as mentioned above, the moduli may continue to develop locally. For all times measured, there remains great dispersion among values of both G' and G'' reinforcing the concept of a mechanically heterogeneous gel at the microscale. Future microrheology measurements during the nucleation and onset of collagen fibril growth phases would help to elucidate whether isolated regions of higher viscoelasticity are present in these early stages of self-assembly, as would be predicted for sparsely distributed clusters within the percolation model.

Further measurements would also be needed to determine whether isolated collagen gels can dynamically reorganize at the microscale (e.g. Figure 6.8), as is seen in response to applied stress [195], and to assess more quantitatively the percolation mechanism in the context of turbidity and microrheology measurements. Although correlations between structure and mechanics during the formation of collagen gels have been probed by combining rheology and imaging [30,191,194,197], these have not assayed the associated development of turbidity of the system. A comparison with

turbidity is useful given its prevalence in measuring the effects of molecular conditions such as collagen sequence and solution pH on fibril formation [39,124,132,140].

6.4. Microrheology of Gelatin

Finally, in this section the viscoelastic properties of gelatin, an alternative molecular arrangement of collagen chains, are investigated. Gelatin is formed by heat denaturation of collagen followed by cooling. The thermal melting transition of collagen is irreversible [207]. This leads to formation of a heterogeneous mixture of individual α -chains of collagen, with short triple-helical entwinements of the chains which create nodes in the gel network [207]. The aim of these microrheological studies on gelatin is to understand how a completely different organization of collagen modifies its mechanical properties. This work was performed in collaboration with Norman Lam, undergraduate researcher in the lab.

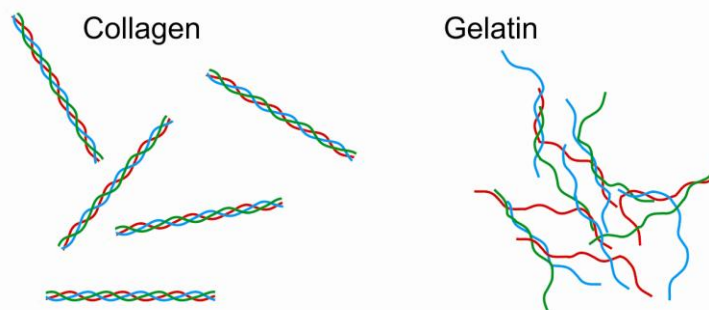


Figure 6.9. This schematic compares the structural organizations of collagen molecules and gelatin [192]. The latter includes individual α -chains of collagen and regions of short triple-helical entwinements of the chains.

Figure 6.10 shows the complex shear moduli of two types of gelatin at 5 mg/ml. One was directly prepared by denaturing collagen and the other one prepared from commercial powdered gelatin as described in Section 6.1. Both gelatin samples show similar values for elastic and viscous moduli, although these are significantly below those of similar concentrations of triple-helical collagen molecules in solution, as can be seen by comparing Figure 6.10 with Figure 5.2, and with those of collagen fibrillar gels formed at the lower concentration of 1 mg/ml (compare Figure 6.10 with Figure 6.4). As

in Chapter 5, the lowest frequency value of $G'_{measured}(f)$ is subtracted from $G'(f)$ for these concentrations of gelatin. Overall, these gelatin samples do not exhibit any elasticity at low frequency, suggesting that an elastic gel structure cannot be sensed by micron-scale probe particles within these samples. This observation is supported by the fact that a 5 mg/ml concentration is close to the critical concentration for gelatin [207].

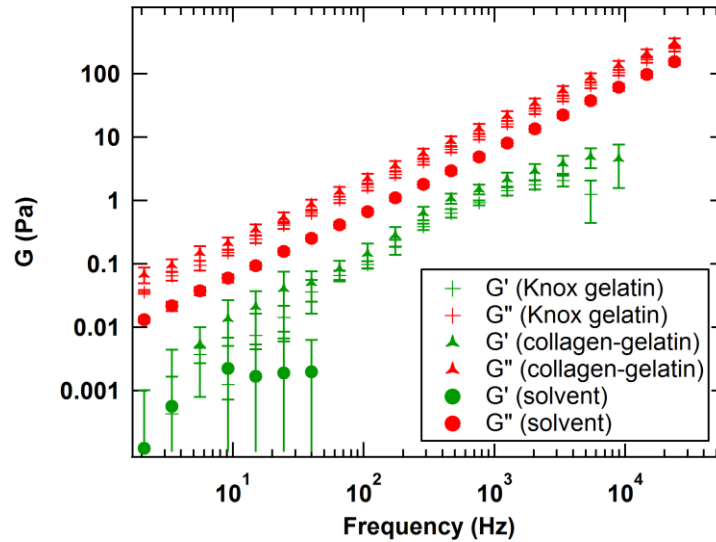


Figure 6.10. Elastic and viscous moduli for 5 mg/ml collagen-gelatin and commercial gelatin (Knox gelatin) are identical within error. Although they are both greater than the corresponding moduli measured in solvent (20 mM acetic acid, circle symbols) alone, they result in much lower moduli than a similar concentration of collagen molecules in solution (Figure 5.2) and fibrillar gels with lower concentrations of collagen (Figures 6.3 and 6.4). Symbols represent mean values and error bars the standard deviations, for $N=10$ beads under each experimental condition.

The lack of spatial heterogeneity of shear moduli (Figure 6.10) as indicated by the small error bars in complex shear moduli, is further evidence for the lack of a gel structure within these gelatin samples. Because it has been shown that the gelation transition is very slow in gelatin [207], it is possible that yet longer gelation times (upon cooling) may possibly lead to an increase in the viscoelastic properties.

The similarity of the viscoelastic properties of gelatin samples prepared from denatured collagen versus the Knox gelatin suggests that different preparation methods, different solvents and pH used, and different animal sources might not play a significant role at these low concentrations of gelatin.

In order to test the effect of concentration, the Knox gelatin sample was also prepared at a concentration of 14 mg/ml. Figure 6.11 shows the measured elastic and viscous moduli of this 14 mg/ml gelatin sample. Because of the strong heterogeneity observed in these samples, in contrast to the observations above for 5 mg/ml gelatin samples, the measurements for $N=10$ different beads (different locations) are not averaged but rather plotted individually. The dispersion in measured elastic modulus ranges from ~ 10 -80 Pa at low frequency, all of which are greater than that of the trap.

Comparing to the literature, the lowest concentration at which gelatin has been characterized by rheology is 47 mg/ml [208]. We repeated our measurements on this higher concentration of gelatin (50 mg/ml) but found that the range of particles' thermal motion was suppressed to such an extent that small amounts of background noise in the instrument and/or drift of the whole sample became the dominant source of measured motion of the particle. Thus, we compare our measurements at 14 mg/ml with the literature values, in which the magnitude of shear modulus of gelatin was found to be on the order of ~ 50 Pa [208]. This is on the same order of magnitude as what is found here for the lower concentration of 14 mg/ml. This similarity in the magnitude of shear modulus, despite the significant difference in concentration, might be because the measurements in Ref. [208] were bulk rheology and hence, they did not probe heterogeneity in the properties. However, in our microrheological characterization, a range of local viscoelastic properties is found for this heterogeneous system. The difference between these two types of rheological measurements is discussed more in Chapter 7.

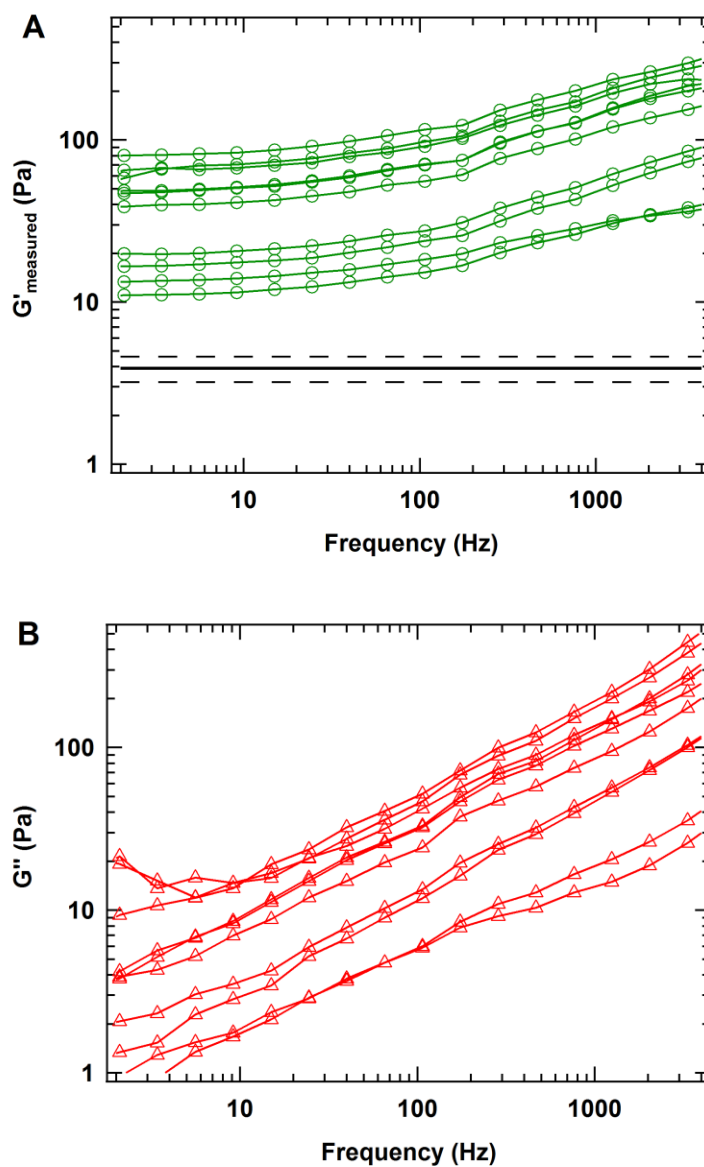


Figure 6.11. Measured (A) elastic and (B) viscous moduli of 14 mg/ml commercial gelatin (Knox gelatin) exhibit significant spatial heterogeneity as sensed by the $2.1 \mu\text{m}$ probe particles used in these experiments. Different traces represent examples of independent measurements by different beads at different locations. Solid and dashed lines in (A) show $G'_{\text{trap}} = 3.9 \pm 0.7 \text{ Pa}$ as described for Figure 6.3.

6.5. Summary

In this chapter, micromechanical properties of different supramolecular structures of collagen were presented. When collagen self-assembly was promoted, I was able to

monitor development of higher-order structure during this process via mechanical changes at the microscale. These changes exhibited significant spatial heterogeneity in response over orders of magnitude in frequency. The marked difference in both magnitude and type of power-law behavior of the complex shear modulus at different regions of the final fibrillar gel indicates that the types of interactions responsible for elasticity in these collagen matrices vary significantly on the microscale. This heterogeneity could be due to a variation in the length of collagen fibrils between entanglements, to the relative sizes of probe particles versus pore sizes, and/or to dispersion in the diameter of the fibrils [191,196,200]. It is also observed that solutions of gelatin (denatured and cooled collagen) at 5 mg/ml possess extremely low elasticity compared to same concentration of collagen molecules in solution and fibrillar gels of lower concentration (0.5 and 1 mg/ml). However, gelatin at a higher concentration (14 mg/ml) does exhibit high elasticity as well as spatial heterogeneity of viscoelastic properties.

Chapter 7.

Conclusions and Future Directions

In this thesis, I developed and applied the technique of high-bandwidth passive microrheology using optical tweezers to characterize the viscoelasticity of collagen systems from molecular solutions to fibrillar gels. The technique is based on optically trapping a micron-sized particle and tracking its thermal motion. The frequency-dependent viscoelastic properties are then obtained from the time-dependent motion of the probed particle. This optical tweezers implementation of microrheology enables the measurement of mechanical properties on the micrometer scale relevant to cells, in contrast to conventional rheology. It also probes small volumes (appropriate for assaying small amounts of sample) and allows read-out of the mechanical response at sub-millisecond timescales (bandwidths of >10 kHz), the latter a distinct advantage over video-based particle-tracking microrheology.

While the main focus of this thesis was on micromechanical investigation of different hierarchical structures of collagen, I also described biochemical assays used to verify purity of our collagen solutions, and turbidity measurements used to follow the kinetics of collagen self-assembly. The formation of well-ordered collagen fibrils was verified using electron microscopy, while to determine the size and shape of collagen at the molecular level, dynamic light scattering was used. The latter measurements revealed the sparse presence of larger structures in dilute acidic solutions of collagen, which could be removed by ultracentrifugation and were shown not to affect the microrheology results reported herein. With the data obtained here from dynamic light scattering, it was not possible to unravel the mystery of collagen's persistence length. For further experiments, using a more powerful or shorter wavelength laser in order to improve the signal-to-noise ratio of these data would be advised. With a more precise light scattering measurement, it might also be possible to monitor the self-assembly process to characterize the evolution of shape and size of collagen assemblies while

assembling into fibrillar form. This may eventually provide evidence for the structure of the intermediate state of collagen microfibrils.

In solutions of triple-helical collagen molecules, concentration-dependent viscoelasticity was observed. It was found that elasticity at the highest concentrations studied (5 mg/ml) was due to collagen molecules interacting in solution conditions that do not lead to self-assembly. It was also shown that in the collagen concentration range used here, measurements with 2- and 3- μm sized beads as well as amine- and carboxylate-functionalized beads give rise to the same measured viscoelastic properties of their surrounding medium. This suggests that entropic depletion does not play a role in these measurements. By significantly increasing the ionic strength of the acidic solution, I also found that electrostatics do not significantly contribute to the viscoelastic response observed here. Therefore, I suggest that hydrophobic interactions and/or physical entanglements of collagen molecules are responsible for the measured response. It is possible to manipulate the hydrophobic interactions by addition of biological detergents [209] and then monitor the changes in the viscoelastic response of collagen solutions.

The high-frequency measurements performed here may provide insights into collagen's flexibility using the scaling factor of the viscous modulus versus frequency at high enough frequencies. For example, scaling factors of $\frac{3}{4}$ and $\frac{2}{3}$ usually correspond to the dynamics of semiflexible chain and flexible chain, respectively. The intermediate scaling factor of 0.6 found in this work for collagen solutions at the highest concentration of 5 mg/ml suggests that reaching higher frequencies (>20 kHz) may be required. However, measurement bandwidth should not be too much higher because it has been shown that, at very short times, the probe particle's motion is affected by hydrodynamics and inertia, and so the predicted scaling is altered [210].

In my measurements, the extracted values for elastic modulus at high frequencies (>2 kHz) underestimated the true values, which arose from finite integration problem. This prevented us from studying the scaling factor for elastic modulus at these frequencies. Measurements at higher bandwidths, here too, could help with this issue. Another suggestion to overcome this problem is to mathematically resolve the high-

frequency fall-off, using approaches such as the oversampling technique suggested in [211].

I, in this thesis, also tested one possible molecular modification of collagen, removal of telopeptides. Telopeptides are believed to play a significant role in kinetics of collagen self-assembly [22,123] but little is known about their effects on intermolecular interactions. I aimed to see if removal of telopeptides alters the viscoelastic properties of collagen solutions, and hence collagen's intermolecular interactions. I found that telopeptides significantly enhance the elasticity of collagen solutions on the tens to hundreds of millisecond timescale. While telopeptides are known to play a significant role in collagen's self-assembly process, my finding is important because it demonstrates evidence of transient interactions through the enhanced elasticity of collagen solutions. One possible follow-up direction with this finding is to use short peptides of specific telopeptide sequences known to interact with specific binding sites on collagen [185]. The hypothesis is that the addition of peptides to a solution of collagen (with intact telopeptides) will block the sites that are responsible to these intermolecular interactions involving telopeptides, and hence lower its elasticity, closer to the values obtained for the telopeptide-removed collagen. If this hypothesis turns out to be true, the nature and timescale of specific interactions between telopeptides and triple-helical region are found. Otherwise, either the original assumption for specificity of the interactions between telopeptides and their neighboring molecule is not true, or the interactions responsible for higher elasticity in telopeptide-intact collagen are instead telopeptide-enhanced physical entanglement rather than specific chemical binding.

Removal of telopeptides is only one example from many possible modifications and mutations of collagen. I have shown that one would be able to characterize the dynamics and time-scales of intermolecular interactions using these microrheology measurements. Accordingly, one could start with a wild-type collagen (type I, II, etc.) and compare the viscoelastic properties with a mutated version. This type of study could address the question of whether the changes in mechanical properties of collagen fibrils, which lead to a specific disorder and hence, a disease, originate from the mechanical properties of single molecules and/or during self-assembly.

Another possible direction of study is mixing different types of collagen, for example types I and III. The association of both types in tissues leads to specific mechanical properties. For example vessel walls contain a network of collagen fibers from type III with smaller quantities of type I [212]. Studies have shown that collagen plays a significant role on the mechanical behavior of this system [213]. Stiffening of the vessel wall is one example of a health problem caused by changes in collagen that occurs with aging. Although this stiffening can lead to complex disorders such as hypertension, little is known about its mechanism [214]. With the microrheology experiments presented in this thesis work, one can study the importance of the ratio of different types of collagen as well as their chemical modifications in stiffening of the vessel walls.

In addition to probing the viscoelastic properties of collagen solutions (at the molecular level), I have monitored the development of collagen's viscoelastic response during self-assembly into higher-order structures. Significant spatial heterogeneity was observed in the viscoelastic response of fibrillar gels over a wide range of frequencies. Heterogeneities were seen in both magnitude and power-law behaviour of the elastic and viscous moduli, which is an indication of different types of interactions responsible for elasticity of collagen matrices on the microscale. The origin of heterogeneity could be variation in the size of collagen fibrils between entanglements and/or the relative size of the probe particle compared to mesh size. This latter issue is counted as an important factor in comparison of the microrheology results to those of bulk rheology. It is shown (e.g. in [120]) that when the viscoelastic medium is homogenous on and above the probed length scale, moduli measured in microrheology agree well with that of bulk measurements. However, when the probe particle is smaller than the scale of heterogeneity, microrheology corresponds only to the local viscoelastic properties and no longer agrees with the medium's bulk properties. Therefore, in some articles [77,215,216], the results obtained from microrheological characterization performed on heterogeneous medium are called effective moduli, which are not representative of bulk properties yet contain information of medium's properties sensed by the probe particle [216]. Microscale heterogeneity of mechanics observed in biological fibrillar networks are likely most relevant to the range of mechanical environments sensed about a cell on timescales relevant to regulatory mechanisms and motility.

To further study heterogeneity in collagen gels, holographic optical tweezers can be used. Using this set-up, multiple particles can be monitored at the same time; additionally, cross-correlation of the displacements of two trapped particles can be used to calculate the complex shear modulus and mechanical coupling between distal parts of the material (two-particle microrheology) [217,218]. Furthermore, the inter-particle response functions for the perpendicular and parallel directions can be used to measure the anisotropy of the system.

An important future direction for this work is to include active driving of the optically trapped particle: active microrheology. This can be done by addition of a device which can precisely steer the laser beam with a sub-millisecond response time. The acousto-optic deflector (AOD) is a powerful tool which can be used to oscillate an optical trap [102]. This takes the system out of equilibrium, which is the case for many cellular processes. Comparing the active and passive microrheology evaluations of an identical sample will result in quantifying the non-equilibrium behaviour of the system, which stems from internally generated nonthermal forces such as those generated from motor proteins.

I also observed that the growth of collagen fibrils generated sufficient force to dislodge microspheres from the optical trap. The force generation and gel properties of collagen fibrils bear similarities to biological filaments such as actin or microtubules [219], although the range of possible fibril diameters for collagen represents a distinct and potentially important control parameter for collagen's mechanical interaction with cells and guiding of cellular fate. One possible direction for this type of study using microrheology is to monitor the changes in micromechanical properties of collagen matrices during cell (e.g. cancer cell) invasion. Other than cell growth in collagen networks, there are many examples of "active networks" which can be studied with this technique such as molecular motors exerting force on cytoskeletal network (e.g. myosin activity in actin networks [220]) and proteolytic cleavage of proteins (e.g. activity of matrix metalloproteinases on collagen).

At the fibrillar level, there are many examples of molecular modifications occurring in collagen in our body, which then present as mechanical changes at the tissue level, such as changes during aging and during propagation of diseases such as

arthritis, diabetes and cardiovascular illness. Chemical cross-linking happens between constituent chains of collagen within a triple helix (intra-molecular) and between collagen triple helices (inter-molecular); this may change the mechanical properties at the molecular level, fibrillar level, or both. Microrheology provides the ability to probe these properties on different length scales, which in turn can be used to monitor development of the chemical modification. This provides a means to test the effect of chemical conditions on system's properties.

Bibliography

- [1] Discher DE, Janmey P, Wang Y-L. Tissue cells feel and respond to the stiffness of their substrate. *Science* 2005;310:1139.
- [2] Dvir T, Timko BP, Kohane DS, Langer R. Nanotechnological strategies for engineering complex tissues. *Nat Nanotechnol* 2011;6:13.
- [3] Hoffman BD, Grashoff C, Schwartz MA. Dynamic molecular processes mediate cellular mechanotransduction. *Nature* 2011;475:316.
- [4] Janmey PA, Weitz DA. Dealing with mechanics: mechanisms of force transduction in cells. *Trends Biochem Sci* 2004;29:364.
- [5] Pathak A, Kumar S. Biophysical regulation of tumor cell invasion: moving beyond matrix stiffness. *Integr Biol* 2011;3:267.
- [6] Wells RG. The role of matrix stiffness in regulating cell behavior. *Hepatology* 2008;47:1394.
- [7] Friess W. Collagen-biomaterial for drug delivery. *Eur J Pharm Biopharm* 1998;45:113.
- [8] Angele P, Kujat R, Nerlich M, Yoo J, Goldberg V, Johnstone B. Engineering of osteochondral tissue with bone marrow mesenchymal progenitor cells in a derivatized hyaluronan-gelatin composite sponge. *Tissue Eng* 1999;5:545.
- [9] Meaney Murray M, Rice K, Wright RJ, Spector M. The effect of selected growth factors on human anterior cruciate ligament cell interactions with a three-dimensional collagen-GAG scaffold. *J Orthop Res* 2003;21:238.
- [10] Eaglstein WH, Falanga V. Tissue engineering and the development of Apligraf a human skin equivalent. *Adv Wound Care* n.d.;11:1.
- [11] Burke JF, Yannas I V, Quinby WC, Bondoc CC, Jung WK. Successful use of a physiologically acceptable artificial skin in the treatment of extensive burn injury. *Ann Surg* 1981;194:413.
- [12] Pachence JM. Collagen-based devices for soft tissue repair. *J Biomed Mater Res* 1996;33:35.
- [13] Kuivaniemi H, Tromp G, Prockop DJ. Mutations in collagen genes: causes of rare and some common diseases in humans. *FASEB J* 1991;5:2052.

- [14] Myllyharju J, Kivirikko KI. Collagens and collagen-related diseases. *Ann Med* 2001;33:7.
- [15] Prockop DJ, Kivirikko KI. Collagens: molecular biology, diseases, and potentials for therapy. *Annu Rev Biochem* 1995;64:403.
- [16] Bailey AJ, Paul RG, Knott L. Mechanisms of maturation and ageing of collagen. *Mech Ageing Dev* 1998;106:1.
- [17] Burrage PS, Mix KS, Brinckerhoff CE. Matrix metalloproteinases: role in arthritis. *Front Biosci* 2006;11:529.
- [18] Gosain A, DiPietro LA. Aging and wound healing. *World J Surg* 2004;28:321.
- [19] Huebsch N, Arany PR, Mao AS, Shvartsman D, Ali OA, Bencherif SA, Rivera-Feliciano J, Mooney DJ. Harnessing traction-mediated manipulation of the cell/matrix interface to control stem-cell fate. *Nat Mater* 2010;9:518.
- [20] Collier JH, Rudra JS, Gasiorowski JZ, Jung JP. Multi-component extracellular matrices based on peptide self-assembly. *Chem Soc Rev* 2010;39:3413.
- [21] Abraham LC, Zuena E, Perez-Ramirez B, Kaplan DL. Guide to collagen characterization for biomaterial studies. *J Biomed Mater Res B Appl Biomater* 2008;87:264.
- [22] Hulmes DJ. Collagen Diversity, Synthesis, and Assembly. In: Fratzl P, editor. *Collagen Struct. Mech.*, New York: Springer; 2008, p. 15–47.
- [23] Fratzl P. Collagen: Structure and Mechanics, an Introduction. In: Fratzl P, editor. *Collagen Struct. Mech.*, New York: Springer; 2008, p. 1–13.
- [24] Buehler MJ. Nature designs tough collagen: explaining the nanostructure of collagen fibrils. *Proc Natl Acad Sci U S A* 2006;103:12285.
- [25] Sun Y-L, Luo Z-P, Fertala A, An K-N. Direct quantification of the flexibility of type I collagen monomer. *Biochem Biophys Res Commun* 2002;295:382.
- [26] Sun Y-L, Luo Z-P, Fertala A, An K-N. Stretching type II collagen with optical tweezers. *J Biomech* 2004;37:1665.
- [27] Gautieri A, Uzel S, Vesentini S, Redaelli A, Buehler MJ. Molecular and mesoscale mechanisms of osteogenesis imperfecta disease in collagen fibrils. *Biophys J* 2009;97:857.
- [28] Gautieri A, Vesentini S, Redaelli A, Buehler MJ. Single molecule effects of osteogenesis imperfecta mutations in tropocollagen protein domains. *Protein Sci* 2009;18:161.
- [29] Velegol D, Lanni F. Cell Traction Forces on Soft Biomaterials. I. Microrheology of Type I Collagen Gels. *Biophys J* 2001;81:1786.

- [30] Latinovic O, Hough L a, Daniel Ou-Yang H. Structural and micromechanical characterization of type I collagen gels. *J Biomech* 2010;43:500.
- [31] Parekh A, Velegol D. Collagen gel anisotropy measured by 2-D laser trap microrheometry. *Ann Biomed Eng* 2007;35:1231.
- [32] Graessley WW. *Polymeric Liquids and Networks: Dynamics and Rheology*, New York: Garland Science; 2008, p. 801.
- [33] Brinson HF, Brinson LC. *Polymer Engineering Science and Viscoelasticity: An Introduction*. vol. 2007, New York: Springer; 2007, p. 1–15.
- [34] Sasaki N. *Viscoelasticity: From Theory to Biological Applications*. In: Vicente J de, editor., Croatia: InTech; 2012, p. 99–122.
- [35] Lim JJ, Temenoff JS. *Fundamentals of Tissue Engineering and Regenerative Medicine*. In: Meyer U, Meyer T, Handschel J, Wiesmann HP, editors., Berlin: Springer; 2009, p. 255–71.
- [36] Larson RG. *The Structure and Rheology of Complex Fluids*, New York: Oxford University Press; 1999, p. 107–80.
- [37] Goodwin JW, Hughes RW. *Rheology for Chemists: An Introduction*, Cambridge: Royal Society of Chemistry; 2008, p. 92–134.
- [38] Gobeaux F, Belamie E, Mosser G, Davidson P, Asnacios S. Power law rheology and strain-induced yielding in acidic solutions of type I-collagen. *Soft Matter* 2010;6:3769.
- [39] Wood GC, Keech MK. The formation of fibrils from collagen solutions. 1. The effect of experimental conditions: kinetic and electron-microscope studies. *Biochem J* 1960;75:588.
- [40] Doi M, Edwards SF. *The Theory of Polymer Dynamics*, New York: Oxford University Press; 1986, p. 140–87.
- [41] Graessley WW. *Polymeric Liquids and Networks: Structure and Properties*, New York: Taylor and Francis group; 2003, p. 265–329.
- [42] Mutch KJ, van Duijneveldt JS, Eastoe J. Colloid-polymer mixtures in the protein limit. *Soft Matter* 2007;3:155.
- [43] Doi M. *Introduction to Polymer Physics*, New York: Oxford University Press; 1996, p. 1–20.
- [44] Richards EG, Dover SD. *An Introduction to the Physical Properties of Large Molecules in Solution*, New York: CUP Archive; 1980, p. 91–6.
- [45] Doi M, Edwards SF. *The Theory of Polymer Dynamics*, New York: Oxford University Press; 1988, p. 289–322.

- [46] Baumann CG, Bloomfield VA, Smith SB, Bustamante C, Wang MD, Block SM. Stretching of Single Collapsed DNA Molecules. *Biophys J* 2000;78:1965.
- [47] MacKintosh FC, Janmey PA. Actin gels. *Curr Opin Solid State Mater Sci* 1997;2:350.
- [48] Amis EJ, Carriere CJ, Ferry JD, Veis A. Effect of pH on collagen flexibility determined from dilute solution viscoelastic measurements. *Int J Biol Macromol* 1985;7:130.
- [49] Nestler FH, Hvidt S, Ferry JD, Veis A. Flexibility of collagen determined from dilute solution viscoelastic measurements. *Biopolymers* 1983;22:1747.
- [50] Saito T, Iso N, Mizuno H, Onda N, Yamato H, Odashima H. Semiflexibility of collagens in solution. *Biopolymers* 1982;21:715.
- [51] Claire K, Pecora R. Translational and Rotational Dynamics of Collagen in Dilute Solution. *J Phys Chem B* 1997;101:746.
- [52] Utiyama H, Sakato K, Ikehara K, Setsuiye T, Kurata M. Flexibility of tropocollagen from sedimentation and viscosity. *Biopolymers* 1973;12:53.
- [53] Hofmann H, Voss T, Kühn K, Engel J. Localization of flexible sites in thread-like molecules from electron micrographs. *J Mol Biol* 1984;172:325.
- [54] Vesentini S, Redaelli A, Gautieri A. Nanomechanics of collagen microfibrils. *Muscles Ligaments Tendons J* 2013;3:23.
- [55] Buehler MJ, Wong SY. Entropic elasticity controls nanomechanics of single tropocollagen molecules. *Biophys J* 2007;93:37.
- [56] Sun YL, Luo ZP, An KN. Stretching short biopolymers using optical tweezers. *Biochem Biophys Res Commun* 2001;286:826.
- [57] Lovelady HH, Shashidhara S, Matthews WG. Solvent specific persistence length of molecular type I collagen. *Biopolymers* 2013;(In press).
- [58] Mu C, Li D, Lin W, Ding Y, Zhang G. Temperature induced denaturation of collagen in acidic solution. *Biopolymers* 2007;86:282–7.
- [59] Teraoka I. *Polymer Solutions: An Introduction to Physical Properties*, New York: John Wiley & Sons; 2002, p. 167–270.
- [60] Doi M, Edwards SF. *The Theory of Polymer Dynamics*, New York: Oxford University Press; 1988, p. 91–140.
- [61] Schnurr B, Gittes F, MacKintosh FC, Schmidt CF. Determining Microscopic Viscoelasticity in Flexible and Semiflexible Polymer Networks from Thermal Fluctuations. *Macromolecules* 1997;30:7781.

- [62] Gittes F, MacKintosh F. Dynamic shear modulus of a semiflexible polymer network. *Phys Rev E* 1998;58:R1241.
- [63] Everaers R, Jülicher F, Ajdari A, Maggs A. Dynamic Fluctuations of Semiflexible Filaments. *Phys Rev Lett* 1999;82:3717.
- [64] Larson RG. *The Structure and Rheology of Complex Fluids*. Struct. Rheol. Complex Fluids, New York: Oxford University Press; 1999, p. 1–66.
- [65] Waigh TA. Microrheology of complex fluids. *Reports Prog Phys* 2005;68:685.
- [66] Brown R. A brief account of microscopical observations made in the months of June, July and August, 1827, on the particles contained in the pollen of plants; and on the general existence of active molecules in organic and inorganic bodies. *Phil Mag* 1828;4:161.
- [67] Einstein A. Über die von der molekularkinetischen Theorie der Wärme geforderte Bewegung von in ruhenden Flüssigkeiten suspendierten Teilchen. *Ann Phys* 1905;17:549.
- [68] Perrin J. Mouvement brownien et réalité moléculaire. *Ann Chim Phys* 1909;18:5.
- [69] Crick FHC, Hughes AFW. The physical properties of cytoplasm. *Exp Cell Res* 1950;1:37.
- [70] Mason T, Ganesan K, van Zanten J, Wirtz D, Kuo S. Particle Tracking Microrheology of Complex Fluids. *Phys Rev Lett* 1997;79:3282.
- [71] Mahaffy RE, Shih CK, MacKintosh FC, Käs J. Scanning probe-based frequency-dependent microrheology of polymer gels and biological cells. *Phys Rev Lett* 2000;85:880.
- [72] Pine D, Weitz D, Chaikin P, Herbolzheimer E. Diffusing wave spectroscopy. *Phys Rev Lett* 1988;60:1134.
- [73] Schnurr B, Gittes F, Mackintosh FC, Schmidt CF. Determining Microscopic Viscoelasticity in Flexible and Semiflexible Polymer Networks from Thermal Fluctuations. *Macromolecules* 1997;30:7781.
- [74] Morse DC. Viscoelasticity of Concentrated Isotropic Solutions of Semiflexible Polymers. 1. Model and Stress Tensor. *Macromolecules* 1998;31:7030.
- [75] Morse DC. Viscoelasticity of Concentrated Isotropic Solutions of Semiflexible Polymers. 2. Linear Response. *Macromolecules* 1998;31:7044.
- [76] Fritz G, Pechhold W, Willenbacher N, Wagner NJ. Characterizing complex fluids with high frequency rheology using torsional resonators at multiple frequencies. *J Rheol* 2003;47:303.

- [77] Yang N, Hutter JL, de Bruyn JR. Microrheology, microstructure, and aging of physically cross-linked poly(vinyl alcohol)/poly(ethylene glycol) blends. *J Rheol* 2012;56:797.
- [78] Chen DT, Weeks ER, Crocker JC, Islam MF, Verma R, Gruber J, Levine AJ, Lubensky TC, Yodh AG. Rheological microscopy: local mechanical properties from microrheology. *Phys Rev Lett* 2003;90:108301.
- [79] Crocker JC, Grier DG. Methods of Digital Video Microscopy for Colloidal Studies. *J Colloid Interface Sci* 1996;179:298.
- [80] Wong I, Gardel M, Reichman D, Weeks E, Valentine M, Bausch A, Weitz D. Anomalous Diffusion Probes Microstructure Dynamics of Entangled F-Actin Networks. *Phys Rev Lett* 2004;92:178101.
- [81] Saxton MJ, Jacobson K. Single-Particle Tracking: Applications to Membrane Dynamics. *Annu Rev Biophys Biomol Struct* 1997;26:373.
- [82] Mason TG, Weitz DA. Optical Measurements of Frequency-Dependent Linear Viscoelastic Moduli of Complex Fluids. *Phys Rev E* 1995;74:1250.
- [83] Furst E, Gast A. Particle dynamics in magnetorheological suspensions using diffusing-wave spectroscopy. *Phys Rev E* 1998;58:3372.
- [84] Okajima T, Arakawa H, Alam MT, Sekiguchi H, Ikai A. Dynamics of a partially stretched protein molecule studied using an atomic force microscope. *Biophys Chem* 2004;107:51.
- [85] Fabry B, Maksym GN, Butler JP, Glogauer M, Navajas D, Fredberg JJ. Scaling the microrheology of living cells. *Phys Rev Lett* 2001;87:148102.
- [86] Neuman KC, Block SM. Optical trapping. *Rev Sci Instrum* 2004;75:2787.
- [87] Atakhorrami M, Addas KM, Schmidt CF. Twin optical traps for two-particle cross-correlation measurements: eliminating cross-talk. *Rev Sci Instrum* 2008;79:043103.
- [88] Buchanan M, Atakhorrami M, Paliarne JF, Schmidt CF. Comparing Macrorheology and One- and Two-Point Microrheology in Wormlike Micelle Solutions. *Macromolecules* 2005;38:8840–4.
- [89] Bertseva E, Grebenkov D, Schmidhauser P, Gribkova S, Jeney S, Forró L. Optical trapping microrheology in cultured human cells. *Eur Phys J E Soft Matter* 2012;35:63.
- [90] Brau RR, Ferrer JM, Lee H, Castro CE, Tam BK, Tarsa PB, Matsudaira P, Boyce MC, Kamm RD, Lang MJ. Passive and active microrheology with optical tweezers. *J Opt A Pure Appl Opt* 2007;9:103.

- [91] Fischer M, Richardson AC, Reihani SNS, Oddershede LB, Berg-Sørensen K. Active-passive calibration of optical tweezers in viscoelastic media. *Rev Sci Instrum* 2010;81:015103.
- [92] Rajkumar AS, Ali BMJ. Microrheology of concentrated DNA solutions using optical tweezers. *Life Sci* 2008;31:381.
- [93] Pesce G, De Luca AC, Rusciano G, Netti PA, Fusco S, Sasso A. Microrheology of complex fluids using optical tweezers: a comparison with macrorheological measurements. *J Opt A Pure Appl Opt* 2009;11:034016.
- [94] Ashkin A. Acceleration and Trapping of Particles by Radiation Pressure. *Phys Rev Lett* 1970;24:156.
- [95] Ashkin A, Dziedzic JM, Bjorkholm JE, Chu S. Observation of a single-beam gradient force optical trap for dielectric particles. *Opt Lett* 1986;11:288.
- [96] Crocker J, Grier D. When Like Charges Attract: The Effects of Geometrical Confinement on Long-Range Colloidal Interactions. *Phys Rev Lett* 1996;77:1897.
- [97] Hough LA, Ou-Yang HD. Correlated motions of two hydrodynamically coupled particles confined in separate quadratic potential wells. *Phys Rev E* 2002;65:1.
- [98] Block SM, Blair DF, Berg HC. Compliance of bacterial flagella measured with optical tweezers. *Nature* 1989;338:514.
- [99] Ashkin A, Dziedzic J. Optical trapping and manipulation of viruses and bacteria. *Science* 1987;235:1517.
- [100] Yoon YZ, Kotar J, Brown AT, Cicuta P. Red blood cell dynamics: from spontaneous fluctuations to non-linear response. *Soft Matter* 2011;7:2042.
- [101] Mehta AD, Rief M, Spudich JA, Smith DA, Simmons RM. Single-Molecule Biomechanics with Optical Methods. *Science* 1999;283:1689.
- [102] Mizuno D, Head DA, Mackintosh FC, Schmidt CF. Active and Passive Microrheology in Equilibrium and Nonequilibrium Systems. *Macromolecules* 2008;41:7194.
- [103] Baumann CG, Bloomfield VA, Smith SB, Bustamante C, Wang MD, Block SM. Stretching of single collapsed DNA molecules. *Biophys J* 2000;78:1965.
- [104] Reicherter M, Haist T, Wagemann EU, Tiziani HJ. Optical particle trapping with computer-generated holograms written on a liquid-crystal display. *Opt Lett* 1999;24:608.
- [105] Dufresne ER, Grier DG. Optical tweezer arrays and optical substrates created with diffractive optics. *Rev Sci Instrum* 1998;69:1974.

- [106] Dholakia K, Čižmár T. Shaping the future of manipulation. *Nat Photonics* 2011;5:335.
- [107] Grier DG. A revolution in optical manipulation. *Nature* 2003;424:810.
- [108] Farré A, Shayegan M, López-Quesada C, Blab GA, Montes-Usategui M, Forde NR, Martín-Badosa E. Positional stability of holographic optical traps. *Opt Express* 2011;19:21370.
- [109] Berne BJ, Pecora R. *Dynamic Light Scattering: With Applications to Chemistry, Biology, and Physics*, New York: John Wiley & Sons; 1976, p. 164–207.
- [110] Madou MJ. *Solid-State Physics, Fluidics, and Analytical Techniques in Micro- and Nanotechnology*. Boca Raton: CRC Press; 2011.
- [111] van der Horst A, Forde NR. Calibration of dynamic holographic optical tweezers for force measurements on biomaterials. *Opt Express* 2008;16:20987.
- [112] Berg-Sørensen K, Oddershede L, Florin E-L, Flyvbjerg H. Unintended filtering in a typical photodiode detection system for optical tweezers. *J Appl Phys* 2003;93:3167.
- [113] Addas KM, Schmidt CF, Tang JX. Microrheology of solutions of semi flexible biopolymer filaments using laser tweezers interferometry. *Phys Rev E* 2004;70:1.
- [114] Berg-Sørensen K, Flyvbjerg H. Power spectrum analysis for optical tweezers. *Rev Sci Instrum* 2004;75:594.
- [115] Tolić-Nørrelykke I, Munteanu E-L, Thon G, Oddershede L, Berg-Sørensen K. Anomalous Diffusion in Living Yeast Cells. *Phys Rev Lett* 2004;93:078102.
- [116] Landau LD, Lifshitz EM. *Statistical Physics*, Berlington: Elsevier; 1996, p. 384–9.
- [117] Zwanzig R. *Nonequilibrium Statistical Mechanics*, New York: Oxford University Press; 2001, p. 3–10.
- [118] Nijenhuis N, Mizuno D, Schmidt CF, Vink H, Spaan JAE. Microrheology of hyaluronan solutions: implications for the endothelial glycocalyx. *Biomacromolecules* 2008;9:2390.
- [119] Atakhorrami M, Sulkowska JI, Addas KM, Koenderink GH, Tang JX, Levine AJ, Mackintosh FC, Schmidt CF. Correlated fluctuations of microparticles in viscoelastic solutions: Quantitative measurement of material properties by microrheology in the presence of optical traps. *Phys Rev E* 2006;73:061501.
- [120] Dasgupta BR, Tee SY, Crocker JC, Frisken BJ, Weitz DA. Microrheology of polyethylene oxide using diffusing wave spectroscopy and single scattering. *Phys Rev E* 2002;65:051505.

- [121] Kühn K. Structure and function of Collagen types. In: Maynes R, editor., Elsevier; 1987, p. 1–42.
- [122] Birk DE, Bruckner P. Collagen: Primer in Structure, Processing and Assembly. In: Brinckmann J, Notbohm H, Müller PK, editors., Berlin: Springer; 2005, p. 185–205.
- [123] Shu-Tung Li. Biomaterials: Principles and Applications. In: Joon B . Park and Joseph D . Bronzino, editor., Boca Raton: CRC Press; 2002, p. 117–39.
- [124] Williams BR, Gelman RA, Poppke DC, Piez KA. Collagen fibril formation. Optimal in vitro conditions and preliminary kinetic results. *J Biol Chem* 1978;253:6578.
- [125] Hancox NM. *Biology of Bone*, New York: CUP Archive; 1972, p. 82–92.
- [126] Helseth DL, Veis A. Collagen self-assembly in vitro. Differentiating specific telopeptide-dependent interactions using selective enzyme modification and the addition of free amino telopeptide. *J Biol Chem* 1981;256:7118.
- [127] Orgel JPRO, Irving TC, Miller A, Wess TJ. Microfibrillar structure of type I collagen in situ. *Proc Natl Acad Sci U S A* 2006;103:9001.
- [128] Silver FH. Type I collagen fibrillogenesis in vitro. Additional evidence for the assembly mechanism. *J Biol Chem* 1981;256:4973.
- [129] Gautieri A, Vesentini S, Redaelli A, Buehler MJ. Hierarchical structure and nanomechanics of collagen microfibrils from the atomistic scale up. *Nano Lett* 2011;11:757.
- [130] Brodsky B, Ramshaw JAM. The collagen triple-helix structure. *Matrix Biol* 1997;15:545.
- [131] Kadler KE, Hojima Y, Prockop DJ. Assembly of collagen fibrils de novo by cleavage of the type I pC-collagen with procollagen C-proteinase. Assay of critical concentration demonstrates that collagen self-assembly is a classical example of an entropy-driven process. *J Biol Chem* 1987;262:15696.
- [132] Li Y, Asadi A, Monroe MR, Douglas EP. pH effects on collagen fibrillogenesis in vitro: Electrostatic interactions and phosphate binding. *Mater Sci Eng C* 2009;29:1643.
- [133] Kuznetsova N, Chi SL, Leikin S. Sugars and polyols inhibit fibrillogenesis of type I collagen by disrupting hydrogen-bonded water bridges between the helices. *Biochemistry* 1998;37:11888.
- [134] Brodsky B, Eikenberry EF, Cassidy K. An unusual collagen periodicity in skin. *Biochim Biophys Acta* 1980;621:162.
- [135] Li Y. The mechanism of collagen self-assembly: Hydrophobic and electrostatic interactions. PhD Thesis. University of Florida, 2009.

- [136] Judd RC. *The Protein Protocols Handbook*. New Jersey: Springer; 2002.
- [137] Winkler C, Denker K, Wortelkamp S, Sickmann A. Silver- and Coomassie-staining protocols: detection limits and compatibility with ESI MS. *Electrophoresis* 2007;28:2095.
- [138] Gelman RA, Williams BR, Piez KA. Collagen fibril formation. Evidence for a multistep process. *J Biol Chem* 1979;254:180.
- [139] Silver FH, Langley KH, Trelstad RL. Type I collagen fibrillogenesis: initiation via reversible linear and lateral growth steps. *Biopolymers* 1979;18:2523.
- [140] Fertala A, Sieron AL, Hojima Y, Ganguly A, Prockop DJ. Self-assembly into fibrils of collagen II by enzymic cleavage of recombinant procollagen II. Lag period, critical concentration, and morphology of fibrils differ from collagen I. *J Biol Chem* 1994;269:11584.
- [141] Silver FH, Birk DE. Kinetic Analysis of Collagen Fibrillogenesis: I. Use of Turbidity-Time Data. *Coll Relat Res* 1983;3:393.
- [142] Brennan M, Davison PF. Influence of the telopeptides on type I collagen fibrillogenesis. *Biopolymers* 1981;20:2195.
- [143] Chu B. *Laser Light Scattering: Basic Principles and Practice*, San Diego: Academic Press; 2007, p. 1–11.
- [144] Berne BJ, Pecora R. *Dynamic Light Scattering: With Applications to Chemistry, Biology, and Physics*, New York: John Wiley & Sons; 1976, p. 10–90.
- [145] Santos NC, Castanho MA. Teaching light scattering spectroscopy: the dimension and shape of tobacco mosaic virus. *Biophys J* 1996;71:1641.
- [146] Cummins HZ, Carlson FD, Herbert TJ, Woods G. Translational and rotational diffusion constants of tobacco mosaic virus from Rayleigh linewidths. *Biophys J* 1969;9:518.
- [147] Scott T. *ABC Biologie*. Berlin: Walter de Gruyter; 1996.
- [148] Carter J, Saunders VA. *Virology: Principles and Applications*, Chichester: John Wiley & Sons; 2007, p. 31–48.
- [149] Broersma S. Rotational Diffusion Constant of a Cylindrical Particle. *J Chem Phys* 1960;32:1626.
- [150] Hwang JS, Cummins HZ. Dynamic light scattering studies of collagen. *J Chem Phys* 1982;77:616.
- [151] Amis EJ, Carriere CJ, Ferry JD, Veis A. Effect of pH on collagen flexibility determined from dilute solution viscoelastic measurements. *Int J Biol Macromol* 1985;7:130.

- [152] Kubota K, Tominaga Y, Fujime S. Dynamic light-scattering study of semiflexible polymers: collagen. *Biopolymers* 1987;26:1717.
- [153] Frisken BJ. Revisiting the Method of Cumulants for the Analysis of Dynamic Light-Scattering Data. *Appl Opt* 2001;40:4087.
- [154] Hickenboth CR, Moore JS, White SR, Sottos NR, Baudry J, Wilson SR. Biasing reaction pathways with mechanical force. *Nature* 2007;446:423–7.
- [155] Stathopoulos PB, Scholz GA, Hwang Y-M, Rumfeldt JAO, Lepock JR, Meiering EM. Sonication of proteins causes formation of aggregates that resemble amyloid. *Protein Sci* 2004;13:3017.
- [156] Stephenson FH. *Calculations for Molecular Biology and Biotechnology: A Guide to Mathematics in the Laboratory*, London: Academic Press; 2004, p. 270–8.
- [157] Wilson K, Walker J. *Principles and Techniques of Practical Biochemistry*, Cambridge: Cambridge University Press; 2000, p. 263–312.
- [158] Erickson HP. Size and shape of protein molecules at the nanometer level determined by sedimentation, gel filtration, and electron microscopy. *Biol Proced Online* 2009;11:32.
- [159] Schmitz KS. *An Introduction to Dynamic Light Scattering by Macromolecules*, New York: Academic Press; 1990, p. 77–99.
- [160] Furthmayr H, Wiedemann H, Timpl R, Odermatt E, Engel J. Electron-microscopical approach to a structural model of intima collagen. *Biochem J* 1983;211:303.
- [161] Caroline D. *Developments in Polymer Characterization*. In: Dawkins J V., editor., New York: Elsevier; 1986, p. 49–95.
- [162] Shayegan M, Forde NR. Microrheological characterization of collagen systems: from molecular solutions to fibrillar gels. *PLoS One* 2013;8:e70590.
- [163] Shayegan M, Forde NR. Probing the Viscoelasticity of Collagen Solutions via Optical-Tweezers-Based Microrheology. *MRS Proc* 2012;1465:mrss12–1465–ss06–08.
- [164] Huh JY, Furst EM. Colloid dynamics in semiflexible polymer solutions. *Phys Rev E* 2006;74:031802.
- [165] Shankar V, Pasquali M, Morse DC. Theory of linear viscoelasticity of semiflexible rods in dilute solution. *J Rheol (N Y N Y)* 2002;46:1111.
- [166] Hough LA, Ou-Yang HD. Viscoelasticity of aqueous telechelic poly(ethylene oxide) solutions: relaxation and structure. *Phys Rev E* 2006;73:031802.

- [167] Gautieri A, Vesentini S, Redaelli A, Buehler MJ. Viscoelastic properties of model segments of collagen molecules. *Matrix Biol* 2012;31:141.
- [168] Rezaei N, Downing BPB, Wieczorek A, Chan CKY, Welch RL, Forde NR. Using optical tweezers to study mechanical properties of collagen. In: Kashyap R, Têtu M, Kleiman RN, editors. *Proc. SPIE, Ottawa, Canada: International Society for Optics and Photonics*; 2011, p. 80070K.
- [169] Obermayer B, Frey E. Tension dynamics and viscoelasticity of extensible wormlike chains. *Phys Rev E* 2009;80:040801.
- [170] Mitchell BS. *An Introduction to Materials Engineering and Science for Chemical and Materials Engineers*, New Jersey: John Wiley & Sons; 2004, p. 285–376.
- [171] Rubinstein M, Colby R, Dobrynin A. Dynamics of Semidilute Polyelectrolyte Solutions. *Phys Rev Lett* 1994;73:2776–9.
- [172] Kulicke W-M, Clasen C. *Viscosimetry of Polymers and Polyelectrolytes*, Hamburg: Springer; 2004, p. 49–68.
- [173] Fuoss RM. Polyelectrolytes. *Discuss Faraday Soc* 1951;11:125.
- [174] Cho J, Heuzey M-C, Bégin A, Carreau PJ. Viscoelastic properties of chitosan solutions: Effect of concentration and ionic strength. *J Food Eng* 2006;74:500–15.
- [175] Fusco S, Borzacchiello A, Miccio L, Pesce G, Rusciano G, Sasso A, Netti PA. High frequency viscoelastic behaviour of low molecular weight hyaluronic acid water solutions. *Biorheology* 2007;44:403.
- [176] Gobeaux F, Belamie E, Mosser G, Davidson P, Asnacios S. Power law rheology and strain-induced yielding in acidic solutions of type I-collagen. *Soft Matter* 2010;6:3769.
- [177] Lai G, Li Y, Li G. Effect of concentration and temperature on the rheological behavior of collagen solution. *Int J Biol Macromol* 2008;42:285.
- [178] Chae BS, Furst EM. Probe surface chemistry dependence and local polymer network structure in F-actin microrheology. *Langmuir* 2005;21:3084.
- [179] Chen D, Weeks E, Crocker J, Islam M, Verma R, Gruber J, Levine A, Lubensky T, Yodh A. Rheological Microscopy: Local Mechanical Properties from Microrheology. *Phys Rev Lett* 2003;90:108301.
- [180] He J, Tang JX. Surface adsorption and hopping cause probe-size-dependent microrheology of actin networks. *Phys Rev E* 2011;83:041902.
- [181] Butt H-J, Graf K, Kappl M. *Physics and Chemistry of Interfaces*. Weinheim: John Wiley & Sons; 2006.

- [182] Kuznetsova N, Leikin S. Does the triple helical domain of type I collagen encode molecular recognition and fiber assembly while telopeptides serve as catalytic domains? Effect of proteolytic cleavage on fibrillogenesis and on collagen-collagen interaction in fibers. *J Biol Chem* 1999;274:36083.
- [183] Sato K, Ebihara T, Adachi E, Kawashima S, Hattori S, Irie S. Possible involvement of aminotelopeptide in self-assembly and thermal stability of collagen I as revealed by its removal with proteases. *J Biol Chem* 2000;275:25870.
- [184] McGuire M, Beerman KA. *Nutritional Sciences: From Fundamentals to Food*, Belmont: Cengage Learning; 2011, p. 175–213.
- [185] Prockop DJ, Fertala A. Inhibition of the self-assembly of collagen I into fibrils with synthetic peptides. Demonstration that assembly is driven by specific binding sites on the monomers. *J Biol Chem* 1998;273:15598.
- [186] Larsen TH, Branco MC, Rajagopal K, Schneider JP, Furst EM. Sequence-dependent gelation kinetics of β -hairpin peptide hydrogels. *Macromolecules* 2009;42:8443.
- [187] Piechocka IK, van Oosten ASG, Breuls RGM, Koenderink GH. Rheology of heterotypic collagen networks. *Biomacromolecules* 2011;12:2797.
- [188] Savin T, Doyle PS. Electrostatically tuned rate of peptide self-assembly resolved by multiple particle tracking. *Soft Matter* 2007;3:1194.
- [189] Tseng Y. Microheterogeneity Controls the Rate of Gelation of Actin Filament Networks. *J Biol Chem* 2002;277:18143.
- [190] Xu J, Palmer A, Wirtz D. Rheology and Microrheology of Semiflexible Polymer Solutions: Actin Filament Networks. *Macromolecules* 1998;31:6486.
- [191] Yang Y, Kaufman LJ. Rheology and confocal reflectance microscopy as probes of mechanical properties and structure during collagen and collagen/hyaluronan self-assembly. *Biophys J* 2009;96:1566.
- [192] Shayegan M, Rezaei N, Lam NH, Altindal T, Wieczorek A, Forde NR. Probing multiscale mechanics of collagen with optical tweezers. In: Dholakia K, Spalding GC, editors. *Proc. SPIE, San Diego: International Society for Optics and Photonics*; 2013, p. 88101P.
- [193] Newman S, Cloître M, Allain C, Forgacs G, Beysens D. Viscosity and elasticity during collagen assembly in vitro: relevance to matrix-driven translocation. *Biopolymers* 1997;41:337.
- [194] Forgacs G, Newman SA, Hinner B, Maier CW, Sackmann E. Assembly of collagen matrices as a phase transition revealed by structural and rheologic studies. *Biophys J* 2003;84:1272.

- [195] Vader D, Kabla A, Weitz D, Mahadevan L. Strain-induced alignment in collagen gels. *PLoS One* 2009;4:e5902.
- [196] Arevalo RC, Urbach JS, Blair DL. Size-dependent rheology of type-I collagen networks. *Biophys J* 2010;99:L65.
- [197] Yang Y, Motte S, Kaufman LJ. Pore size variable type I collagen gels and their interaction with glioma cells. *Biomaterials* 2010;31:5678.
- [198] Velegol D, Lanni F. Cell traction forces on soft biomaterials. I. Microrheology of type I collagen gels. *Biophys J* 2001;81:1786.
- [199] Gelman RA, Poppke DC, Piez KA. Collagen fibril formation in vitro. The role of the nonhelical terminal regions. *J Biol Chem* 1979;254:11741.
- [200] Lindström SB, Vader DA, Kulachenko A, Weitz DA. Biopolymer network geometries: characterization, regeneration, and elastic properties. *Phys Rev E Stat Nonlin Soft Matter Phys* 2010;82:051905.
- [201] Shen ZL, Kahn H, Ballarini R, Eppell SJ. Viscoelastic properties of isolated collagen fibrils. *Biophys J* 2011;100:3008.
- [202] Piechocka IK, Bacabac RG, Potters M, Mackintosh FC, Koenderink GH. Structural hierarchy governs fibrin gel mechanics. *Biophys J* 2010;98:2281.
- [203] Discher DE, Janmey P, Wang Y-L. Tissue cells feel and respond to the stiffness of their substrate. *Science* 2005;310:1139.
- [204] Helary C, Bataille I, Abed A, Illoul C, Anglo A, Louedec L, Letourneur D, Meddahi-Pellé A, Giraud-Guille MM. Concentrated collagen hydrogels as dermal substitutes. *Biomaterials* 2010;31:481.
- [205] Dogterom M, Kerssemakers JW, Romet-Lemonne G, Janson ME. Force generation by dynamic microtubules. *Curr Opin Cell Biol* 2005;17:67.
- [206] Pollard TD, Borisy GG. Cellular motility driven by assembly and disassembly of actin filaments. *Cell* 2003;112:453.
- [207] Djabourov M. Architecture of gelatin gels. *Contemp Phys* 1988;29:273.
- [208] Djabourov M, Leblond J, Papon P. Gelation of aqueous gelatin solutions. II. Rheology of the sol-gel transition. *J Phys* 1988;49:333–43.
- [209] Hu XW, Knight DP, Chapman JA. The effect of non-polar liquids and non-ionic detergents on the ultrastructure and assembly of rat tail tendon collagen fibrils in vitro. *Biochim Biophys Acta* 1997;1334:327.
- [210] Grebenkov DS, Vahabi M, Bertseva E, Forró L, Jeney S. Hydrodynamic and subdiffusive motion of tracers in a viscoelastic medium. *Phys Rev E* 2013;88:040701.

- [211] Tassieri M, Evans RML, Warren RL, Bailey NJ, Cooper JM. Microrheology with optical tweezers: data analysis. *New J Phys* 2012;14:115032.
- [212] Raghov R. Vascular Medicine: A Companion to Braunwald's Heart Disease. In: Creager M, Beckman JA, Loscalzo J, editors., Philadelphia: Elsevier Health Sciences; 2012, p. 43–70.
- [213] Silver FH, Snowhill PB, Foran DJ. Mechanical Behavior of Vessel Wall: A Comparative Study of Aorta, Vena Cava, and Carotid Artery. *Ann Biomed Eng* 2003;31:793–803.
- [214] Diez J, Lopez B, Gonzalez A, Querejeta R. The Role of Myocardial Collagen Network in Hypertensive Heart Disease. *Curr Hypertens Rev* 2007;3:1–7.
- [215] Rich JP, McKinley GH, Doyle PS. Size dependence of microprobe dynamics during gelation of a discotic colloidal clay. *J Rheol (N Y N Y)* 2011;55:273.
- [216] De Bruyn JR. Modeling the microrheology of inhomogeneous media. *J Nonnewton Fluid Mech* 2013;193:21–7.
- [217] Crocker JC, Valentine MT, Weeks ER, Gislser T, Kaplan PD, Yodh a G, Weitz D a. Two-point microrheology of inhomogeneous soft materials. *Phys Rev Lett* 2000;85:888.
- [218] Starrs L, Bartlett P. One- and two-point micro-rheology of viscoelastic media. *J Phys Condens Matter* 2003;15:S251.
- [219] Oster G, Mogilner A. Force Generation by Cellular Polymers. In: Ciferri A, editor. *Supramol. Polym.*, Boca Raton: CRC Press; 2005, p. 741–50.
- [220] Mizuno D, Tardin C, Schmidt CF, Mackintosh FC. Nonequilibrium mechanics of active cytoskeletal networks. *Science* 2007;315:370.
- [221] Molecular Probes. Product information: Alexa Fluor 647 Microscale Protein Labeling Kit (A20173). 2006.

Appendix A.

Rationale for the Preference of Manual Adjustment of Laser Power

The laser power delivered to the sample can be adjusted in two different ways. The laser controller provides the ability to change the power via a current adjustment. Additionally, as described in Section 2.2, our optical tweezers apparatus allows for manual adjustment of laser power delivered to the chamber, using the half-wave plate in the set-up (Figure 2.3). Here, I explain why I chose latter method to adjust the laser power.

"Strange" power spectra were obtained for the displacements of a particle trapped in water when the laser current was adjusted to be less than ~ 11 A. That is, a broad peak/shoulder appears at the tail of the spectra and its position and height vary with the laser power. The laser light itself seems to be responsible for this behavior. As shown in Figure A.1, setting the laser current above 11 A eliminates the peak up to the Nyquist frequency (50 kHz).

According to this observation, the current of the laser was decided to be set to a constant value (12 A), and the power directed to the chamber was adjusted manually by rotating the half-wave plate before the polarizing beam splitter.

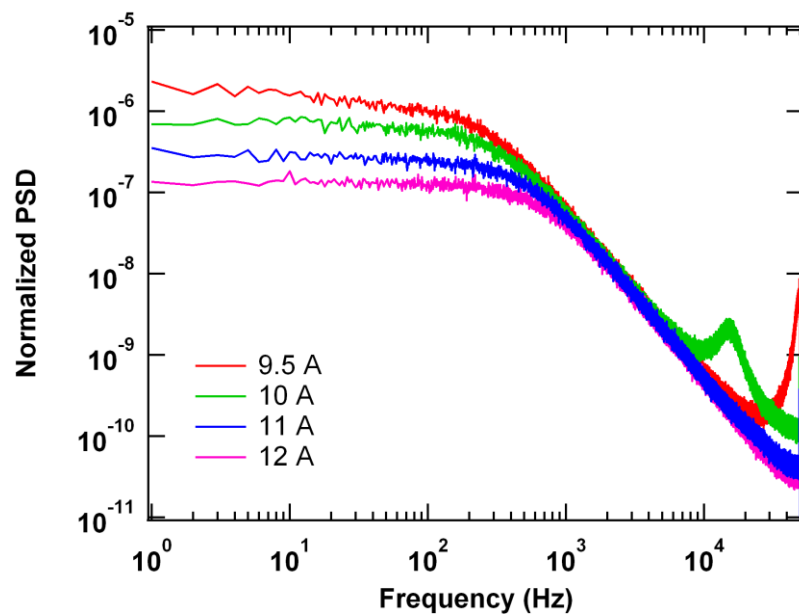


Figure A.1. Power spectrum of a 2.1 μm polystyrene particle trapped in water using four different laser currents.

Appendix B.

Mathematical Derivation of the Relationship Between Trap Stiffness and Complex Shear Moduli

Here, it is mathematically shown first that the viscous modulus is not influenced by the trap stiffness, and second, that the trap's effect on the elastic modulus can be corrected using Eq. 2.12.

The measured complex response function (the reciprocal function of the measured stiffness) can be related to that of the medium and the trap stiffness by

$$\frac{1}{A_{measured}^*} = \frac{1}{A_{medium}^*} + \kappa, \quad (B.1)$$

where κ is the trap stiffness [113]. Using $A^* = A' + iA''$, Eq. B.1 becomes

$$\frac{1}{A'_{measured} + iA''_{measured}} = \frac{1}{A'_{medium} + iA''_{medium}} + \kappa. \quad (B.2)$$

Since $\frac{1}{x + iy} = \frac{x - iy}{x^2 + y^2}$, Eq. B.2 can be rewritten as

$$\begin{aligned} \frac{A'_{measured}}{A'^2_{measured} + A''^2_{measured}} - i \frac{A''_{measured}}{A'^2_{measured} + A''^2_{measured}} = \\ \frac{A'_{medium}}{A'^2_{medium} + A''^2_{medium}} - i \frac{A''_{medium}}{A'^2_{medium} + A''^2_{medium}} + \kappa. \end{aligned} \quad (B.3)$$

For this equation to be true, both the real parts and imaginary parts in two sides of the equation should be equal:

$$\frac{A'_{measured}}{A'^2_{measured} + A''^2_{measured}} = \frac{A'_{medium}}{A'^2_{medium} + A''^2_{medium}} + \kappa, \quad (B.4)$$

$$\frac{A''_{measured}}{A'_{measured}{}^2 + A''_{measured}{}^2} = \frac{A''_{medium}}{A'_{medium}{}^2 + A''_{medium}{}^2}. \quad (\text{B.5})$$

Using Eq. (2.11), the magnitudes of the elastic and viscous moduli are

$$G' = \frac{1}{6\pi R} \frac{A'}{A'^2 + A''^2}, \quad (\text{B.6})$$

$$G'' = \frac{1}{6\pi R} \frac{A''}{A'^2 + A''^2}.$$

Combining this with Eq. B.4 and B.5, the desired results are obtained:

$$G'_{measured} = G'_{medium} + \frac{\kappa}{6\pi R}, \quad (\text{B.7})$$

$$G''_{measured} = G''_{medium}.$$

Appendix C.

High-Frequency Dispersion of Elastic Modulus

In order to understand the origin of the dispersion of the elastic modulus at high frequency (Figure 2.12), first, the Lorentzian function (Eq. 2.5) has been used to produce an ideal PSD (ignoring aliasing) up to a maximum frequency of 50 kHz (Figure C.1). These theoretical values are then used to calculate the complex response function followed by the elastic modulus (Figure C.2).

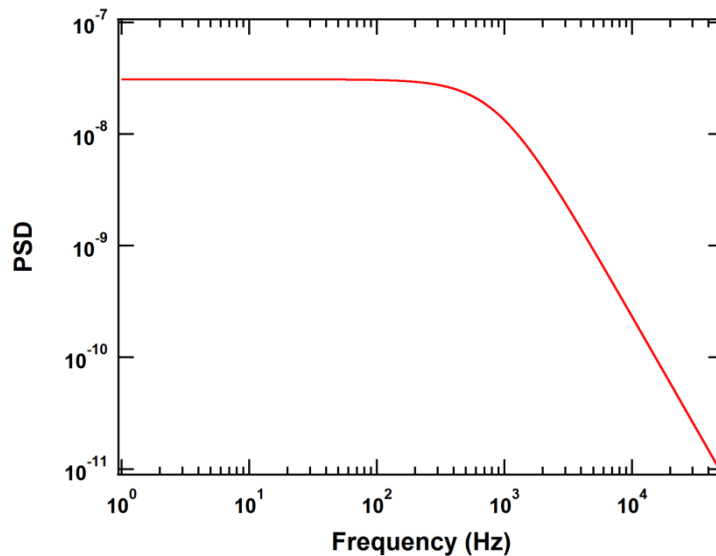


Figure C.1. An ideal theoretical power spectrum of a particle in water according to Eq. 2.5 (the Lorentzian function) with $f_c = 873\text{Hz}$ and $A = 0.0235 \text{ ((V/V)}^2\text{.Hz)}$.

As explained in Chapter 2, the Kramers-Kronig integration (Eq. 2.10) suffers a drop at high frequency due to the cut-off of the integration. To verify this, one can extrapolate the -2 slope of the power spectrum (for water) to infinity and find the response functions and shear moduli as if the measurements were performed at infinite bandwidth. Figures C.2(A) and (B) compare the results for the response function and elastic modulus for a finite sampling condition (solid lines) and an infinite bandwidth (dashed lines). While no difference is seen in the imaginary part of the response function (as expected), the real part of both the response function and the elastic modulus start to deviate significantly below their true values beyond ~3 kHz.

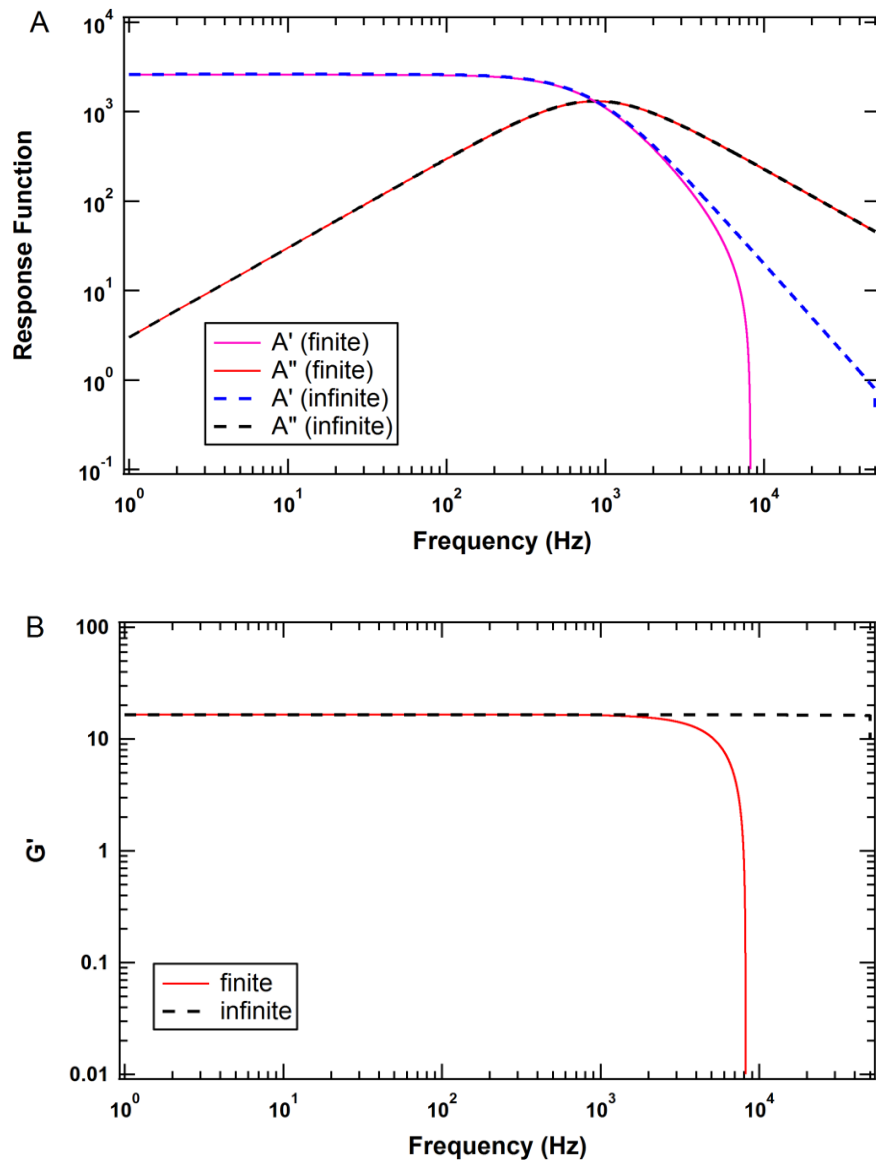


Figure C.2. (A) Real and imaginary parts of the response function for a particle trapped in water, for a finite sampling rate of 100 kHz (solid lines) and as if it were sampled at an infinite bandwidth (dashed lines). (B) Elastic shear modulus obtained for the above conditions.

More realistically, an experimental power spectrum of the bead is described by Lorentzian function where the data include random noise. Here, to test for the effect of the noise, a more realistic form of power spectrum is produced (Figure C.3) by the simulated motions of a bead in an optical trap conducted by Naghmeh Rezaei, a PhD student in our lab. The same analysis is repeated for these data and the results are shown in Figure C.4. The effect of the noise is that the values of elastic modulus start to

disperse around the true value (*i.e.* perfect infinite measurement), while the overall trend in the elastic shear modulus at >9 kHz is to decrease (in Figure C.4(B), compare the averaged, blocked results with that as if it were sampled at infinite bandwidth).

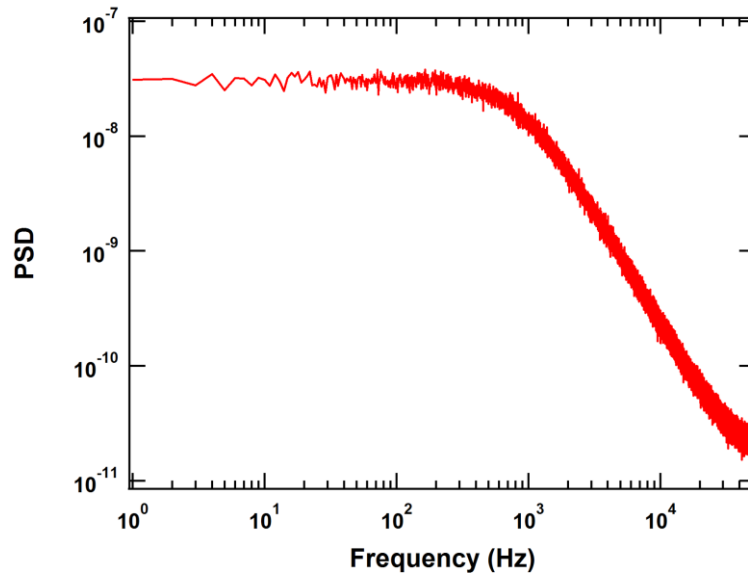


Figure C.3. The power spectrum of a particle in water obtained from particle's simulated motions in an optical trap. Parameters of the Lorentzian fit are similar to those in Figure C.1, and here, aliasing at high frequencies is apparent.

According to the studies presented in this Appendix, the origin of the overall drop of elastic modulus at high-frequency (Figures 2.11 and 2.12) is from the frequency cut-off in Kramers-Kronig integration (Eq. 2.10) due to the finite sampling, which leads to underestimation of elastic modulus (in the example here, at >9 kHz). Additionally, stochastic noise in the power spectrum causes significant dispersion around the theoretically obtained, noise-free value (here, at frequencies greater than ~500 Hz).

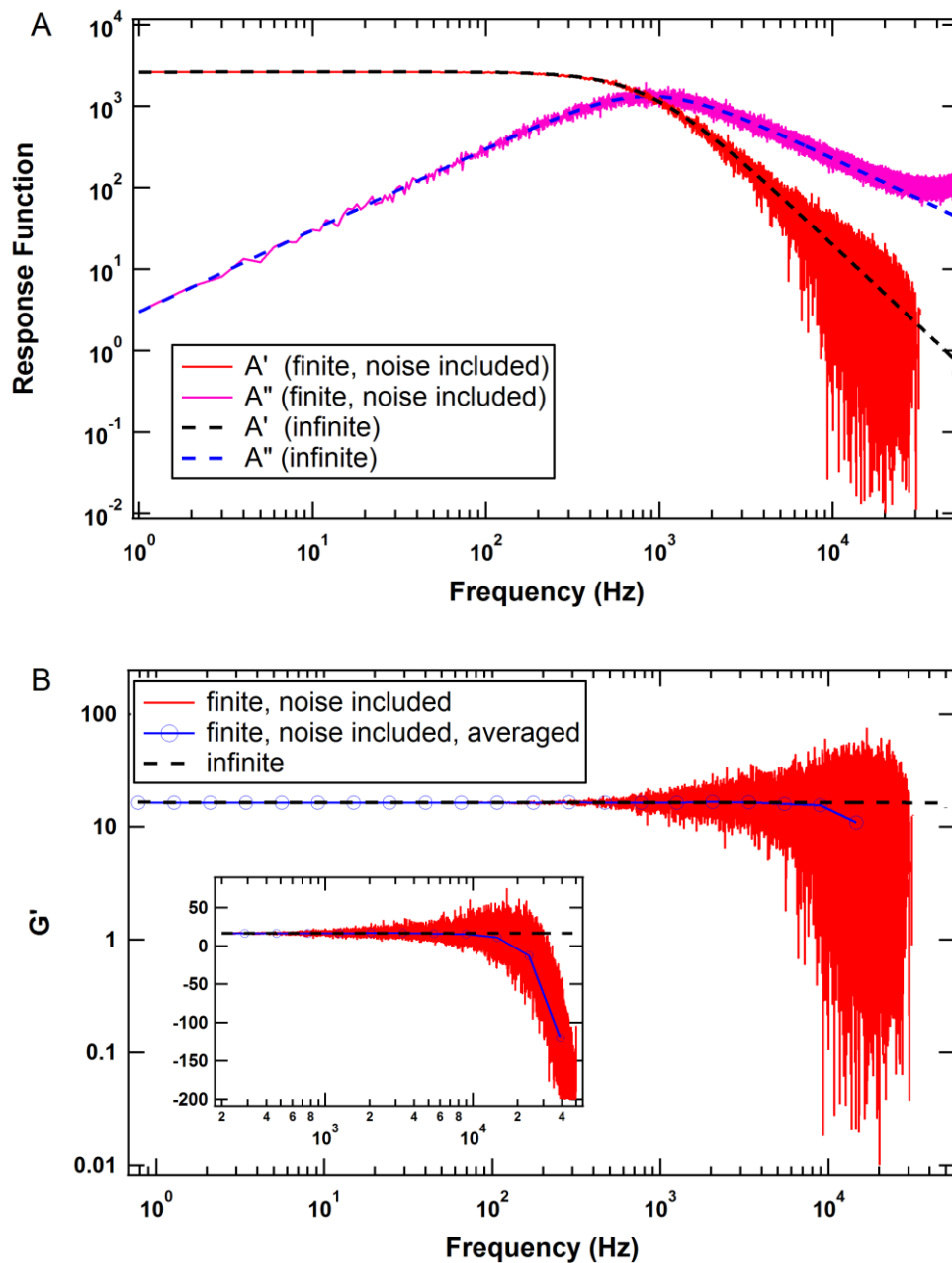


Figure C.4. (A) Real and imaginary parts of the response function for a particle trapped in water, when it is sampled at finite sampling rate of 100 kHz (solid lines) when random noise is included and as if it were sampled at an infinite bandwidth with no noise (dashed lines). (B) Elastic shear modulus obtained for the above conditions. Blue circles are the averaged, blocked results of the elastic modulus with finite sampling (solid line). Inset: The data are replotted on a semi-logarithmic scale to show better the overall decreasing trend of elastic modulus at high frequency.

Appendix D.

Labelling Collagen with Alexa Fluorophore

(Adapted from Invitrogen technical notes [221])

Alexa Fluorophore Chemistry:

Diagram below shows the Alexa Fluor 647. The dye covalently binds to protein through its coupling reaction with a primary amine on a protein (e.g. the side-chain of a lysine).

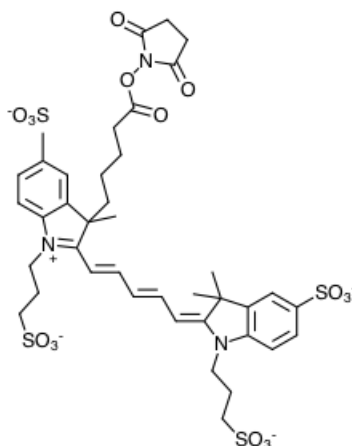


Figure D.1. Structure of Alexa Fluor 647 carboxylic acid, succinimidyl ester.

Materials:

- Carbonate-bicarbonate buffer (0.5 M carbonate plus 2.5 M NaCl, pH 9.3)
- Stock Alexa 647 succinimide in DMSO (200 μ l of dry DMSO were added to 1 mg of Alexa reagent. Then, from this stock solution aliquots of 10 μ l were stored at -80°C.)

Procedure:

- 1) Dilute the stock carbonate buffer 1:2.5 in water (final concentration of 0.2 M carbonate plus 1 M NaCl)
- 2) Dialyze the collagen solution into this carbonate buffer: 3 changes of 100 μ l in each tube, 30 minutes per change (at room temperature)

- 3) Collect the dialyzed sample by poking the membrane and centrifuging at 855 g for 1 minute
- 4) Add 10 μ l of the stock Alexa in DMSO into the dialyzed collagen sample (500 μ l). Wrap the tube in tinfoil to prevent light reaching the reaction and leave it rotating at room temperature for 1 hour
- 5) Dialyze back into 20 mM acetic acid as in step 2
- 6) Collect the dialyzed labelled collagen as in step 3

Appendix E.

Enzyme-Linked Immunosorbent Assay (ELISA)

The schematic diagram below illustrates the chemical steps for the ELISA experiments used to quantify collagen concentration. There are various types of ELISA available depending on the methodology of capturing the antigen (here, collagen) directly or indirectly (using a trapping antibody) in the wells. I empirically found that for collagen type I, it is more efficient not to use a trapping antibody and let collagen stick on the walls by itself. Then, in the next step, I specifically detect collagen molecules using a detecting antibody.

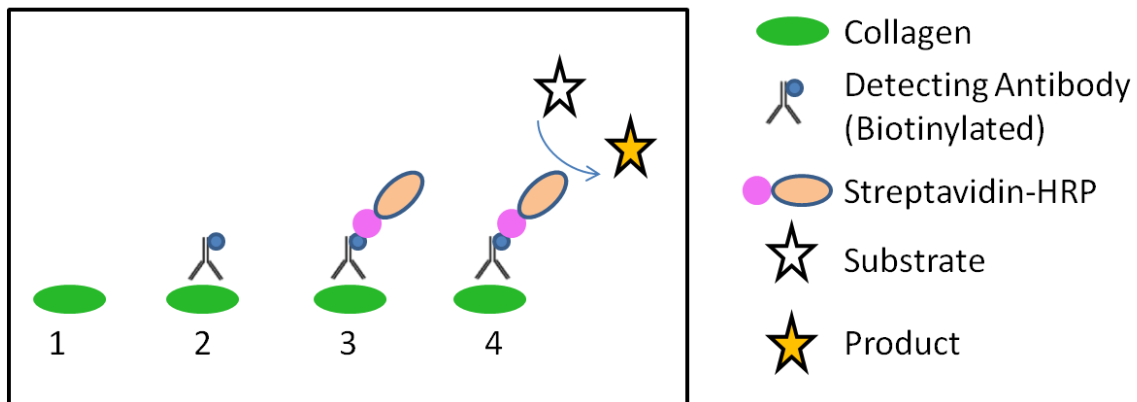


Figure E.1. Chemical steps for the ELISA experiment.

Materials:

- 96-well ELISA plate
- Phosphate Buffered Saline (PBS 1X)
- Tween 20 (Sigma)
- Bovine serum albumin (BSA, Jackson ImmunoResearch)
- Mouse monoclonal anti-rat type I collagen antibody, biotinylated (Chondrex)
- HRP-Conjugated Streptavidin (Jackson ImmunoResearch)
- 3,3',5,5'-Tetramethylbenzidine (Sigma)
- 1.2 M HCl

Procedure:

- 1) Prepare serial dilutions of collagen solutions (concentration range: 0-10 $\mu\text{g/ml}$, solvent: 1X PBS) and add 100 μl of each to different wells of the 96-well plate (incubation for 2 hours at room temperature or overnight at 4°C).
- 2) Remove the solution (pour by quickly inverting the whole plate) and add 200 μl of blocking reagent (2% BSA in PBS including 0.1% Tween) in each well (1 hour at room temperature).
- 3) Prepare serial dilutions of detecting antibody solutions (concentration range: 0-1 $\mu\text{g/ml}$, solvent: 2% BSA in PBS including 0.1% Tween).
- 4) Remove the blocking reagent and add 100 μl of prepared antibody solutions to each well (1 hour at room temperature).
- 5) Remove the solutions and wash the plate three times with PBS including 0.1% Tween (200 μl in each well for each wash, no incubation time is required).
- 6) Add 100 μl of HRP-Conjugated Streptavidin solutions to each well (concentration: 0.1 $\mu\text{g/ml}$, solvent: 2% BSA in PBS including 0.1% Tween) (1 hour at room temperature).
- 7) Remove the solutions and wash the plate 5 times with PBS including 0.1% Tween (200 μl in each well for each wash).
- 8) Add 50 μl of the substrate (Tetramethylbenzidine) and wait for color change (~10 minutes, blue color). Read the optical density at 645 nm.
- 9) Add 50 μl of the stopping reagent (1.2 M HCl) and read the optical density at 460 nm. (Stopping reagent terminates the HRP reaction with substrate by altering the pH of the system and produces a yellow end product.)
- 10) Analyze the data by preparing a standard curve from the serial dilutions of a sample of known concentration (concentration on X axis and optical density on Y axis), then, extract the unknown concentrations by interpolating the optical density values.